Molecular Simulation Studies of Lipid Bilayers and Biomolecular Coatings for Water

Barrier and Biocompatibility Purposes

By

Alexander Hao Yang

Dissertation

Submitted to the Faculty of the

Graduate School of Vanderbilt University

in partial fulfillment of the requirements

for the degree of

DOCTOR OF PHILOSOPHY

in

Chemical Engineering

January 31, 2020

Nashville, Tennessee

Approved:

Clare McCabe, Ph.D.

Peter T. Cummings, Ph.D.

G. Kane Jennings, Ph.D.

Paul E. Laibinis, Ph.D.

Todd R. Graham, Ph.D.

To my family and friends, thank you for always supporting me.

ACKNOWLEDGMENTS

TABLE OF CONTENTS

LIST OF TABLES

LIST OF FIGURES

Chapter 1

Introduction

Lipid bilayers are a class of membranes that occur naturally and synthetically. Their tunable structure and phase behavior can be used to alter transport and barrier properties for both topical and biological applications. To control the structure and phase behavior of lipid bilayers, their composition can be modified. Thus, a fundamental understanding between composition, structure, and function is necessary for rationally designing bilayers in the aforementioned applications.

In particular, water permeability and neurotransmission are interesting applications that can be controlled via lipid bilayer structure and phase behavior. To study various aspects of these properties at the nanoscale, molecular simulation (in particular, molecular dynamics simulation) was used to systematically vary and examine the influence of chemical composition on lipid bilayer structure. Chapter 2 outlines the fundamental chemistry that governs membranes and lipid bilayers, with a summary of relevant experimental, theoretical, and simulation work. Chapter 2 also includes a discussion of the various phases and associated properties of lipid bilayers. Chapter 3 describes how composition can tune the structural properties of lipid bilayers in the gel phase. Chapter 4 builds on this work by examining how gel-phase bilayer structure influences water permeability. Chapter 5 examines how graphene and single-stranded DNA influence the structure and organization of lipid bilayers in the fluid phase. Lastly, Chapter 6 summarizes the work in this thesis and recommends further work.

Chapter 2

Background

2.1   The Roles of Membranes

Membranes are ubiquitous macromolecular structures that can be found throughout biological, chemical, and material fields. A well-known adage, "structure determines function", summarizes how to design materials for a particular application. In a general sense, membranes, largely planar materials, are effective at separating distinct chemical systems. This property can be attributed to the membrane's barrier ability to both physically and chemically allow certain materials in and out, also known as selectivity or semipermeability. Chemical and material applications of membranes include reverse osmosis for water desalinization[1] and proton exchange for fuel cell energy applications,[2] whereby polymer membranes can be used to separate and filter water from contaminants or protons from chemical compounds. In biology, membranes can also be found within the blood brain barrier,[3] biological cells, and the skin;[4–13] these barriers help protect vital biological systems from external entities.

One particularly appealing attribute of membranes is their passive permeability, in which energy does not need to be expended in order to transport or separate particular components.[14] To understand some passive permeability properties and design membranes for separation processes, one can draw from some fundamental chemical engineering concepts, including thermodynamics and transport. Thermodynamic considerations include free energy barriers to permeation. Depending on the chemical composition of the membrane, different permeants will experience a variety of energetically favorable or unfavorable interactions, which help predict which permeants, at what frequency, will enter the membrane. Among permeants, comparing the free energy barriers and partition coeffi-

cients helps evaluate a membrane's selectivity. Transport considerations include diffusion. Again, depending on the chemical composition of the membrane, different permeants will exhibit different mobilities around and inside the membrane. When designing practical engineering applications of membranes, relevant considerations include synthesis cost, selectivity, rate of separation, environmental effects, scale-up, maintenance, and durability, particularly in the realm of proton exchange and reverse osmosis membranes.[15,16] Biological applications must additionally consider biocompatibility.

Within biological fields, membranes commonly manifest as lipid bilayers, and sometimes multilayers, in both natural and artificial applications. One of the astounding features of lipid bilayers is how their composition and structure can be tailored to a particular environment or function. While lipid bilayers are generally planar structures, tuning their chemical composition will modify their specific structural properties and, consequently, their specific function. As a result, lipid bilayers can be designed and engineered for countless applications, including those mentioned earlier.

2.2   Chemical Overview of Lipid Bilayers

Lipids are organic compounds that contain hydrophilic and hydrophobic regions. In general, hydrophilic components are slightly polar or charged, yielding energetically favorable interactions with water. On the other hand, hydrophobic components are neither polar nor strongly charged, resulting in energetically unfavorable interactions with water. Because of this chemical distinction, the different regions will tend to aggregate with each other – hydrophilic regions will spatially orient closer to each other and with water, while hydrophobic regions will spatially orient closer to each other and away from water. Common lipids are shown in Figure 2.1.

1,2-distearoyl-sn-glycero-3-phosphocholine (DSPC)

1,2-dioleoyl-sn-glycero-3-phosphocholine (DOPC)

Cholesterol
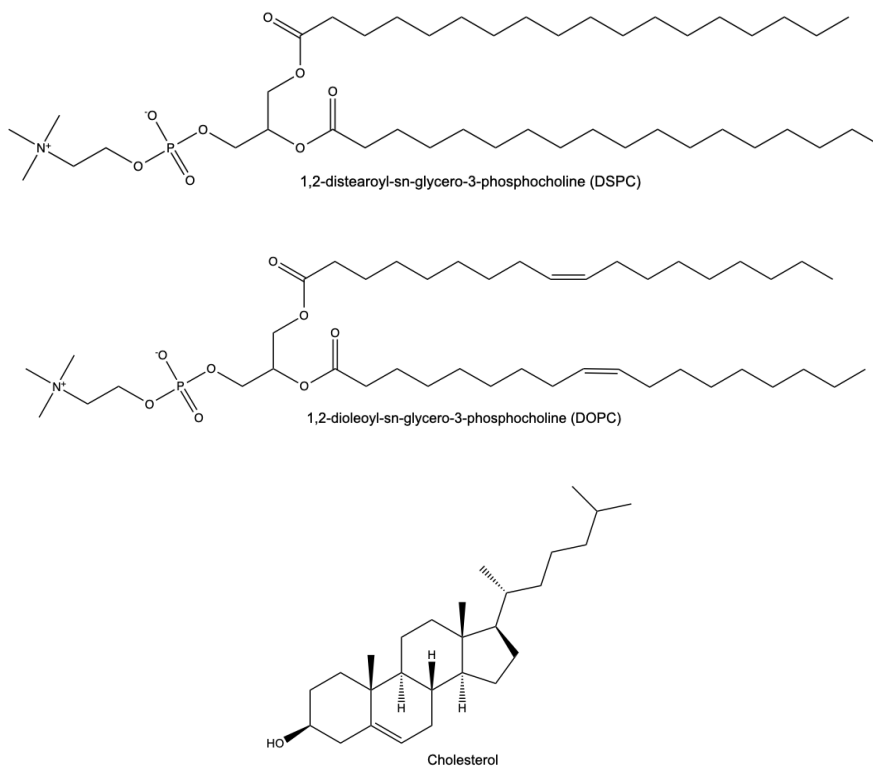
Figure 2.1: Skeletal structures of various common in biology and in molecular simulation.

Depending on the strength of interaction and molecular size, lipids can aggregate into a variety of structures including micelles, bilayers, and reverse micelles.[17] Micelles are spherical structures where the hydrophilic head groups are larger than the hydrophobic tail (micelles generally form from components with one tail). The head groups are on the exterior of the micelle while the tails are on the interior. If the hydrophobic tails become larger (bilayers generally form from components with two tails), the lipids can form bilayers. In bilayers, the hydrophilic head groups are still oriented outwards toward water and the tails are still oriented inwards toward each other, but the relative sizes yield more planar and less spherical structures (see Figure 2.2). In reverse micelles, the hydrophobic tails cannot pack internally as in micelles or bilayers (reverse micelles generally form from components with more than two tails). While still spherical, reverse micelle hydrophobic tails now orient outwards to the water and the hydrophilic head groups are oriented inwards.
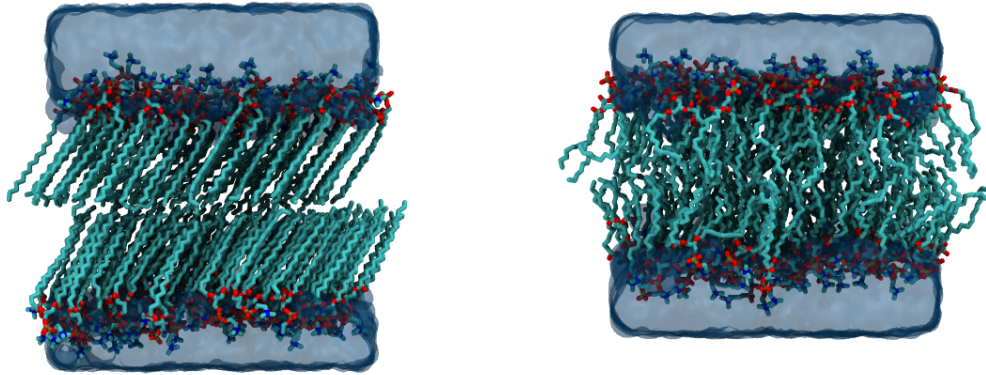
Figure 2.2: Simulation renderings of lipid bilayers in two phases (gel, left; fluid, right). Bulk water is shown on the top and bottom of the figures. Lipids are seen in the middle of the figures, with head groups oriented outwards toward the water and tail groups oriented inwards toward each other.

2.3   Bilayer Phases

For bilayers, a variety of phases can be observed,[18] that depend on factors such as melting temperature, hydration, and composition. The phases can be characterized by their lipid organization (configuration of the tails) and their lipid lateral diffusion (how mobile the lipids are within the plane of the leaflet). Figure 2.2 shows some simulation renderings of two bilayer phases. Figure 2.3 depicts some additional bilayer phases.
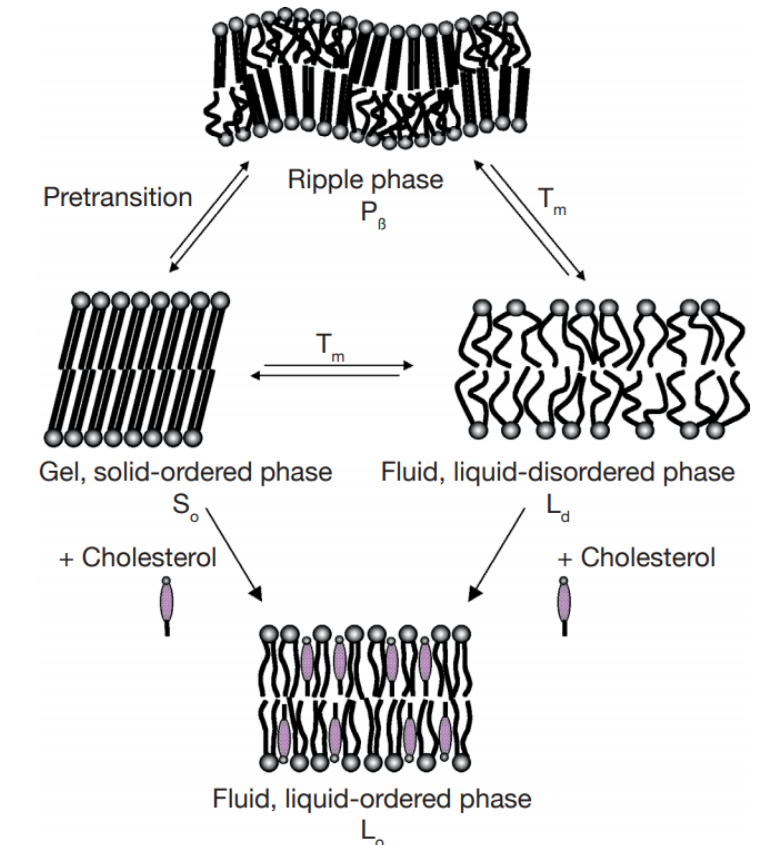
Figure 2.3: Various bilayer phases depending on composition and temperature. Image reproduced from Eeman *et al.* with permission from Les Presses agronomiques de Gembloux.

For a given bilayer below its melting point, the bilayer occupies a gel (L_β) or solid-ordered (S_o) phase. In the gel phase, lipid tails are highly ordered – tails are in the all-*trans* configuration and elongated. This tail organization allows lipids to pack very tightly, thus immobilizing the lipids and yielding diffusion coefficients on the order of 10^{-11} or $10^{-12} \frac{cm^2}{sec}$.[19,20] Gel-phase bilayers also demonstrate greater thicknesses and lower permeabilities to water and solutes.[21] Furthermore, within the gel phase, some lipids with sufficiently large head groups can uniformly tilt up to 30° with respect to the bilayer normal,

creating the tilted-gel (L'_β) phase.[22,23]

Above the melting temperature, bilayers occupy a fluid phase (L_α).[24] In fluid phases, the tails are more disordered due to the presence of *gauche* configurations. Due to the *gauche* defects, lipids do not pack as tightly compared to those in the gel phase, and lateral diffusion coefficients rise to the order of 10^{-7} or $10^{-8}\frac{cm^2}{sec}$. More specifically within the fluid phase, lipids can occupy the liquid-disordered (L_d) or liquid-ordered (L_o) phase. As the names suggest, the liquid-ordered phase possesses greater ordering than the liquid-disordered phase. The formation of the liquid-ordered phase can be attributed to the presence of cholesterol, whose stiff rings and inverted-cone shape disturb the packing of the gel phase, but fill the free space and facilitate packing within the fluid phase.[20,21,25]

The ripple phase (P_β) is generally considered to be a transition or coexistence phase between gel and fluid phase.[20,24] In the ripple phase, some bilayer nanodomains display gel-phase properties, while others display fluid-phase properties. The ripples arise from the different structural and mechanical properties imparted by the gel and fluid regions.

Melting temperature and phase behavior can depend on degree of un-saturation (presence of double bonds) and acyl chain length.[21,24,26] The presence of double bonds within the lipid tails results in more *gauche* defects, thus lowering the melting temperature and facilitating the formation of the fluid phase, while increased chain length facilitates lipid tail ordering, thus increasing the melting temperature and facilitating the formation of the gel phase.[20,24,26]

2.4   Lipid Membranes in the Stratum Corneum

Our skin is the primary transport barrier against external permeants – in particular, the outermost layer of the skin, the stratum corneum (SC), contributes significantly to skin barrier function.[27] The SC is often described using a brick and mortar model, where the bricks consist of corneocytes and the mortar consists of a lipid matrix of multilayers composed of ceramides (CER), cholesterol (CHOL), and free fatty acids (FFA).[8] The SC lipids demon-

strate phase heterogeneity with various lamellar organization and periodicities (short and long) in addition to various lateral organization and lattice behavior (hexagonal and orthorhombic).[6] In general, the strong ordering and immobile behavior of these layers are characteristic of gel and crystalline phases.[28–30] It has been reported that the SC's primary contribution to barrier function comes from the lipid matrix.[27] When the lipid matrix composition is altered and lateral and lamellar organization of the SC are compromised, various ailments can result, including atopic dermatitis, lamellar ichthyosis, and dry skin.[12,31]

The role of SC lipid composition on lateral packing, lamellar organization, and barrier properties has been extensively studied.[9,12,32–38] Within the SC, the optimum lipid packing (as examined by X-ray diffraction) that yields the best barrier properties tends to be the orthorhombic phase, while facilitating transitions to a hexagonal phase reduces barrier function.[9,12,35,37,38] Furthermore, reduced conformational disordering (as measured by FTIR methylene stretching around 2850 cm^{-1}) tends to be associated with the orthorhombic phase and better barrier function.[9,12,35,37,38] Longer-tailed CER and FFA have been associated with orthorhombic packing and lower conformational disorder.[9,12,37,38] In terms of lamellar organization of the SC, promoting the long periodicity phase (repeat distance ~13 nm) tends to improve barrier function, where shorter chains are not associated with the long periodicity phase (LPP) and, in the case of short FFA chains, can form separate lamella.[36,37]

In situations where the SC lipid composition, lateral packing, or lamellar organization are compromised, various moisturizers have been proposed to restore these properties. Commonly studied moisturizers include isostearyl isostearate (ISIS), isopropyl isostearate (IPIS), and glycerol monoisostearate (GMIS).[34] Among this group, ISIS appeared to yield the best barrier properties in experimental SC models, as it occasionally incorporated into the LPP (though sometimes formed separate lamellar domains), did not inhibit formation of the LPP, and promoted orthorhombic packing (though formation of separate lateral domains has yet to be determined). The question still remains, what other moisturizers exist

that can restore healthy SC or supplement SC barrier function?

Focusing on a particular skin condition, dry skin issues afflict as much as 40% of the population.[35] To address dry skin, scientists have made efforts in designing formulations that can mimic the excellent barrier function of healthy SC; these formulations of interest often exhibit a gel phase at ambient temperatures. Due to cost and synthetic considerations, researchers have opted to use other gel-forming lipids to mimic healthy SC, including phospholipids.[31,39,40]

Various studies have reported the relationship between composition, structure, and function of bilayer-forming lipids within the gel phase.[41–48]

2.4.0.1 Experimental Studies of Gel-Phase Phospholipids

Most experimental work involving gel-phase phospholipids utilizes X-ray diffraction (XRD) and electron density modeling. Some of the earliest work came from Tardieu *et al.*,[18] who used XRD to examine lipids found within egg lecithin and mitochondria. They developed early phase diagrams involving tilted-gel, gel, and liquid phases in addition to reporting phase transition temperatures. Even within some gel phases, a liquid layer was observed in the middle of the bilayer due to "length heterogeneity". Furthermore, structural properties including lattice parameters, bilayer thicknesses, and tilt angles. Lis *et al.*[49] and Rand *et al.*[50] rationalized these bilayer structural properties as a balance of hydration, van der Waals, and electrostatic forces. In 1989, Wiener *et al.*[51] utilized XRD, wide-angle X-ray scattering, and electron density modeling to study properties of fully-hydrated gel-phase phospholipids (dipalmitoylphosphatidylcholine, DPPC) at greater resolution, reporting not only areas, chemical group volumes, and tilt angles, but also the number of waters hydrating each lipid ($\sim$10 waters per lipid). More up-to-date structural data for DPPC and dimyristoylphosphatidylcholine (DMPC) can be found in Tristram-Nagle[22] and Nagle *et al.*[52] In 1993, Tristram-Nagle *et al.*[53] examined the dependence of these properties on the chain lengths of the phospholipids, characterizing these trends as a function of van der

Waals forces and repulsive excluded-volume interactions that arise from additional methylene groups. Increasing the chain length was found to increase the numbers of water per lipid, area per lipid, bilayer thickness, and tilt angle. Building off the chain-length dependency, Sun *et al.*[54] studied the temperature dependency of bilayers within the gel phase, observing temperature to increase bilayer thickness, increase chain packing, and decrease tilt angle while having no effect on head group and interface properties. The ripple phase has been preliminarily studied, observing mixed fluid and gel regions and the formation of *gauche-trans-gauche* kinks that contribute to the different arms within the ripple phase.[55]

2.4.0.2 Theoretical Studies of Permeation through Gel-Phase Phospholipids

Multiple theories and models have been proposed to describe and predict permeation events through gel-phase and crystalline phospholipids. This section describes two such theories.

One theory involves utilizing solubility-diffusion models to describe the various regions within the bilayer.[56,57] In this framework, hydrophilic (head group) regions and hydrophobic (tail) regions are treated separately, but summed up to yield an effective resistance to permeation. This methodology accounts for both thermodynamic and transport considerations within permeability. Depending on the region of the bilayer, the free energy and diffusive barriers will be more or less favorable to permeation.

Another theory, the Trauble-Haines-Liebowitz model, involves the formation of *gauche-trans-gauche* configurations (kinks) within lipid chains on a lattice. While some permeants do not fit these kinks and pores might be more appropriate to describe permeation of that size, water molecules can fit within these kinks.[58–62] According to this theory, water transports through crystalline-like bilayers depending on the motion and creation of chain kinks (see Figure 2.4). The creation of these kinks first depends on head group motion; the displacement of a head group first generates a space that causes the phospholipid ester groups (at the beginning of the tails) to shift, forming the kink. The kink then proceeds down the

lipid chains, serving as a pathway for water transport. Flory claimed that the *gauche-trans-gauche* configuration was a low energy motion for chain polymers.[63] The propagation of the kink is believed to occur at relatively fast rates compared to the initial motion in the head groups required to create the first kink. Thus, the rate limiting step appears to be associated with the motion of the head groups, which is strongly tied to the lateral diffusion of the lipids.
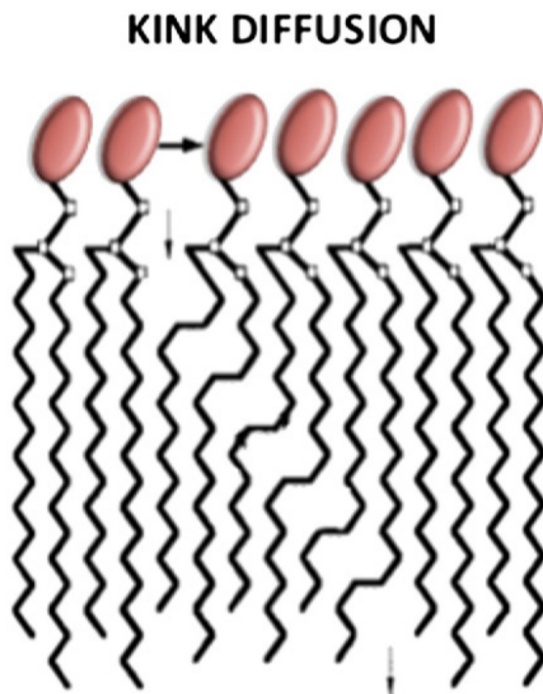
KINK DIFFUSION

Figure 2.4: Schematic describing kink diffusion through crystalline phospholipid bilayers. The schematic depicts a single lipid as it laterally shifts and vertically propagates the kink. Image reproduced from Disalvo *et al.* with permission from ElSevier.

Chain configurations can be measured via FTIR, which helped corroborate this theory.[62] Furthermore, Paula *et al.* observed permeation of small, polar molecules to be weak depend on bilayer thickness.[61] This model also explains that kinks cannot diffuse through double bonds.[59,60] This model also rationalizes cholesterol's permeability-diminishing property as a result of significantly decreasing chain motion despite accelerating head group motion.[60] Interestingly, Haines hypothesized *iso* or *anteiso* lipids with methyl branches near the terminal positions could prevent the formation of stable gel phases[60] – although,

at the time, no water permeability studies for these compounds were reported. On the other hand, more recently, methyl-branched compounds like ISIS appear to facilitate the gel-phase behavior within the SC.[33,34]

2.4.0.3 Simulation Studies of Gel-Phase Phospholipids

While it is clear a relationship exists between composition, structure, and function for these bilayer systems in topical applications, there is a lack of molecular understanding in how certain components alter bilayer structure, packing, and permeability. The research so far has demonstrated that adding certain components to these bilayers can produce densely-packed lipids that improve barrier function, but the research does not sufficiently explain this phenomenon at a molecular level – experimental research can typically report macroscopic properties, but not nanoscopic, molecular properties like atomic positions or orientations. In this regard, molecular simulation can provide insight. Molecular simulation provides direct information into the coordinates and forces of each atom, as well as a framework to systematically study the influence of individual variables or components on bilayer structure and permeability. A necessary component of a molecular simulation is an accurate description of a system's potential energy (force field). Force fields must reliably describe the energetic interactions for the system of interest, and common force fields have steadily been expanding support for gel-phase lipids, including OPLS,[48,64] AMBER,[65] GROMOS,[45–47,66] and CHARMM.[67–70] However, due to the computational expense of simulating gel-phase systems with low mobility, there has been little published work on simulations of gel-phase lipids compared to those of fluid-phase lipids, and the works on gel-phase lipids are mostly focused on ceramide-based bilayers and not phospholipid-based bilayers.[28,48,71–76] Computational studies of gel-phase phospholipids[45–47] have shown some trends with respect to adding fatty alcohol components. For example, larger head groups introduce greater steric repulsions and increase bilayer area per lipid; longer tails introduce greater van der Waals attractions, increase tilt angle, and

improve lipid tail packing; asymmetric tails facilitate interdigitation between leaflets.[45,46] Newer studies suggest water barrier properties are influenced by interfacial properties, including hydrogen bonding and water dynamics.[47] but a large remainder of chemical space has yet to be explored.

2.5 Lipid Bilayers Comprising the Cell Membrane

Eukaryotic cells and cell organelles are surrounded by plasma membranes (cellular membranes) whose functions include signaling and transport. The composition of the cell membranes (lipids and transmembrane proteins) found throughout nature will depend on the environment and particular nature of signaling and transport. The composition within a single cell membrane is also very heterogeneous, with a mixture of liquid-disordered and liquid-ordered phases.[21,25,77] Some nanodomains, dubbed rafts, also have roles in particular biological pathways.[21] Thus, the phase heterogeneity in cellular membranes is key for certain functions to be performed.

One particular function relevant to cell membranes is synaptic and neurotransmission.[78–81] Cholesterol has been reported to be relevant for proper synaptic vesicle function, possibly due to cholesterol's role in organizing the local membrane environment.[78,81] Whether the key property for neurotransmission is the presence of cholesterol or the resultant liquid-ordered phase is an ongoing field of research,[78,79] though it is clear the relevance of composition and phase behavior for a key biological function.

While there are numerous methods to indirectly characterize local cholesterol content and membrane phase behavior,[78,79] simulations serve as an atomistic microscope, allowing direct observation and quantification of these local behaviors of lipid bilayers at the nanoscale,[82–89] especially as computational hardware and techniques improve the accuracy and reliability of molecular simulation. Thus, it is now feasible to examine the various influences of composition and phase behavior on lipid bilayers with more complex chemistries.

In particular, graphene (a 2-dimensional lattice of carbon) is hypothesized to localize cholesterol and facilitate formation of the liquid-ordered phase, which could impact neurotransmission.[78,79] Molecular simulation can be used to elucidate this nanoscale behavior and better study graphene-bilayer interactions. So far, preliminary computational studies have observed graphene's cytotoxic effects on cellular membranes.[82,83] Can biocompatible applications of graphene be developed to mitigate cytotoxic side effects without compromising desirable effects? To date, there have been no computational studies examining methods to mitigate graphene's cytotoxic effects on cellular membranes and improve graphene's range of biocompatible applications.

2.6 Bibliography

[1] Geoffrey M. Geise, Donald R. Paul, and Benny D. Freeman. "Fundamental water and salt transport properties of polymeric materials". In: *Progress in Polymer Science* 39.1 (2014), pp. 1–42.

[2] Qunhui Guo et al. "Sulfonated and crosslinked polyphosphazene-based proton-exchange membranes". In: *Journal of Membrane Science* 154.2 (1999), pp. 175–181.

[3] Scott D Campbell, Karen J Regina, and Evan D Kharasch. "Significance of lipid composition in a blood-brain barrier-mimetic PAMPA assay." In: *Journal of biomolecular screening* 19.3 (2014), pp. 437–44.

[4] J A Bouwstra et al. "Phase behavior of isolated skin lipids". In: *Journal of Lipid Research* 35.5 (1995), pp. 999–1011.

[5] J A Bouwstra et al. "Phase behavior of lipid mixtures based on human ceramides: Coexistence of crystalline and liquid phases". In: *Journal of Lipid Research* 42.11 (2011), pp. 1759–1770.

[6] J. Bouwstra, G. Gooris, and M. Ponec. "The lipid organisation of the skin barrier: Liquid and crystalline domains coexist in lamellar phases". In: *Journal of Biological Physics* 28.2 (2002), pp. 211–223.

[7] Joke A. Bouwstra et al. *Structure of the skin barrier and its modulation by vesicular formulations*. Vol. 42. 1. 2003, pp. 1–36.

[8] Charlotte M Beddoes, Gert S Gooris, and Joke A Bouwstra. "Preferential arrangement of lipids in the long periodicity phase of a stratum corneum matrix model." In: *Journal of lipid research* (2018), jlr.M087106.

[9] Masayuki Uchiyama et al. "Free fatty acids chain length distribution affects the permeability of skin lipid model membranes". In: *Biochimica et Biophysica Acta - Biomembranes* 1858.9 (2016), pp. 2050–2059.

[10] Daniël Groen et al. "Two new methods for preparing a unique stratum corneum substitute". In: *Biochimica et Biophysica Acta - Biomembranes* 1778.10 (2008), pp. 2421–2429.

[11] E.H. Mojumdar et al. "Stratum corneum lipid matrix: location of acyl ceramide and cholesterol in the unit cell of the long periodicity phase". In: *Biochimica et Biophysica Acta (BBA) - Biomembranes* 1858.8 (2016), pp. 1926–1934.

[12] Gonneke S K Pilgram et al. "Aberrant Lipid Organization in Stratum Corneum of Patients with Atopic Deramtitis and Lamellar Ichthyosis". In: *Journal of Investigative Dermatology* 117.3 (2001), pp. 710–717.

[13] G. S. Gooris et al. "Interactions of dipalmitoylphosphatidylcholine with ceramide-based mixtures". In: *Biochimica et Biophysica Acta - Biomembranes* 1860.6 (2018), pp. 1272–1281. arXiv: S0005273618300658.

[14] Eduard J. Stadelmann and Ok Young Lee-Stadelmann. "Passive permeability". In: *Methods in Enzymology* 174.C (1989), pp. 246–266.

[15] D. Liu and S. Case. "Durability study of proton exchange membrane fuel cells under dynamic testing conditions with cyclic current profile". In: *Journal of Power Sources* 162.1 (2006), pp. 521–531.

[16] Kah Peng Lee, Tom C. Arnot, and Davide Mattia. "A review of reverse osmosis membrane materials for desalination-Development to date and future potential". In: *Journal of Membrane Science* 370.1-2 (2011), pp. 1–22.

[17] Jacob N. Israelachvili. *Intermolecular and Surface Forces*. 3rd ed. Academic Press Inc., 2011.

[18] A. Tardieu, Vittorio Luzzati, and F. C. Reman. "Structure and polymorphism of the hydrocarbon chains of lipids: A study of lecithin-water phases". In: *Journal of Molecular Biology* 75.4 (1973), pp. 711–733.

[19] John L R Rubenstein, Barton A Smith, and Harden M Mcconnell. "Lateral diffusion in binary mixtures of cholesterol and phosphatidylcholines". In: *Proceedings of the National Academy of Sciences USA* 76.1 (1979), pp. 15–18.

[20] Marc Eeman and Magali Deleu. "From biological membranes to biomimetic model membranes". In: *Biotechnologie, Agronomie, Société et Environnement/Biotechnology, Agronomy, Society and Environment* 14.4 (2010), pp. 719–736.

[21] Sushmita Mukherjee and Frederick R Maxfield. "Membrane Domains". In: *Annu. Rev. Cell Dev. Biol* 20 (2004), pp. 839–66.

[22] Stephanie Tristram-Nagle et al. "Structure of gel phase DMPC determined by x-ray diffraction". In: *Biophysical Journal* 83.6 (2002), pp. 3324–3335.

[23] S. Tristram-Nagle and John F. Nagle. "Structure of lipid bilayers". In: *Biochimica et biophysica acta* 1469.3 (2000), pp. 159–195. arXiv: NIHMS150003.

[24] Marieke Kranenburg and Berend Smit. "Phase behavior of model lipid bilayers". In: *Journal of Physical Chemistry B* 109.14 (2005), pp. 6553–6563.

[25] Gerald W Gw Feigenson. "Phase boundaries and biological membranes". In: *Annual review of biophysics and biomolecular structure* 36 (2007), pp. 63–77.

[26] S. G. Clerc and T. E. Thompson. "Permeability of dimyristoyl phosphatidylcholine/dipalmitoyl phosphatidylcholine bilayer membranes with coexisting gel and liquid-crystalline phases". In: *Biophysical Journal* 68.6 (1995), pp. 2333–2341.

[27] A. S. Michaels, S. K. Chandrasekaran, and J. E. Shaw. "Drug permeation through human skin: Theory and invitro experimental measurement". In: *AIChE Journal* 21.5 (1975), pp. 985–996.

[28] Timothy C. Moore et al. "Effect of Ceramide Tail Length on the Structure of Model Stratum Corneum Lipid Bilayers". In: *Biophysical Journal* 114.1 (2018), pp. 113–125.

[29] B. O. Forslind. *A domain mosaic model of the skin barrier*. 1994.

[30] Lars Norlen. "Skin Barrier Structure and Function: The Single Gel Phase Model". In: *The Journal of Investigative Dermatology* 117.4 (2001), pp. 830–836.

[31] G. Pennick et al. "The effect of an amphiphilic self-assembled lipid lamellar phase on the relief of dry skin". In: *International Journal of Cosmetic Science* 34.6 (2012), pp. 567–574.

[32] A. V. Rawlings and C. R. Harding. "Moisturization and skin barrier function". In: *Dermatologic Therapy* 17 (2004), pp. 43–48.

[33] J. Caussin et al. "Interaction of lipophilic moisturizers on stratum corneum lipid domains in vitro and in vivo". In: *Skin Pharmacology and Physiology* 20.4 (2007), pp. 175–186.

[34] Julia Caussin, Gert S. Gooris, and Joke A. Bouwstra. "FTIR studies show lipophilic moisturizers to interact with stratum corneum lipids, rendering the more densely packed". In: *Biochimica et Biophysica Acta - Biomembranes* 1778.6 (2008), pp. 1517–1524.

[35] G Pennick et al. "Superior effect of isostearyl isostearate on improvement in stratum corneum water permeability barrier function as examined by the plastic occlusion stress test". In: *International Journal of Cosmetic Science* 32.4 (2010), pp. 304–312.

[36] D Groen et al. "Is an orthorhombic lateral packing and a proper lamellar organization important for the skin barrier function?" In: *Biochimica et Biophysica Acta - Biomembranes* 1808.6 (2011), pp. 1529–1537.

[37] E. H. Mojumdar et al. "The role of ceramide chain length distribution on the barrier properties of the skin lipid membranes". In: *Biochimica et Biophysica Acta - Biomembranes* 1838.10 (2014), pp. 2473–2483.

[38] Barbora Školová et al. "Different phase behavior and packing of ceramides with long (C16) and very long (C24) acyls in model membranes: Infrared spectroscopy using

deuterated lipids". In: *Journal of Physical Chemistry B* 118.35 (2014), pp. 10460–10470.

[39] P. A. Bulsara et al. "The rational design of biomimetic skin barrier lipid formulations using biophysical methods". In: *International Journal of Cosmetic Science* 39.2 (2017), pp. 206–216.

[40] Robert S. Summers et al. "The effect of lipids, with and without humectant, on skin xerosis". In: *Journal of the Society of Cosmetic Chemists* 47.February (1996), pp. 27–39.

[41] Eric Wang and Jeffery B. Klauda. "Molecular Dynamics Simulations of Ceramide and Ceramide-Phosphatidylcholine Bilayers". In: *Journal of Physical Chemistry B* 121.43 (2017), pp. 10091–10104.

[42] Eric Wang and Jeffery B. Klauda. "Structure and Permeability of Ceramide Bilayers and Multilayers". In: *Journal of Physical Chemistry B* 123.11 (2019), pp. 2525–2535.

[43] Eric Wang and Jeffery B. Klauda. "Simulations of Pure Ceramide and Ternary Lipid Mixtures as Simple Interior Stratum Corneum Models". In: *Journal of Physical Chemistry B* (2018).

[44] Eric Wang and Jeffery B. Klauda. "Models for the Stratum Corneum Lipid Matrix: Effects of Ceramide Concentration, Ceramide Hydroxylation, and Free Fatty Acid Protonation". In: *Journal of Physical Chemistry B* 122.50 (2018), pp. 11996–12008.

[45] Remco Hartkamp et al. "Investigating the Structure of Multicomponent Gel-Phase Lipid Bilayers". In: *Biophysical Journal* 111.4 (2016), pp. 813–823.

[46] Remco Hartkamp et al. "Structural Properties of Phospholipid-based Bilayers with Long- Chain Alcohol Molecules in the Gel Phase". In: *Journal of Physical Chemistry B* 120.50 (2016), pp. 12863–12871.

[47] Remco Hartkamp et al. "Composition Dependence of Water Permeation Across Multicomponent Gel-Phase Bilayers". In: *Journal of Physical Chemistry B* 122.12 (2018), pp. 3113–3123.

[48] Chinmay Das, Peter D Olmsted, and Massimo G Noro. "Water permeation through stratum corneum lipid bilayers from atomistic simulations". In: *Soft Matter* 5.22 (2009), p. 8. arXiv: 0907.1664.

[49] L J Lis et al. "Interactions between neutral phospholipid bilayer membranes." In: *Biophysical journal* 37.3 (1982), pp. 657–65.

[50] R.P. Rand and V.A. Parsegian. "Hydration forces between phospholipid bilayers". In: *BBA - Reviews on Biomembranes* 988.3 (1989), pp. 351–376.

[51] M. C. Wiener, R. M. Suter, and J. F. Nagle. "Structure of the fully hydrated gel phase of dipalmitoylphosphatidylcholine". In: *Biophysical Journal* 55.2 (1989), pp. 315–325.

[52] John F Nagle et al. "Structure of gel phase DPPC determined by X-ray diffraction". In: *Chemistry and Physics of Lipids* 218.6 (2019), pp. 168–177.

[53] S. Tristram-Nagle et al. "Measurement of chain tilt angle in fully hydrated bilayers of gel phase lecithins". In: *Biophysical Journal* 64.4 (1993), pp. 1097–1109.

[54] W. J. Sun et al. "Structure of gel phase saturated lecithin bilayers: temperature and chain length dependence." In: *Biophysical journal* 71.2 (1996), pp. 885–891.

[55] K. Akabori and J. F. Nagle. "Structure of the DMPC lipid bilayer ripple phase". In: *Soft Matter* 11.5 (2015), pp. 918–926. arXiv: 15334406.

[56] Siewert-Jan Marrink and Herman J. C. Berendsen. "Simulation of water transport through a lipid membrane". In: *Journal of Physical Chemistry* 98.15 (1994), pp. 4155–4168.

[57] John F Nagle et al. "Theory of passive permeability through lipid bilayers." In: *The Journal of general physiology* 131.1 (2008), pp. 77–85.

[58] Thomas H. Haines. "A Model for Transition State Dynamics in Bilayers: Implications for the Role of Lipids in Biomembrane Transport". In: *Biophysical Journal* 37.1 (1982), pp. 147–148.

[59] Thomas H Haines. "Water Transport Across Biological Membranes". In: *FEBS Letters* 346 (1994), pp. 115–122.

[60] Thomas H. Haines and L. S. Liebovitch. "Permeability and Stability of Lipid Bilayers". In: *Permeability and Stability of Lipid Bilayers*. Ed. by E. A. Disalvo and S. A. Simon. CRC Press, 1994. Chap. 6, pp. 123–136.

[61] S. Paula et al. "Permeation of Protons, Potassium Ions, and Small Polar Molecules Through Phospholipid Bilayers as a Function of Membrane Thickness". In: *Biophysical Journal* 70.January (1996), pp. 339–348.

[62] E. A. Disalvo et al. "Functional role of water in membranes updated: A tribute to Träuble". In: *Biochimica et Biophysica Acta - Biomembranes* 1848.7 (2015), pp. 1552–1562.

[63] Paul J. Flory. *Statistical Mechanics of Chain Molecules*. New York: Interscience, 1969.

[64] William L. Jorgensen, David S. Maxwell, and Julian Tirado-Rives. "Development and Testing of the OLPS All-Atom Force Field on Conformational Energetics and Properties of Organic Liquids". In: *J. Am. Chem. Soc.* 118.15 (1996), pp. 11225–11236.

[65] Callum J. Dickson et al. "Lipid14: The Amber Lipid Force Field - Supplementary Data". In: *Journal of Chemical Theory and Computation* 10.2 (2014), pp. 865–879.

[66] David Poger, Wilfred F. van Gunsteren, and Alan E. Mark. "A New Force Field for Simulating Phosphatidylcholine Bilayers". In: *Journal of computational chemistry* 31.6 (2009), pp. 1117–1125. arXiv: NIHMS150003.

[67] Richard M. Venable, Bernard R. Brooks, and Richard W. Pastor. "Molecular dynamics simulations of gel (LβI) phase lipid bilayers in constant pressure and constant surface area ensembles". In: *The Journal of Chemical Physics* 112.10 (2002), pp. 4822–4832.

[68] Scott E. Feller and Richard W. Pastor. "Constant surface tension simulations of lipid bilayers: The sensitivity of surface areas and compressibilities". In: *Journal of Chemical Physics* 111.3 (1999), pp. 1281–1287.

[69] Jeffery B. Klauda et al. "Simulation-based methods for interpreting x-ray data from lipid bilayers". In: *Biophysical Journal* 90.8 (2006), pp. 2796–2807.

[70] Alison N. Leonard et al. "Developing and Testing of Lipid Force Fields with Applications to Modeling Cellular Membranes". In: *Chemical Reviews* 119.9 (2019), pp. 6227–6269.

[71] Sagar A. Pandit and H. Larry Scott. "Molecular-dynamics simulation of a ceramide bilayer". In: *Journal of Chemical Physics* 124.1 (2006), pp. 1–7.

[72] Nikolaos I. Papadimitriou et al. "Studying the structure of single-component ceramide bilayers with molecular dynamics simulations using different force fields". In: *Molecular Simulation* 7022.May 2016 (2014), pp. 1–15.

[73] Markéta Paloncyová et al. "Rationalization of reduced penetration of drugs through ceramide gel phase membrane". In: *Langmuir* 30.46 (2014), pp. 13942–13948.

[74] Rakesh Gupta and Beena Rai. "Molecular Dynamics Simulation Study of Skin Lipids: Effects of the Molar Ratio of Individual Components over a Wide Temperature Range". In: *The Journal of Physical Chemistry B* 119.35 (2015), pp. 11643–11655.

[75] Huanjie Wang and Fancui Meng. "The permeability enhancing mechanism of menthol on skin lipids: a molecular dynamics simulation study". In: *Journal of Molecular Modeling* (2017).

[76] Shan Guo et al. "Simulation study of the structure and phase behavior of ceramide bilayers and the role of lipid head group chemistry." In: *Journal of chemical theory and computation* 9.11 (2013), pp. 5116–5126.

[77] David G Ackerman and Gerald W Feigenson. "Lipid Bilayers: Clusters, Domains and Phases". In: *Essays BIochem.* 57 (2015), pp. 33–42.

[78] Kristina E. Kitko et al. "Regulation of Lipid Membrane Trafficking and Transmembrane Signaling by Graphene". In: *Biophysical Journal* 108.2 (2015), 187a.

[79] Kristina E. Kitko et al. "Membrane cholesterol mediates the cellular effects of monolayer graphene substrates". In: *Nature Communications* 9.1 (2018).

[80] Jeffrey S. Dason et al. "Vesicular sterols are essential for synaptic vesicle cycling". In: *Journal of Neuroscience* 30.47 (2010), pp. 15856–15865.

[81] Dmytro Puchkov and Volker Haucke. "Greasing the synaptic vesicle cycle by membrane lipids". In: *Trends in Cell Biology* 23.10 (2013), pp. 493–503.

[82] Yusong Tu et al. "Destructive extraction of phospholipids from Escherichia coli membranes by graphene nanosheets". In: *Nature Nanotechnology* 8.8 (2013), pp. 594–601.

[83] Liuyang Zhang, Bingqian Xu, and Xianqiao Wang. "Cholesterol Extraction from Cell Membrane by Graphene Nanosheets: A Computational Study". In: *The Journal of Physical Chemistry B* 120.5 (2016), pp. 957–964.

[84] W.F. Drew Bennett and D. Peter Tieleman. "Computer simulations of lipid membrane domains". In: *Biochimica et Biophysica Acta (BBA) - Biomembranes* 1828.8 (2013), pp. 1765–1776.

[85] Timothy S Carpenter et al. "Capturing Phase Behavior of Ternary Lipid Mixtures with a Refined Martini Coarse-Grained Force Field". In: *Journal of Chemical Theory and Computation* (2018), acs.jctc.8b00496.

[86] E Egberts, S J Marrink, and H J Berendsen. "Molecular dynamics simulation of a phospholipid membrane." In: *European biophysics journal : EBJ* 22 (1994), pp. 423–436. arXiv: NIHMS150003.

[87] Roland Faller and Siewert Jan Marrink. "Simulation of domain formation in DLPC-DSPC mixed bilayers". In: *Langmuir* 20.18 (2004), pp. 7686–7693.

[88] Siewert J Marrink and D Peter Tieleman. "Perspective on the Martini model." In: *Chemical Society reviews* 42.16 (2013), pp. 6801–6822.

[89] Christopher T Boughter et al. "Influence of Cholesterol on Phospholipid Bilayer Structure and Dynamics". In: *The Journal of Physical Chemistry B* (2016), acs.jpcb.6b08574.

Chapter 3

Composition-Structure Relationships in Gel-Phase Bilayers

3.1 Introduction

Gel-phase phospholipid bilayers are often used in cosmetic and pharmaceutical formulations as topical treatments, designed to retain moisture by mimicking the barrier function of healthy skin. Typically, phospholipid bilayers are composed of lipids with unsaturated tails. Under ambient conditions, these bilayers occupy a liquid-crystalline phase. However, lipids with fully saturated tails have been observed to occupy a gel phase in which the lipids are highly ordered and fairly immobile.[1] Gel-phase, ceramide-based multilayers in the stratum corneum (outermost layer of the skin) have demonstrated excellent barrier properties due to their dense packing.[2–5] Various formulations and moisturizers, some including phospholipids, have been shown to contribute to the gel-phase behavior of the stratum corneum and boost barrier function.[4,6–10] Designing such formulations first requires an understanding of how the individual lipids, and their relative composition, influences the structure and properties of the bilayer.

To date, several experimental methods have been utilized to study the structure and properties of gel-phase lipid bilayers. Early observations of various bilayers were reported by Tardieu *et al.*, who characterized lattice parameters and tilt angels in gel and tilted-gel phases.[1] Early work by Lis *et al.* characterized force versus separation distance between different gel-phase bilayers, identifying an exponentially decaying "hydration repulsion," which was found to depend on phospholipid polar groups and packing of the hydrocarbon acyl chains.[11] Later, Rand and Parsegian explored water uptake and bilayer properties versus relative humidity, rationalizing the behavior via hydration, electorstatic, undulation, steric, and van der Waals forces and noting that hydration forces help drive phase transition

behavior and bilayer order.[12] The hydration force was used to rationalize bilayer thickness trends, hydrocarbon tilt, and surface area per head group.[13] Sun *et al.* utilized small-angle and wide-angle X-ray scattering experiments to study gel-phase, saturated lipids, observing that increasing chain length increases area per chain, tilt angle, and bilayer thickness.[14–16] Using electron density modeling, Wiener *et al.* determined methylene and head group volumes, bilayer thicknesses, and hydration within gel-phase phospholipids, demonstrating the utility of electron density modeling to examine gel-phase bilayers.[17] In addition to phospholipids occupying the gel phase, Akabori and Nagle also reported a ripple phase of phospholipids, further emphasizing the variegated behavior of phospholipid bilayers.[18]

Experimental lipid bilayer studies have also considered mixed lipid systems. For example, Hishida *et al.*, in numerous studies, observed that the addition of n-alkanes can rigidify bilayers, alter bilayer transition temperatures, and also influence phase separation (in a manner different from cholesterol).[19–21] Aagaard *et al.* observed the ability of alkanes and alcohols to affect fluid-phase bilayer packing properties and volume in different ways depending on chain length relative to the bilayer-forming lipid (14 carbons).[22] Ingolfsson and Andersen further explored this property with longer bilayer-forming lipids (22 carbons) and a greater variety of alcohol chain lengths, identifying the different behaviors between short and long-chain alcohols when looking at how alcohols stabilize membrane-protein interactions.[23] Additional experiments have demonstrated the ability of short-chain alcohols to disorder and disrupt the structural and mechanical properties of fluid-phase lipid membranes.[24,25] In fluid-phase systems, cholesterol is known to increase orientational order in phospholipid tails, reduce lipid lateral diffusion, improve packing, and thus influence solute permeability.[26] Other experimental evidence suggests that the addition of fatty acid components can alter the morphology of pure gel-phase phospholipids from tilted and rippled phases into untilted, gel-phases.[27]

While it is clear a relationship exists between composition, structure, and function in gel-phase, phospholipid-based bilayer systems, there is a lack of molecular understanding

with respect to how certain components affect bilayer structure. In this regard, molecular simulation can be a powerful tool, providing direct access to the spatial coordinates and interactions of each atom over time while serving as an effective platform for a systematic comparison of similar systems with slightly different compositions. While there is extensive simulation literature for fluid-phase lipid bilayers, we restrict our focus to simulations of gel-phase lipid bilayers. Early simulations of gel-phase phospholipid (DPPC) bilayers were conducted by Tu *et al.*[28] and Essman *et al.*,[29] who examined areas per lipid, density profiles, and chain configurations for simulations up to 1 ns, which as noted by the authors, is too short to demonstrate convergence.[28] Poger *et al.* reported that the GROMOS53A6 parameter set yielded structural properties characteristic of gel-like phases for DPPC bilayers by measuring area per lipid and tail ordering.[30] Hartkamp *et al.* proceeded to use this force field to report a range of gel-phase bilayer properties for DSPC and mixed DSPC-alcohol systems.[31,32] Recent CHARMM force field updates have been mad eto correct for earlier inconsistencies and more accurately simulate gel-phase structures[33–36] Klauda *et al.* also updated the CHARMM force field, dubbed CHARMM36, to better parametrize lipids and reproduce gel-phase properties, including area per lipid, tail order parameters, and accuracy in tensionless ensembles.[37,38] The CHARMM36 force field has been applied to study a vareity of phospholipid-based bilayers and examine, for example, the influence of cholesterol on bilayer properties[39] and phase transition temperatures of saturated phospholipid bilayers.[40] While the force fields have been improved and computational resources have been expanded, allowing for longer simulation times, to the authors' knowledge, there have been few simulation studies examining the influence of composition on the structure of gel-phase phospholipid bilayers.

Here, we perform molecular dynamics (MD) simulations to examine the structural behavior of multicomponent gel-phase bilayers of 1,2-distearoyl-sn-glycero-3-phosphatidylcholine (DSPC) with various amounts of free fatty acid (FFA) and long chain alcohol (OH) molecules. Two- and three-component mixtures of DSPC, OH, and FFA were examined. The two-

component mixtures consisted of either 33% or 50% (by mol) DSPC, with the remainder either OH or FFA. The three-component mixtures consisted of either 33% or 50% DSPC, with the remainder equimolar OH and FFA. In all mixtures, OH and FFA tail lengths were varied to either 12, 16, or 24 carbons.

3.2   Methods

All of the bilayer systems studied were initialized using the mBuild software package.[41] Each bilayer was constructed using two leaflets consisting of leaflets arranged in an 8 x 8 square lattice. Lattice spacing was chosen to be ~20% larger than the final area per lipid based on earlier work.[31,32] To assess finite system size effects, larger simulations using 10 x 10 leaflets for select compositions were also performed and good agreement with the 8 x 8 leaflets was obtained. Lipids were tilted randomly between 5 and 25° with respect to the bilayer normal and randomly placed along leaflets. Lipids were also randomly spun around their tail vectors to avoid artificial alignment as found in other work.[42] Bilayers were solvated with 20 water molecules per lipid for a total of 2560 water molecules. Energy minimization was performed using steepest descent to remove any unfavorable overlaps between molecules in the initial configuration followed by 100 ps of NVT equilibration and 500 ps of NPT equilibration. Random Walk MD (RWMD)[43] was then performed for a total of 190 ns to relax the bilayer configurations away from any initial configuration bias. Briefly, RWMD involves a random walk through temperature spacae over the course of a MD simulation by randomly swapping simulation temperatures with adjacent temperatures.[43] For the first 30 ns, temperature windows were spaced 10 K between 305 and 455 K. For the remainder of the RWMD, the temperature ceiling (initially 455 K) was reduced by 10 K every 10 ns to allow the system to gradually settle into a stable, gel-phase configuration. 100 ns of NPT sampling was then performed at 305 K and 1 bar, with the last 20 ns used for analysis. Over the 100 ns of NPT sampling, systems were determined to be well-equilibrated based on agreement between leaflet angle distributions, convergence of
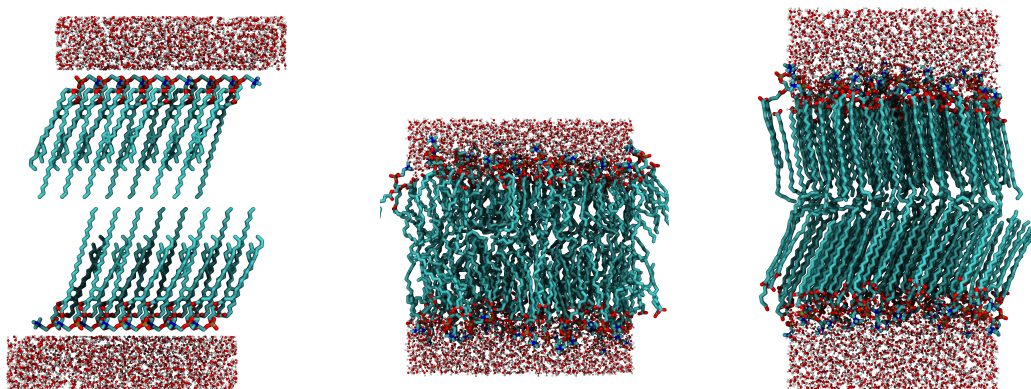
Figure 3.1: 50% DSPC, FFA24 configurations through equilibration protocol. mBuild-generated structure (left). Sample configuration from RWMD (middle). Relaxed, gel-phase structure (right)

measured values of time, and agreement of measured values across simulations of the same composition with different initial configurations.

All simulations were performed using the GROMACS 2018 MD simulation engine.[44–49] DSPC, alcohol (OH), and fatty acid (FFA) molecules were parametrized according to the CHARMM-GUI in accordance with the CHARMM36 all-atom force field.[37,50] Water was modeled using TIP3P and constrained using the SETTLE algorithm.[51–53] All other bonds containing hydrogen were constrained using the LINCS algorithm.[54] Electrostatics were computed using the particle mesh Ewald (PME) method with a real-space cutoff of 1.2 nm and Fourier spacing of 0.16 nm.[55] Force-switching functions were used for van der Waals interactions between 10 and 12 Å.[50] Temperature was held at 305 K using a Nosé-Hoover thermostat with a 1.0 ps time constant.[50,56,57] Pressure was held semi-isotropically at 1 bar (XY and Z directions coupled separately) using a Parrinello-Rahman barostat with a 2.0 ps time constant.[58] Compressibility was held at 4.5 x 10^{-5} bar^{-1}. A 2 fs timestep was used. Snapshots throughout the equilibration process are shown in Figure 3.1.

3.2.1 Analysis

Atomic positions and simulation box dimensions were used to compute the area per lipid (APL), area per tail (APT), average tilt angle, component offset distances, bilayer height, and interdigitation (Idig). The APL was computed by dividing the cross-sectional area of the simulation box by the number of lipids in the leaflet. The tilt angle was taken as the average angle between the long axis of a molecule's tail and the bilayer normal, with the long axis defined as the eigenvector corresponding to the minimum eigenvalue of the inertia tensor.[59] The APT was computed by dividing the APL by the average number of tails per lipid and multiplying by the cosine of the tilt angle. Component offset distances were determined by comparing the average depth (Z-coordinate) of the DSPC phosphate group's center of mass and the component's head group center of mass. For alcohol (OH) groups, the head group was taken as the hydroxyl group. For fatty acids (FFA), the head group was taken as the carboxylic acid group. For convention, a component with a larger offset is buried deeper into the bilayer. The bilayer height was computed as the average offset distance of DSPC phosphate groups between leaflets. Interdigitation (Idig) was calculated using the overlap between leaflet density profiles.[60]

$$I_{dig} = \int_{-\infty}^{\infty} \frac{4\rho_T(z)\rho_B(z)}{(\rho_T(z) + \rho_B(z))^2} dz \qquad (3.1)$$

where the subscripts "T" and "B" indicate top and bottom leaflets, respectively. The S2 order parameter was computed as the largest eigenvalue of the nematic tensor, derived from the lipid tails in each leaflet.[43,61]

Block-averaging was performed with block sizes of 5 ns. Error bars are reported 1 standard error from the block-averaging procedure. For a given composition, multiple simulations were performed with varying initial APL and initial tilt angle. Simulation analyses were conducted using the MDTraj and MDAnalysis Python libraries.[62–64] Analysis was aided by software packages within the scientific Python ecosystem: SciPy,[65] NumPy,[66]

Pandas,[67] and Matplotlib.[68] Usage of mBuild in addition to other well-tested, open-source tools within the Python ecosystem help ensure TRUE simulations – transferable, reproducible, usable, and extensible.[69–71]

3.3   Results and Discussion

In order to validate our simulation methodologies, a single-component DSPC bilayer was first studied. Results for the pure DSPC system are presented Table 3.1 and are found to be consistent with both experimental and prior simulation findings, validating our use of RWMD as an equilibration protocol in gel-phase DSPC systems.[14,32,40]

Table 3.1: Structural data gathered for a pure DSPC bilayer.

APL (Å^2)	Tilt Angle (°)	APT (Å^2)	Height (Å)	Idig (Å)	S2
50.4 (0.1)	35.9 (0.2)	20.3 (0.03)	46.6 (0.1)	3.06 (0.04)	0.964 (0.001)

The results from simulations of two-component mixtures are presented below. While we will discuss each bilayer property in turn, in general we find that bilayer properties are largely dependent on DSPC fraction and tail length, but the slight head group differences between FFA and OH can cause modest differences in structure.

3.3.1   Component Offset Distances

For two-component mixtures, a schematic illustrating the offset of the secondary component (FFA or OH) is shown in Figure 3.2. In multi-component mixtures, we observe different components are found at different depths within the bilayer, presumably to maximize van der Waals attractions from the tails and minimize steric repulsions from the head groups. Component localizations were also identified in simulations of fluorinated alcohols in DOPC bilayers, where the increased steric repulsiosn due to the large fluorinated head groups compared to their nonfluorinated counterparts drove the fluorinated alcohols deeper

31

inside the bilayer.[72] The component offset observed herein appears strongly dictated by the DSPC fraction and the tail length (Figure 3.3). Due to the large steric repulsions from DSPC head groups, the secondary components are pushed deeper to the center of the bilayer. To a lesser degree, the FFA components exhibit slightly more steric repulsion than OH components, leading to greater FFA offset than OH offset. In order to maintain tail overlap, longer chains are found closer to the bilayer-water interface. Interestingly, the FFA and OH offsets at 33% DSPC are roughly the same – this observation could be due to the strong presence of 24-carbon tails compensating for any head group differences. By increasing the order in gel-phase systems compared to fluid-phase systems, components may be more energetically favored to displace themselves deeper into the bilayer to reduce steric repulsions and increase van der Waals attractions.
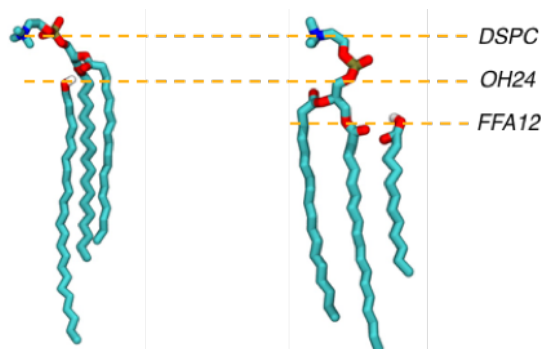
Figure 3.2: Visualization of component offsets. The longer lignoceryl (OH24, left) component lies closer to the DSPC head groups compared to the shorter dodecanoic acid (FFA12, right) component.
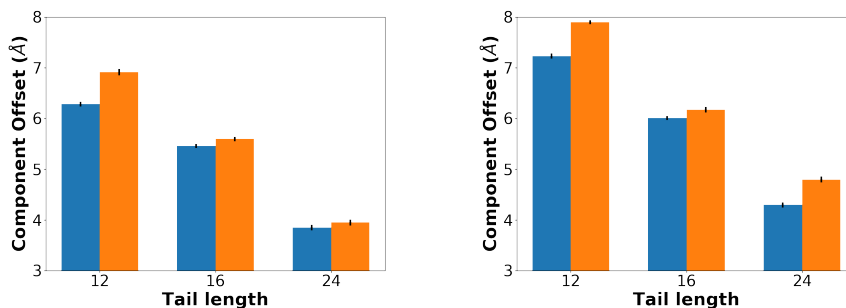
Figure 3.3: Secondary component offset comparisons for two-component mixtures containing 33% DSPC(left) or 50% DSPC (right). Fatty acid systems shown by orange bars and alcohol by blue.

Similar to two-component systems, the three-component systems exhibit greater offset with larger DSPC fractions providing greater steric repulsion (Figure 3.4). Additionally, shorter-tailed components have larger offsets than longer-tailed components. Comparing corresponding two- and three-component systems with symmetric tails (e.g., DSPC-OH12 or DSPC-FFA12 and DSPC-OH12-FFA12), the component offsets are roughly the same. Only slight differences, that can be attributed to head group substitutions, are observed. When looking at three-component systems with asymmetric tails (e.g., DSPC-OH12-FFA24), component offsets are found to be different than the respective binary (e.g., DSPC-OH12 and DSPC-FFA24). By increasing the variety of tail lengths present in the three-component bilayers, the lipids can offset differently to maximize tail overlap as compared to the two-component system. For example, looking at 12- and 16-carbon tails, increasing the tail length of one component will increase the offset of the other. The 33% DSPC, OH12-FFA12 system demonstrates a particular offset combination for OH12 and FFA12; the 33% DSPC, OH16-FFA12 system demonstrates an increased FFA12 offset while the 33% DSPC, OH12-FFA16 system demonstrates an increased OH12 offset. By lengthening one component, the other component can descend deeper into the bilayer. 24-carbon tails, however, do not create the same space for molecules to descend due to the loss of nematic order toward the middle, interdigitated region of the bilayer (Figure 3.5).

The loss in nematic order can be attributed to the noticeably longer tails in the 24-carbon components compared to the tails of other components.

When looking at the effect of head group chemistry in systems of three-component systems and asymmetric tails, offsets are not consistent. For example, when comparing DSPC-OH16-FFA12 and DSPC-OH12-FFA16 systems, the FFA12 does not share the same offset as the OH12 and the OH16 group does not share the same offset as the FFA16 group. This observation reinforces the notion that different head groups can slightly adjust their offset, although tail length has a more noticeable effect. Furthermore, this observation has consequences for structural properties as discussed below.
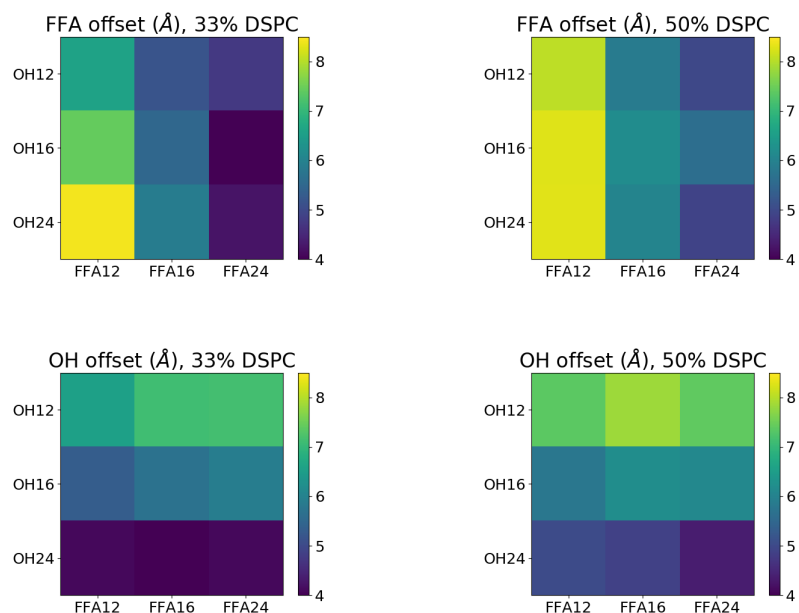
Figure 3.4: Offset comparisons for three-component mixtures containing 33% DSPC (left) or 50% DSPC (right). Fatty acid component offsets (top), alcohol component offsets (bottom).
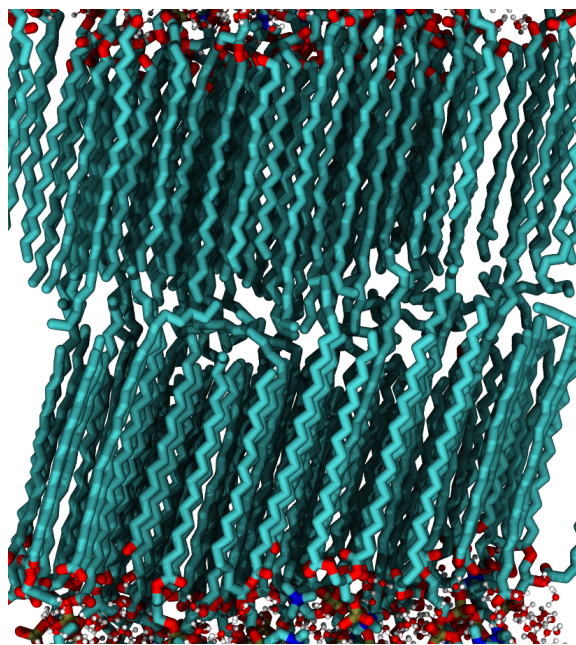
Figure 3.5: Simulation snapshot of 33% DSPC, OH16-FFA24, demonstrating how long-tailed components lose order in the middle of the bilayer.

3.3.2 Area Per Tail (APT)

Tail-length mismatch in addition to offset differences can help elucidate the role of composition on lipid packing. Results for the APT are shown in Figure 3.6. For OH systems, the lipid tails appear to reach the densest packing (lowest APT) when the tails are equal in length. This result suggests that the van der Waals attractions from the tail groups help the tails pack more tightly. However, unequal-length tails mitigate their ability to align and support other tails; longer tails cannot overlap as easily with shorter tails and result in worse alignment and packing. Using an analysis of variance (ANOVA) test to evaluate the APT variance between all binary and ternary systems, an F-value of 4.52 was obtained with a p-value of 4.0e-7, suggesting these data are statistically significant.

For FFA systems, it is important to recognize the enlarged cross-sectional area from the FFA head group compared to the OH group, which introduces disorder and makes lipid packing more difficult. In the 33% DSPC-67%FFA systems, increasing the FFA tail length appears to strengthen the van der Waals attractions, overcoming the relatively larger head

groups compared to OH head groups and increasing packing. In the 50% DSPC-50% FFA systems, increasing the number of tails relative to head groups compared to the 33% DSPC-67% FFA systems, is found to strengthen the van der Waals attractions and help overcome the enlarged head groups. As a result, equal-length tails appear to pack the most densely (similar to the OH case).

Hartkamp *et al.* presented different APT-OH tail length trends with DSPC-OH mixtures using the GROMOS53A6 force field.[31] Quantitatively, the values differ by less than 1 $Å^2$. Qualitatively, however, some of the GROMOS53A6 and CHARMM36 trends differ. In the 50%-50% DSPC-OH systems, the GROMOS trends indicate an APT minimum with the shortest tail lengths (OH12), whereas the CHARMM trends indicate an APT minimum with OH16, where the OH and DSPC chain lengths are most equal. In the 33%-67% systems, the GROMOS trends indicate DSPC-OH24 has a smaller APT than DSPC-OH16, while the CHARMM trends indicate the opposite. The small quantitative differences between force fields that result in different qualitative trends may be due to different force field parametrizations.

A similar observation was found by Moore *et al.*[43] when computationally comparing ceramides with different fatty acid tail lengths. When increasing chain length, very slight APT fluctuations were found, but much larger APT variations were observed when altering the cholesterol or saturated FFA content – substituting ceramide with cholesterol or FFA and substituting DSPC with OH or FFA have larger influences on APT compared to chain length.[43] We note that these packing trends for gel-phase systems appear different from trends within fluid-phase systems, where 4- to 7-carbon OH components tended to increase membrane volume because short component could not reach into the hydrophobic tail region and 8- to 12-carbon OH components tended to occupy the free volume in the tail region and lead to denser packing.[22] This difference can be attributed to the already-dense packing of the gel-phase systems versus the disordered, loose-packing in fluid-phase systems.
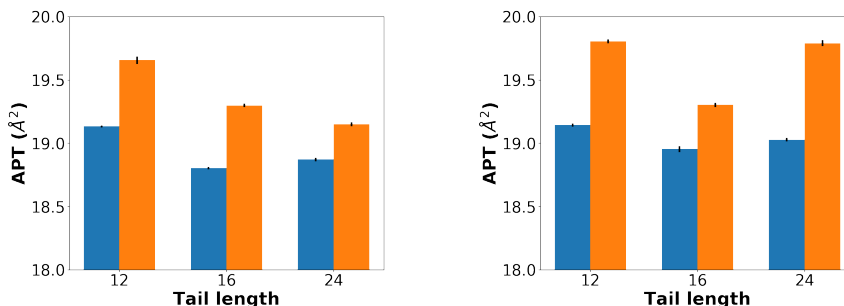
Figure 3.6: APT comparisons for two-component mixtures containing 33% DSPC (left) or 50% DSPC (right). Systems composed of FFA (orange) and OH (blue).

We also note the experimental agreement with Hishida *et al.*, who observed tail-tail distances decrease with the addition of n-alkanes by filling in the gaps generated from large head groups, also resulting in a more rigid structure.[20] For a pure DSPC bilayer, our simulated APT is 20.3 $Å^2$. Upon mixing with singled-tailed components, the APT drops below 20 $Å^2$. The simulation trends agree with the experimental trends as the addition of single-tailed components allows for closer tail spacing; however, the tail-length dependence found is not the same as that found by Hishida *et al.*, who found that interstitial distances between alkyl chains decreased monotonically with alkane chain length. This could be due to differences in the head group chemistry or choice of chain lengths (Hishida *et al.* used 8-14 carbons; this study uses 12-14 carbons).[19,20] Additionally, the simulated APT values are in agreement with the area per chain values of 21.4 $Å^2$ reported by Seddon *et al.* from X-ray studies of DSPC-FFA bilayers.[27]

3.3.3   Intra-bilayer Hydrogen Bonding

Thus far, the simulations show that altering bilayer composition can result in different depth localizations (offsets) and tail packing (APT) in the binary and ternary systems studied. To examine any relationships with hydrogen bonding networks that could arise from offset or lipid packing effects, intra-bilayer hydrogen bonding was measured. This property counts the number of hydrogen bonds between bilayer molecules, excluding water

hydrogen bonding (Figure 3.7). As can be seen from the results in Figure 3.7, 33% DSPC systems appear to form a larger number of hydrogen bonds compared to 50% DSPC systems, likely due to the increased number of hydrogen bond donors (DSPC molecules have no hydrogen bond donors, only acceptors). Looking at head group chemistry effects, OH systems are found to form a larger number of hydrogen bonds compared to FFA systems, possibly due to the increased steric repulsion and disorder that mitigates the formation of hydrogen bonds in FFA systems. Similarly, longer components tend to form more hydrogen bonds compared to shorter components, which can be related to the offset and closer proximity of C24 components to DSPC molecules compared to shorter components. Using an ANOVA test across the various compositions studied, an F-statistic of 17.2 is obtained with a p-value of 5.6e-8, suggesting these properties are statistically significant.
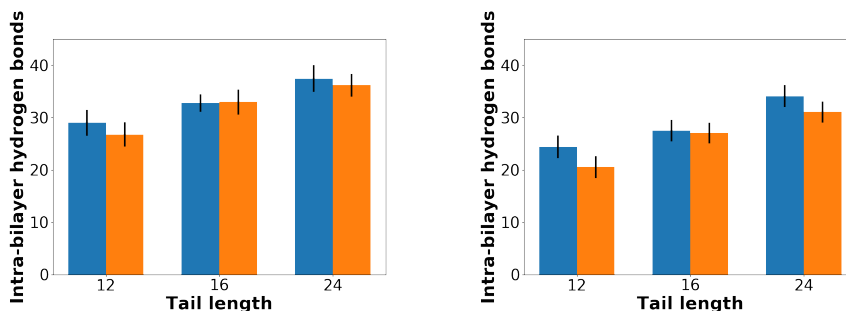
Figure 3.7: Intra-bilayer hydrogen bonding numbers for two-component mixtures containing 33% DSPC (left) or 50% DSPC (right). Systems are composed of FFA (orange) and OH (blue).

3.3.4 Interfacial Water Relaxation

Since bilayer composition naturally appears to have an influence on the bilayer hydrogen bonding network, interfacial water dynamics may also be affected. Various groups have recognized the complex interactions between water and head groups in phospholipid membranes, noting that water has an influence on properties including surface pressure, activity, and hydration behavior.[13,14,16,17,73–78] The dipole relaxation times for the 33% DSPC systems generally appear longer than those for 50% DSPC systems. In the Appendix, ob-

38

serving that 33% DSPC systems have a smaller APL (tighter head group packing), the more densely-packed hydrophilic head groups can develop more sustained water contacts than the less densely-packed 50% DSPC systems. Within the 33% DSPC systems, longer tails appear to increase the dipole relaxation times; as longer-tailed components move closer to the bilayer-water interface, the components can form more contacts with the solvent, slowing down their overall dynamics. However, within the 50% DSPC systems, the water dynamics appear dominated by the increased number of phosphocholine head groups, masking the influence of the secondary component. Similar, Hartkamp *et al.* reported longer-lasting lipid-water hydrogen bonds, and thus slower interfacial water dynamics, as chain length increased.[79]

Our findings (Figure 3.8) preliminarily appear to contradict those of Baryiames *et al.*, who studied heterogeneous reverse micelles and the role of composition on hydrogen bonding and interfacial water dynamics.[80] Using reverse micelles composed of sorbitan (a nonionic detergent) with FFA16-18 substitutions for hydroxyl functional groups, they observed water interfacial hydrogen bond dynamics to slow in heterogeneous (more FFA16-18 substitutions) systems compared to homogeneous systems (no FFA substitutions). This result was largely due to the ability of water to penetrate more deeply into the micelle. They observed water penetration to be influenced by composition heterogeneity, where heterogeneous systems packed poorly compared to homogeneous systems, and this poor packing created space for water penetration and slower dynamics. In contrast, our systems demonstrate greater packing when heterogeneous; the ability for the lipids to offset their position within the bilayer creates space for greater water penetration, resulting in slower water dynamics compared to pure DSPC. However, although shorter components with deeper offsets in our bilayers can yield greater water penetration and possibly slower water dynamics, the reduction in solvent-head group contact accelerates water dynamics. Rationalizing our results with Baryiames' findings, the 24-carbon components and their offsets provide a balance of solvent-head group contact and water penetration to result in slower

water dynamics compared to shorter-length components.

Generally, our data suggest that OH components slow down interfacial water more than FFA components, possibly due to less offset promoting more solvent contact with DSPC head groups. Using an ANOVA test across the compositions studied, an F-statistic of 3.48 was obtained with a p-value of 2.2e-5, suggesting the properties are statistically significant.
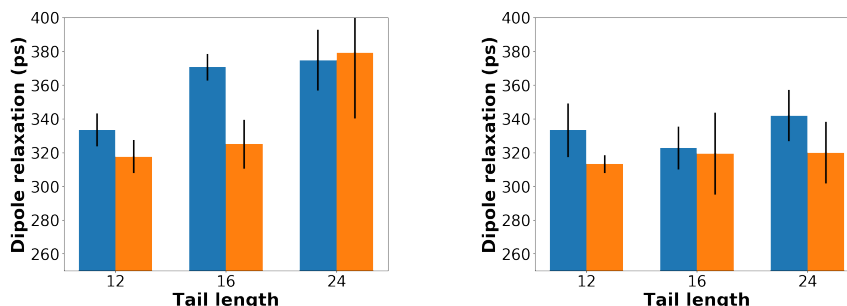
Figure 3.8: Water dipole relaxation times near the bilayer-water interface for two-component mixtures containing 33% DSPC (left) or 50% DSPC (right). Systems are composed of FFA (orange) and OH (blue). For reference, the corresponding pure DSPC value is about 200 ps.

3.3.5 Area Per Lipid (APL), Height, Interdigitation (Idig), S2, and Tilt

The Appendix A presents additional structural information for the various mixed bilayer systems examined. In general, we find that the APL is dependent on the DSPC fraction. Given the size of the DSPC head group compared to the other lipids, this is not surprising and consistent with results found in earlier work.[31] FFA molecules tend to increase the APL more than the OH molecules, similarly due to slightly increased steric repulsions. At 50% DSPC, the APL tends to increase with tail length, which can be attributed to the reduced component offset and closer proximity between different components (see offset discussion from Section 3.3.1). For example, 24-carbon length tails move closer to the water-bilayer interface, introduce greater steric repulsions to the DSPC head groups, and cause the head groups to laterally spread apart. We note similar results with Hishida *et al.*, who found that alkanes can increase the head-head distance in their 70 mol% DMPC bilayers with 30

mol% alkane (8- to 14- carbon tails).[20] At 33% DSPC, the DSPC remains fairly constant, which could be due to the overall head group size reduction by substituting DSPC with FFA or OH.

Tilt angle appears dependent on both DSPC fraction and tail length. While larger head groups induce greater steric repulsion that pushes the lipids apart and increases APL, tilting provides the lipid tails with a mechanism to maximize van der Waals interactions while reducing steric repulsions. Furthermore, longer tails enhance the strength of the van der Waals interaction, resulting in a larger tilt angle, which again is similar to that observed by Hartkamp *et al.*[31] Additionally, the results are consistent with the work of Seddon *et al.* who reported that the addition of FFA reduces the tilt of gel-phase bilayers.[27,40] It should be noted that our 33% DSPC, 67% FFA mixtures not only demonstrate a low tilt angle, but also a low APL. This result could indicate an already-favorable distribution of lipids along the bilayer normal without needing to tilt or laterally spread out, compared to other DSPC-FFA mixtures that require tilting to obtain a favorable configuration.

Bilayer height generally increases with the tail length as longer tails naturally increase the thickness of each leaflet. Similar trends were found by Seddon *et al.*[27] Bilayer height are, however, also affected by tilt angles and interdigitation. Compared to FFA components, OH components generally result in taller bilayers due to the lower tilt angles. At 33% DSPC, the 12- and 24-carbon FFA and OH bilayers display the same height due to the interdigitation and tilt angle properties balancing each other out. Interdigitation measures the amount of leaflet-leaflet overlap, with greater interdigitation values indicating higher leaflet-leaflet overlap. The amount of interdigitation is found to depend on the amount of tail-length asymmetry, similar to earlier work.[31] DSPC tails are 18-carbons long, which effectively reach to similar depths as OH16 and FFA16 when considering component offset. Due to this similarity in tail length, there is little room for opposing leaflets to interdigitate. By shortening or lengthening one component, the resulting tail-length asymmetry creates space for the opposing leaflet. A similar observation was found by Aagaard *et al.*, who

reported a "mismatch" effect that had influence on molar volume.[22]

The three-component systems examined in this study demonstrate many of the same trends as the two-component systems, namely dependence on DSPC fraction and tail length with some modest differences when mixing OH and FFA head groups. By increasing the variety of tail lengths in the system, components are able to displace themselves depth-wise and provide an additional mechanism for generating stable, tightly packed configurations. The DSPC fractions studied are the same as those examined in the two-component systems (33% and 50%), but the non-DSPC component in the two-component system can be viewed has having been partially substituted with a third component, further altering tail length or head group chemistry. Results for three-component systems follow similar trends as two-component systems, and can be found in the Appendix A.

3.4 Conclusion

Two- and three-component gel-phase, lipid bilayers were studied, whose compositions included DSPC and combinations of OH and FFA with 12-, 16-, and 24-carbon tails. We observe that head group repulsion and tail-length asymmetry drive shorter components deeper within the bilayer. These component offsets influence tail alignment and tail packing (APT). Furthermore, the component offsets and APT properties affect intra-bilayer hydrogen bonding; tighter-packed tails and greater intra-bilayer hydrogen bonding appear correlated. As a result of tail packing and intra-bilayer hydrogen bond networks, the interfacial solvent dynamics are impacted, as observed by the water dipole relaxation times.

Bilayer structure is largely dictated by the steric repulsions from head groups and van der Waals attractions from tails. Larger head groups create greater steric repulsion, and longer tails provide greater van der Waals attraction. OH and FFA components possess chemically similar tails but slightly different head groups, which has small effects on resultant bilayer properties. Shorter-tailed components are found deeper within the bilayer, which can help mitigate the steric repulsions at the bilayer-water interface, but reduces the

amount of intra-bilayer hydrogen bonding. APL and tilt angle are most largely affected by DSPC fraction, although secondary and tertiary components can introduce offsets that can slightly modify the steric repulsions. Area per tail and nematic order depends on head group size and tail length, but OH components and 16-carbon tails generally exhibit the lowest APT and highest S2. Interdigitation is most affected by tail length asymmetry. Dipole relaxation times of interfacial water appear dependent on the area per lipid due to the ability of hydrophilic head groups to form contacts with water. Various published results for fluid-phase and gel-phase systems help corroborate the findings here.

Overall, these results shed light on mechanisms by which lipids can pack differently in gel-phase bilayers. By understanding how the composition of head groups and tail lengths affects the balance between steric repulsion and van der Waals attraction, formulations can be designed with particular structures in mind. Further, this work may shed light on how composition can be used to tune barrier properties of gel-phase membranes.

3.5   Bibliography

[1] A. Tardieu, Vittorio Luzzati, and F. C. Reman. "Structure and polymorphism of the hydrocarbon chains of lipids: A study of lecithin-water phases". In: *Journal of Molecular Biology* 75.4 (1973), pp. 711–733.

[2] Gonneke S K Pilgram et al. "Aberrant Lipid Organization in Stratum Corneum of Patients with Atopic Deramtitis and Lamellar Ichthyosis". In: *Journal of Investigative Dermatology* 117.3 (2001), pp. 710–717.

[3] J. Van Smeden et al. "The important role of stratum corneum lipids for the cutaneous barrier function". In: *Biochimica et Biophysica Acta - Molecular and Cell Biology of Lipids* 1841.3 (2014), pp. 295–313.

[4] Julia Caussin, Gert S. Gooris, and Joke A. Bouwstra. "FTIR studies show lipophilic moisturizers to interact with stratum corneum lipids, rendering the more densely packed". In: *Biochimica et Biophysica Acta - Biomembranes* 1778.6 (2008), pp. 1517–1524.

[5] D Groen et al. "Is an orthorhombic lateral packing and a proper lamellar organization important for the skin barrier function?" In: *Biochimica et Biophysica Acta - Biomembranes* 1808.6 (2011), pp. 1529–1537.

[6] J. Caussin et al. "Interaction of lipophilic moisturizers on stratum corneum lipid domains in vitro and in vivo". In: *Skin Pharmacology and Physiology* 20.4 (2007), pp. 175–186.

[7] G. Pennick et al. "The effect of an amphiphilic self-assembled lipid lamellar phase on the relief of dry skin". In: *International Journal of Cosmetic Science* 34.6 (2012), pp. 567–574.

[8] G Pennick et al. "Superior effect of isostearyl isostearate on improvement in stratum corneum water permeability barrier function as examined by the plastic occlusion stress test". In: *International Journal of Cosmetic Science* 32.4 (2010), pp. 304–312.

[9] Robert S. Summers et al. "The effect of lipids, with and without humectant, on skin xerosis". In: *Journal of the Society of Cosmetic Chemists* 47.February (1996), pp. 27–39.

[10] P. A. Bulsara et al. "The rational design of biomimetic skin barrier lipid formulations using biophysical methods". In: *International Journal of Cosmetic Science* 39.2 (2017), pp. 206–216.

[11] L J Lis et al. "Interactions between neutral phospholipid bilayer membranes." In: *Biophysical journal* 37.3 (1982), pp. 657–65.

[12] R.P. Rand and V.A. Parsegian. "Hydration forces between phospholipid bilayers". In: *BBA - Reviews on Biomembranes* 988.3 (1989), pp. 351–376.

[13] G. S. Smith et al. "X-ray structural studies of freely suspended ordered hydrated DMPC multimembrane films". In: *The Journal of Chemical Physics* 92.7 (1990), pp. 4519–4529.

[14] W. J. Sun et al. "Structure of gel phase saturated lecithin bilayers: temperature and chain length dependence." In: *Biophysical journal* 71.2 (1996), pp. 885–891.

[15] S. Tristram-Nagle et al. "Measurement of chain tilt angle in fully hydrated bilayers of gel phase lecithins". In: *Biophysical Journal* 64.4 (1993), pp. 1097–1109.

[16] Stephanie Tristram-Nagle et al. "Structure of gel phase DMPC determined by x-ray diffraction". In: *Biophysical Journal* 83.6 (2002), pp. 3324–3335.

[17] M. C. Wiener, R. M. Suter, and J. F. Nagle. "Structure of the fully hydrated gel phase of dipalmitoylphosphatidylcholine". In: *Biophysical Journal* 55.2 (1989), pp. 315–325.

[18] K. Akabori and J. F. Nagle. "Structure of the DMPC lipid bilayer ripple phase". In: *Soft Matter* 11.5 (2015), pp. 918–926. arXiv: 15334406.

[19] Mafumi Hishida et al. "Phase separation of a ternary lipid vesicle including <i>n</i> -alkane: Rugged vesicle and bilayer flakes formed by separation between highly rigid and flexible domains". In: *The Journal of Chemical Physics* 150.6 (2019), p. 064904.

[20] Mafumi Hishida et al. "Effect of n-alkanes on lipid bilayers depending on head-groups". In: *Chemistry and Physics of Lipids* 188 (2015), pp. 61–67.

[21] Mafumi Hishida et al. "Communication: Rigidification of a lipid bilayer by an incorporated n -alkane". In: *Journal of Chemical Physics* 144.4 (2016).

[22] Thomas H. Aagaard, Mette N. Kristensen, and Peter Westh. "Packing properties of 1-alkanols and alkanes in a phospholipid membrane". In: *Biophysical Chemistry* 119.1 (2006), pp. 61–68.

[23] Helgi I. Ingólfsson and Olaf S. Andersen. "Alcohol's effects on lipid bilayer properties". In: *Biophysical Journal* 101.4 (2011), pp. 847–855.

[24] R C Lyon et al. "A relationship between alcohol intoxication and the disordering of brain membranes by a series of short-chain alcohols." In: *The Journal of pharmacology and experimental therapeutics* 218.3 (1981), pp. 669–675.

[25] Hung V. Ly and Marjorie L. Longo. "The influence of short-chain alcohols on interfacial tension, mechanical properties, area/molecule, and permeability of fluid lipid bilayers". In: *Biophysical Journal* 87.2 (2004), pp. 1013–1033.

[26] Emma Falck et al. "Lessons of Slicing Membranes: Interplay of Packing, Free Area, and Lateral Diffusion in Phospholipid/Cholesterol Bilayers". In: *Biophysical Journal* 87.2 (2004), pp. 1076–1091. arXiv: 0402290 [cond-mat].

[27] John M Seddon et al. "Phosphatidylcholinefatty acid membranes: effects of head-group hydration on the phase behaviour and structural parameters of the gel and inverse hexagonal (HII) phases". In: *Biochimica et Biophysica Acta (BBA) - Biomembranes* 1327.1 (1997), pp. 131–147.

[28] K Tu et al. "Molecular dynamics investigation of the structure of a fully hydrated gel-phase dipalmitoylphosphatidylcholine bilayer." In: *Biophysical journal* 70.2 (1996), pp. 595–608.

[29] Ulrich Essmann, Lalith Perera, and Max L. Berkowitz. "The Origin of the Hydration Interaction of Lipid Bilayers from MD Simulation of Dipalmitoylphosphatidylcholine Membranes in Gel and Liquid Crystalline Phases". In: *Langmuir* 11.24 (1995), pp. 4519–4531.

[30] David Poger, Wilfred F. van Gunsteren, and Alan E. Mark. "A New Force Field for Simulating Phosphatidylcholine Bilayers". In: *Journal of computational chemistry* 31.6 (2009), pp. 1117–1125. arXiv: NIHMS150003.

[31] Remco Hartkamp et al. "Structural Properties of Phospholipid-based Bilayers with Long- Chain Alcohol Molecules in the Gel Phase". In: *Journal of Physical Chemistry B* 120.50 (2016), pp. 12863–12871.

[32] Remco Hartkamp et al. "Investigating the Structure of Multicomponent Gel-Phase Lipid Bilayers". In: *Biophysical Journal* 111.4 (2016), pp. 813–823.

[33] Richard M. Venable, Bernard R. Brooks, and Richard W. Pastor. "Molecular dynamics simulations of gel (LβI) phase lipid bilayers in constant pressure and constant surface area ensembles". In: *The Journal of Chemical Physics* 112.10 (2002), pp. 4822–4832.

[34] Scott E. Feller and Richard W. Pastor. "Constant surface tension simulations of lipid bilayers: The sensitivity of surface areas and compressibilities". In: *Journal of Chemical Physics* 111.3 (1999), pp. 1281–1287.

[35] Jeffery B. Klauda et al. "Simulation-based methods for interpreting x-ray data from lipid bilayers". In: *Biophysical Journal* 90.8 (2006), pp. 2796–2807.

[36] Alison N. Leonard et al. "Developing and Testing of Lipid Force Fields with Applications to Modeling Cellular Membranes". In: *Chemical Reviews* 119.9 (2019), pp. 6227–6269.

[37] Jeffery B Klauda et al. "Update of the CHARMM all-atom additive force field for lipids: validation on six lipid types". In: *The Journal of Physical Chemistry B* 114.23 (2010), pp. 7830–7843.

[38] R. W. Pastor and A. D. MacKerell. "Development of the CHARMM force field for lipids". In: *Journal of Physical Chemistry Letters* 2.13 (2011), pp. 1526–1532.

[39] Christopher T Boughter et al. "Influence of Cholesterol on Phospholipid Bilayer Structure and Dynamics". In: *The Journal of Physical Chemistry B* (2016), acs.jpcb.6b08574.

[40] Pouyan Khakbaz and Jeffery B. Klauda. "Investigation of phase transitions of saturated phosphocholine lipid bilayers via molecular dynamics simulations". In: *Biochimica et Biophysica Acta - Biomembranes* 1860.April (2018), pp. 1489–1501.

[41] Christoph Klein et al. "A Hierarchical, Component Based Approach to Screening Properties of Soft Matter". In: *Foundations of Molecular Modeling and Simulation: Select Papers from FOMMS 2015*. Ed. by Randall Q Snurr, Claire S Adjiman, and David A Kofke. Singapore: Springer Singapore, 2016, pp. 79–92.

[42] Karthik Uppulury, Patrick S. Coppock, and James T. Kindt. "Molecular Simulation of the DPPE Lipid Bilayer Gel Phase: Coupling between Molecular Packing Order and Tail Tilt Angle". In: *Journal of Physical Chemistry B* 119.28 (2015), pp. 8725–8733.

[43] Timothy C. Moore et al. "Effect of Ceramide Tail Length on the Structure of Model Stratum Corneum Lipid Bilayers". In: *Biophysical Journal* 114.1 (2018), pp. 113–125.

[44] Erik Lindahl, Berk Hess, and David van der Spoel. "GROMACS 3.0: a package for molecular simulation and trajectory analysis". In: *Molecular Modeling Annual* 7.8 (2001), pp. 306–317.

[45] David Van Der Spoel et al. "GROMACS: Fast, flexible, and free". In: *Journal of Computational Chemistry* 26.16 (2005), pp. 1701–1718.

[46] Berk Hess et al. "GROMACS 4: Algorithms for Highly Efficient, Load-Balanced, and Scalable Molecular Simulation". In: *Journal of Chemical Theory and Computation* 4.3 (2008), pp. 435–447.

[47] Sander Pronk et al. "GROMACS 4.5: a high-throughput and highly parallel open source molecular simulation toolkit". In: *Bioinformatics* 29.7 (2013), p. 845.

[48] Mark James Abraham et al. "GROMACS: High performance molecular simulations through multi-level parallelism from laptops to supercomputers". In: *SoftwareX* 1-2 (2015), pp. 19–25.

[49] Szilárd Páll et al. "Tackling Exascale Software Challenges in Molecular Dynamics Simulations with GROMACS". In: *Solving Software Challenges for Exascale: International Conference on Exascale Applications and Software, EASC 2014, Stockholm, Sweden, April 2-3, 2014, Revised Selected Papers*. Ed. by Stefano Markidis and Erwin Laure. Cham: Springer International Publishing, 2015, pp. 3–27.

[50] Sunhwan; Jo et al. "CHARMM-GUI: A Web-Based Graphical User Interface for CHARMM". In: *Journal of computational chemistry* 29 (2008), pp. 1859–1865. arXiv: NIHMS150003.

[51] William L. Jorgensen et al. "Comparison of simple potential functions for simulating liquid water". In: *The Journal of Chemical Physics* 79.2 (1983), pp. 926–935. arXiv: arXiv:1011.1669v3.

[52]   Shuichi Miyamoto and Peter A Kollman. "Settle: An analytical version of the SHAKE and RATTLE algorithm for rigid water models". In: *Journal of Computational Chemistry* 13.8 (1992), pp. 952–962.

[53]   A. D. MacKerell et al. "All-Atom Empirical Potential for Molecular Modeling and Dynamics Studies of Proteins". In: *The Journal of Physical Chemistry B* 102.18 (1998), pp. 3586–3616. arXiv: NIHMS150003.

[54]   Berk Hess. "P-LINCS: A Parallel Linear Constraint Solver for Molecular Simulation". In: *Journal of Chemical Theory and Computation* 4.1 (2008), pp. 116–122.

[55]   Ulrich Essmann et al. "A smooth particle mesh Ewald method". In: *The Journal of Chemical Physics* 103 (1995), pp. 8577–8593.

[56]   Shuichi Nosé. "A unified formulation of the constant temperature molecular dynamics methods". In: *The Journal of Chemical Physics* 81.1 (1984), pp. 511–519. arXiv: 9807099 [cond-mat].

[57]   William G Hoover. "Canonical dynamics: Equilibrium phase-space distributions". In: *Phys. Rev. A* 31.3 (1985), pp. 1695–1697.

[58]   Michele Parrinello and Aneesur Rahman. "Polymorphic transitions in single crystals: A new molecular dynamics method". In: *Journal of Applied physics* 52.12 (1981), pp. 7182–7190.

[59]   S Mabrey and J M Sturtevant. "Investigation of Phase Transitions of Lipids and Lipid Mixtures by High Sensitivity Differential Scanning Calorimetry". In: *Proceedings of the National Academy of Sciences* 73.11 (1976), pp. 3862–3866.

[60]   M R Wilson. "Determination of Order Parameters in Realistic Atom-Based Models of Liquid Crystal Systems". In: *Journal of Molecular Liquids* 68.1 (1996), pp. 23–31.

[61] Shan Guo et al. "Simulation study of the structure and phase behavior of ceramide bilayers and the role of lipid head group chemistry." In: *Journal of chemical theory and computation* 9.11 (2013), pp. 5116–5126.

[62] Robert T. McGibbon et al. "MDTraj: A Modern Open Library for the Analysis of Molecular Dynamics Trajectories". In: *Biophysical Journal* 109.8 (2015), pp. 1528–1532. arXiv: gr-qc/0102081 [gr-qc].

[63] Richard Gowers et al. "MDAnalysis: A Python Package for the Rapid Analysis of Molecular Dynamics Simulations". In: *Proceedings of the 15th Python in Science Conference*. 2016, pp. 98–105.

[64] Naveen Michaud-Agrawal et al. "MDAnalysis: A Toolkit for the Analysis of Molecular Dynamics Simulations". In: *J Comput Chem* 32 (2011), pp. 2319–2327.

[65] E. Jones, T. Oliphant, and P Peterson. *SciPy: Open source scientific tools for Python*. 2001.

[66] Stéfan Van Der Walt, S. Chris Colbert, and Gaël Varoquaux. "The NumPy array: A structure for efficient numerical computation". In: *Computing in Science and Engineering* 13.2 (2011), pp. 22–30.

[67] W McKinney. "Data Structures for Statistical Computing in Python". In: *Proceedings of the 9th Python in Science Conference* (2010), pp. 51–56.

[68] John D. Hunter. "Matplotlib: A 2D graphics environment". In: *Computing in Science and Engineering* 9.3 (2007), pp. 99–104.

[69] Eric Jankowski et al. "Perspective on Coarse-Graining , Cognitive Load , and Materials Simulation". In: *Computational Materials Science* Pending Re.April 2019 (2019), p. 109129.

[70] Peter Cummings. "Computational screening of soft materials systems with application to nano-lubrication systems". In: (2017).

[71]   Matthew W. Thompson et al. "Scalable Screening of Soft Matter: A Case Study of Mixtures of Ionic Liquids and Organic Solvents". In: *Journal of Physical Chemistry B* 123.6 (2019), pp. 1340–1347.

[72]   Mike Zhang et al. "Fluorinated Alcohols' Effects on Lipid Bilayer Properties". In: *Biophysical Journal* (2018), pp. 1–11.

[73]   John F Nagle et al. "Structure of gel phase DPPC determined by X-ray diffraction". In: *Chemistry and Physics of Lipids* 218.6 (2019), pp. 168–177.

[74]   E. A. Disalvo et al. "Functional role of water in membranes updated: A tribute to Träuble". In: *Biochimica et Biophysica Acta - Biomembranes* 1848.7 (2015), pp. 1552–1562.

[75]   J. Katsaras et al. "Evidence for a Two-Dimensional Molecular Lattice in Subgel Phase DPPC Bilayers". In: *Biochemistry* 34.14 (1995), pp. 4684–4688.

[76]   P. C. Mason et al. "Critical swelling in single phospholipid bilayers". In: *Physical Review E - Statistical Physics, Plasmas, Fluids, and Related Interdisciplinary Topics* 61.5 (2000), pp. 5634–5639.

[77]   Bradley C. Dallin and Reid C. Van Lehn. "Spatially Heterogeneous Water Properties at Disordered Surfaces Decrease the Hydrophobicity of Nonpolar Self-Assembled Monolayers". In: *The Journal of Physical Chemistry Letters* 10 (2019), pp. 3991–3997.

[78]   Bradley Dallin et al. "Molecular Order Affects Interfacial Water Structure and Temperature-Dependent Hydrophobic Interactions between Nonpolar Self-Assembled Monolayers". In: *Langmuir* 35 (2019), acs.langmuir.8b03287.

[79]   Remco Hartkamp et al. "Composition Dependence of Water Permeation Across Multicomponent Gel-Phase Bilayers". In: *Journal of Physical Chemistry B* 122.12 (2018), pp. 3113–3123.

[80] Christopher P. Baryiames, Morgan Teel, and Carlos R. Baiz. "Interfacial H-Bond Dynamics in Reverse Micelles: The Role of Surfactant Heterogeneity". In: *Langmuir* (2019), acs.langmuir.9b01693.

Chapter 4

Structure-Permeability Relationships in Gel-Phase Bilayers

4.1   Introduction

Dry skin ailments increase the rate of water loss through the skin, more specifically, the outermost layer of the skin known as the stratum corneum (SC). As a result, the overall health and barrier function of the SC is compromised. The SC is often represented using the brick-and-mortar model, where the bricks correspond to the dead corneocytes and the mortar corresponds to a lipid matrix composed of ceramides, cholesterol, and free fatty acids..[1–8] Topical formulations attempt to mimic healthy SC in order to restore health and barrier function to compromised SC.[8] While the SC lipid matrix has demonstrated excellent occlusive properties through a tight lipid packing in a gel phase, ceramides are expensive and difficult to formulate; thus, less-expensive phospholipids are of greater interest for topical formulations.[9]

Experimentally, barrier function of the SC has been experimentally related to both the gel phase and orthorhombic packing of the lipid membranes.[1,2,4,5,7,10] The addition of emollients such as isostearyl isostearate (ISIS), saturated alcohols (OH), or saturated free fatty acids (FFA) to topical formulations have been shown to improve water barrier function in topical formulations by promoting an orthorhombic packing or improving the overall lipid ordering within the bilayers.[8,9,11] These results reflect early theoretical work relating lipid disorder and *gauche-trans-gauche* kink formation in lipid chains to increased solute permeability.[12–14] While some experimental work has identified some components that improve barrier function and some theoretical work has laid out some of the fundamental factors and mechanisms of permeability through highly-organized, slowly-moving lipid bilayers, further work is necessary to gain an atomistic, chemical understanding of

water permeability through gel-phase, phospholipid bilayers.

Computationally, there have been many permeability studies for fluid-phase phospholipid bilayers, but fewer for gel-phase bilayers.[15–17] For studying fluid-phase permeability, the Hummer positional autocorrelation extension of the Woolf-Roux estimator has been commonly employed to calculate permeability.[18,19] However, significant sampling is necessary for fluid-phase systems, and the drastically slower lipid dynamics in gel-phase systems would require vastly more computational resources.[16] Usage of the Woolf-Roux estimator and weighted histogram analysis method (WHAM) to compute permeability has found success in studying permeability of solutes through gel-phase ceramide bilayers and multilayers.[20] Other methods applied to fluid-phase systems, including Bayesian inference schemes applied to the Smoluchowski equation, have yet to be applied to gel-phase systems, where sufficient sampling times have yet to be thoroughly studied.[16,21,22] When considering sufficient sampling times, gel-phase systems exhibit lipid lateral diffusion coefficients orders of magnitude slower than the fluid-phase counterparts, requiring orders of magnitude greater simulation times.[23] On the other hand, constrained molecular dynamics methods applied to the inhomogeneous solubility-diffusion model, developed by Marrink and Berendsen, have demonstrated applicability for both fluid-phase and gel-phase bilayers.[24–28] Das *et al.* and Notman *et al.* studied water permeability through gel-phase, SC atomistic models.[25–27] Hartkamp *et al.* explored the influence of ISIS and OH molecules on permeability through gel-phase phospholipid bilayers;[28] however, the influence of FFA molecules, a common component in topical formulations and the SC, has yet to be computationally examined.

This chapter presents permeability coefficients for a variety of multi-component, gel-phase phospholipid bilayers, validated by prior experiment and theory. Structure-permeability relationships are rationalized via the influence of bilayer composition on resultant atomistic interactions. To reduce the computational expense associated with gel-phase permeability calculations, a bootstrapping method is presented.

4.2 Computational Methods

4.2.1 System Setup

Bilayers were initialized using the mBuild software package.[29] Bilayers were constructed using two leaflets consisting of molecules arranged in an 8x8 square lattice. Lattice spacing was chosen to be about 20% larger than the final area per lipid based on earlier work.[30,31] Lipids were tilted randomly between 5 and 25° with respect to the bilayer normal and randomly placed along leaflets. Lipids were also randomly spun around their tail vectors to avoid artificial alignment found in other work.[32] Bilayers were solvated with 20 water molecules per lipid for a total of 2560 water molecules.

Two- and three-component mixtures of DSPC, OH, and FFA were examined. Two-component mixtures consisted of either 33% or 50% DSPC, with the remainder either OH or FFA. Three-component mixtures consisted of either 33% or 50% DSPC, with the remainder equimolar OH and FFA. In all mixtures, OH and FFA tail lengths were varied to either 12, 16, or 24 carbons (OH12, FFA12, etc.).

4.2.2 Simulation Protocol

Equilibration simulations were performed using the GROMACS 2018 MD simulation package.[33–38] DSPC, OH, and FFA molecules were parametrized according to CHARMM-GUI in accordance with the CHARMM36 all-atom force field.[39,40] Water was modeled using TIP3P and constrained using the SETTLE algorithm.[41,42] All other bonds containing hydrogen were constrained using the LINCS algorithm.[43] Electrostatics were computed using the particle mesh Ewald (PME) method.[44] Force-switching functions were used for van der Waals interactions between 10 and 12 Å.[39] Temperature was held at 305 K using a Nosé-Hoover thermostat with a 1.0 ps time constant.[39,45,46] Pressure was held semi-isotropically at 1 bar (XY and Z direction coupled separately) using a Parrinello-Rahman barostat with a 2.0 ps time constant.[47] Compressibility was held at 4.5 x 10^{-5} bar^{-1}. A 2

fs timestep was used.

Energy minimization was performed using steepest descent to remove any unfavorable overlaps between molecules. 100 ps of NVT equilibration followed by 500 ps of NPT equilibration was performed. Random Walk MD (RWMD) for a total of 190 ns was used to relax bilayer configurations away from any initial configuration bias.[48]

Moore *et al.* demonstrated the validity of RWMD to relax gel-phase ceramides, and we have adopted this method for gel-phase phospholipids.[48] RWMD involves a random walk through temperature space over the course of MD simulation by randomly swapping simulation temperatures with adjacent temperatures. Temperature moves are accepted or rejected according to a probability of acceptance criterion,[49]

$$P^{accept} = min(1, e^{f(T_{old}) - f(T_{new})})$$ (4.1)

where f is the frequency a particular temperature has been visited, T_{old} is the current temperature, and T_{new} is the proposed, new temperature.

Following RWMD, 100 ns of NPT sampling was performed at 305 K and 1 bar.

4.2.3 Structural Analysis Details

Atomic positions and simulation box dimensions were used to compute the area per lipid (APL), area per tail (APT), average tilt angle, and nematic order parameter (S2). The APL was computed by dividing the cross-sectional area of the simulation box by the number of lipids in the leaflet. The tilt angle was taken as the average angle between the long axis of a molecule's tail and the bilayer normal, with the long axis defined as the eigenvector corresponding to the minimum eigenvalue of the inertia tensor.[50] The APT was computed by dividing the APL by the average number of tails per lipid and multiplying by the cosine of the tilt angle. The S2 order parameter was computed as the largest eigenvalue of the nematic tensor, derived from the lipid tails in each leaflet.[48,51]
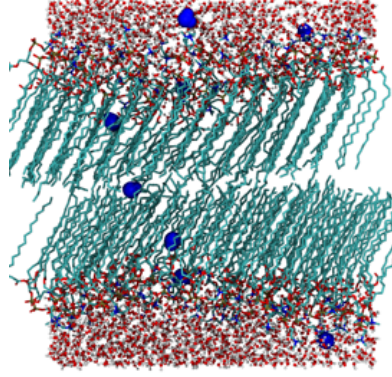
Figure 4.1: Z-constrained molecular dynamics. Specific water molecules (blue, enlarged) are constrained in the Z-direction, but allowed to roam in the XY-plane. Some unconstrained waters are omitted for visual clarity.

4.2.4 Inhomogeneous Solubility-Diffusion Model

The inhomogeneous solubility-diffusion model relates the free energy and diffusion properties to the permeation resistance and permeability coefficient.[24] Using Z-Constrained MD, molecules can be constrained to various points along the reaction coordinate (the Z direction in this study, see 4.1. By recording the Z-forces, F_z, acting on each molecule, the mean force and random forces can be identified.

Free energy profiles $\Delta G(z)$, can be derived from the mean forces, $< F_z >$

$$\Delta G(z) = - \int_{-\infty}^{z} < F_z(z) > dz \qquad (4.2)$$

In practice, the lower limit of the integral can be taken as a Z-coordinate within the bulk water, as we are only interested in the free energy barriers along the bilayer.

Local diffusion profiles, $D(z)$, can be derived from the autocorrelations of the random forces, $\Delta F_z(z,t) = F_z(z,t) - < F_z(z,t) >$.

$$D(z) = \frac{(k_B T)^2}{\int_0^{\infty} < \Delta F(z,t) \Delta F(z,0) > dt} \qquad (4.3)$$

In this equation, k_b is Boltzmann's constant, and T is temperature. In practice, the

upper limit of the integral can be taken as a finite time when the integral remains relatively stable and the autocorrelation decays to 0. For these systems, 300 ps is a sufficient upper bound for the autocorrelation functions to decay to 0 and the integral to remain sufficiently constant.[28]

Permeation resistance, R, can be derived from the free energy and diffusion profiles.

$$R = \int_{z_1}^{z_2} \frac{\exp \frac{\Delta G(z)}{k_B T}}{D(z)} dz \tag{4.4}$$

Finally, the permeability coefficient is calculated as the inverse of the permeation resistance.

$$P = \frac{1}{R} \tag{4.5}$$

4.2.5 Z-Constrained Molecular Dynamics Protocol

Simulations are continued from those outlined in earlier sections in this manuscript (4.2.2). GROMACS 2018 was used to pull randomly-selected water molecules to various depths in the bilayer.[33–38] Using mBuild[29] and Foyer,[52] simulations were converted into LAMMPS files. LAMMPS was used to conduct Z-constrained MD and sample the forces acting on each water molecule.[53] In both steps, water molecules were allowed to roam in the XY plane at a given depth and sample any lateral heterogeneity present in the bilayers. Supplemental simulations were performed to ensure consistency between the two MD software packages. Z-constrained simulations were run for 1 ns, which was a sufficient amount of time to sample multiple time decays of the force autocorrelation functions (about 200-300 ps). In one permeability sweep, water molecules were constrained to about 40 different Z-windows, depending on the height of the bilayer. Windows were spaced 2 Å. 20 sweeps were performed for each bilayer composition. Simulations were conducted at 1 atm and 305 K.

4.2.6 Bootstrap Methods

Bootstrapping is a statistical technique that involves resampling (with replacement) from a given sample (the distribution of data gathered).[54] From a single sample distribution, we can canonically obtain a single value for an estimator or statistic. By resampling with replacement from the original sample distribution, we can generate many samples. From these bootstrap distributions, we can obtain many bootstrap estimates. This range of bootstrap estimates can provide information about the variability in our desired estimate. It is worth noting the assumptions built into the bootstrap method: each individual sample is independent from the others, the sample distribution represents the population distribution, and the estimate is normally distributed.

Given the computational expense for permeability simulations of gel-phase bilayers and finite computational resources, bootstrapping provides a promising method of improving the reliability of permeability estimates. Each permeability sweep is conducted independently, although the initial configuration is taken to be the same equilibrated, probable configuration from the extensive equilibration protocol mentioned earlier 4.2.2. Since this is the same methodology that would be applied with extensive computational resources, the sample distribution well-represents the population distribution. Within the central limit theorem, we believe the bootstrap distribution of permeability values to reasonably follow a normal distribution.

From a set of permeability simulations, we can generate a sample distribution of permeability coefficients. This sample distribution is bootstrapped to generate a more reliable estimate of the permeability and variance of the permeability for a given bilayer composition. Efron and Tibshirani also note the statistical improvement by applying transformations to the data in order to improve the normal approximation to the dataset.[54] In this study of bilayer permeability, we note the apparent logarithmic scale of the permeability coefficient. Furthermore, experimental literature suggests a lognormal distribution of water permeability.[55,56] We apply the bootstrap method to the logarithm of the permeability coefficient in

order to bootstrap a more normally-distributed sample.

4.3   Results and Discussion

4.3.1   Bootstrap Validation

Preliminary results have been obtained for a DSPC bilayer 20 simulations. Figure 4.2 presents the normalized histogram of the log-permeability, log(P), coefficients. This distribution is fairly normal, suggesting that the gathered distribution of permeability coefficients is log-normal. This reinforces the use of the logarithm of permeability coefficients.
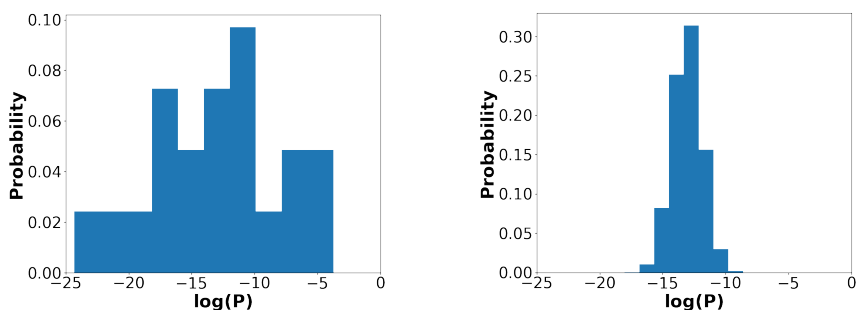
Figure 4.2: Probability distribution (left) and bootstrapped probability distribution (right) of log(P)

Applying the bootstrapping approach (100,000 bootstrap samples of size 20 or more) to 20 ns simulations of the DSPC bilayer yields a log(P) of -13.04 with a standard error of 0.26. This corresponds to a permeability coefficient of 2.16e-6 $\frac{cm}{sec}$ (naïve averaging of the same data set yields a permeability coefficient of 1.72e-3 $\frac{cm}{sec}$). For comparison, Hartkamp *et al.* sampled for 46 to 98 ns and reported a value of 1.4e-8 $\frac{cm}{sec}$ with an error of 3.6e-9 $\frac{cm}{sec}$ (this was using SPC water and the GROMOS53A6 force field).[28] Experimental evidence at 293 K reports a diffusive permeability of 8.1e-7 $\frac{cm}{sec}$.[57] Assuming both force fields are sufficient lipid models, both the bootstrapping and non-bootstrapping approaches can yield results within an order of magnitude of experiment, although the bootstrapping approach can yield reliable results with less simulation (20 ns in this simulation as opposed to 46 to 98 ns). For

further comparison, Das *et al.* performed 30 ns simulations of stratum corneum bilayers at 305 K and found water permeability coefficients around 3.7e-9 $\frac{cm}{sec}$ (without bootstrapping), while corresponding experimental results report permeability coefficients on the order of 1e-7 $\frac{cm}{sec}$.[27] By comparing methodologies with similar numbers of simulations (20 ns in this study vs 30 ns from Das *et al.*),[27] bootstrapping can yield results within an order of magnitude closer to experimental results compared to naïve methods.

To gather accurate free energy and diffusion profiles, similar bootstrapping methodologies were used. At a given reaction coordinate, the free energy distribution is roughly normal, while the diffusion distribution is roughly log-normal. Symmetrized free energy and diffusion profiles are shown in Figure 4.3. For validation, the self-diffusion coefficient of bulk TIP3P water at 301 K is presented.[58] Using the auto-correlations of the random forces, the calculated diffusion of TIP3P water in the solvent phase is in agreement with the self-diffusion coefficient of bulk TIP3P water.

When looking at qualitative composition-permeability trends found via simulation, the trends appear to agree well with those found in experiment by Bulsara *et al.*.[9] Permeability coefficients are presented in Table 4.1. The agreement in qualitative trends between simulation and experiment validates our method to efficiently compute permeability coefficients through gel-phase, lipid bilayers.
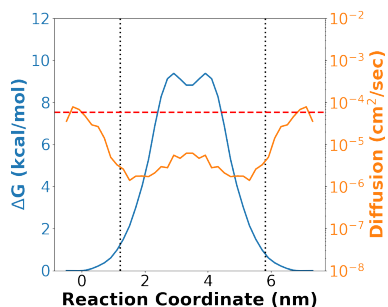
Figure 4.3: Bootstrapped-free energy profile (blue), bootstrapped-diffusion profile (orange), and self-diffusion coefficient of bulk TIP3P water (red). Bilayer head group depths are shown in black dotted lines for reference

Table 4.1: Computed structural properties and permeability coefficients for gel-phase bilayers studied

System	APT ($\mathring{A}^2$)	S2	Log(P)	P ($\frac{cm}{sec}$)
DSPC	19.73 (0.02)	0.964 (0.0010)	-13.04 (0.26)	2.16e-06 (0.56)
50% DSPC, 50% FFA12	19.82 (0.03)	0.963 (0.0013)	-13.04 (0.19)	2.17e-06 (0.41)
50% DSPC, 50% OH12	19.17 (0.03)	0.982 (0.0003)	-17.89 (0.32)	1.70e-08 (0.54)
50% DSPC, 50% FFA16	19.27 (0.01)	0.981 (0.0005)	-14.52 (0.24)	4.94e-07 (1.19)
50% DSPC, 50% OH16	18.85 (0.01)	0.986 (0.0001)	-24.69 (0.28)	1.89e-11 (0.53)
50% DSPC, 50% FFA24	19.21 (0.02)	0.975 (0.0009)	-16.85 (0.26)	4.81e-08 (1.25)
50% DSPC, 50% OH24	19.17 (0.02)	0.980 (0.0014)	-16.18 (0.28)	9.39e-08 (2.63)
50% DSPC, 25% OH24, 25% FFA24	19.70 (0.04)	0.973 (0.0012)	-20.54 (0.27)	1.20e-09 (0.56)
33% DSPC, 67% FFA12	19.84 (0.04)	0.971 (0.0010)	-15.55 (0.16)	1.77e-07 (0.28)
33% DSPC, 67% OH12	19.37 (0.02)	0.979 (0.0004)	-18.85 (0.33)	6.50e-09 (2.15)
33% DSPC, 67% FFA16	19.32 (0.02)	0.982 (0.0006)	-23.19 (0.24)	8.48e-11 (2.04)
33% DSPC, 67% OH16	18.94 (0.01)	0.987 (0.0004)	-21.09 (0.27)	6.96e-10 (1.88)
33% DSPC, 67% FFA24	19.03 (0.02)	0.982 (0.0010)	-25.43 (0.30)	9.06e-12 (2.72)
33% DSPC, 67% OH24	18.75 (0.02)	0.984 (0.0004)	-21.40 (0.36)	5.07e-10 (1.83)
34% DSPC, 33% OH16, 33% FFA16	19.04 (0.02)	0.985 (0.0007)	-21.65 (0.30)	3.98e-10 (1.19)

4.3.2 Composition, Structure, Permeability Relationships

Theoretical studies relate liquid-crystalline bilayer permeability to lipid chain ordering (measured via CH_2 symmetric stretching frequencies) and lipid lateral diffusion.[12–14,59] In the Trauble-Haines-Liebowitz model, more-ordered bilayers demonstrate fewer void spaces for water molecules to occupy; furthermore, bilayers with slower-moving lipids exhibit slower dynamics for the void spaces to form and propagate from one end of the

lipid chain to the other end.[12–14,59] Our computational findings largely support this model, observing the better-packed lipids (lower APT, higher S2) exhibit lower permeability 4.4. Due to the somewhat kinetically-artificial nature of the pulling and constraining, our simulations are not well-suited to shed light on the mechanisms of permeation; our simulations are; however, well-suited to sampling thermodynamic and transport properties by measuring the forces at various depths within the bilayer. We also observe the reduced permeability for some multi-component DSPC bilayers compared to our pure DSPC bilayers, consistent with experimental findings by Bulsara *et al.*.[9]
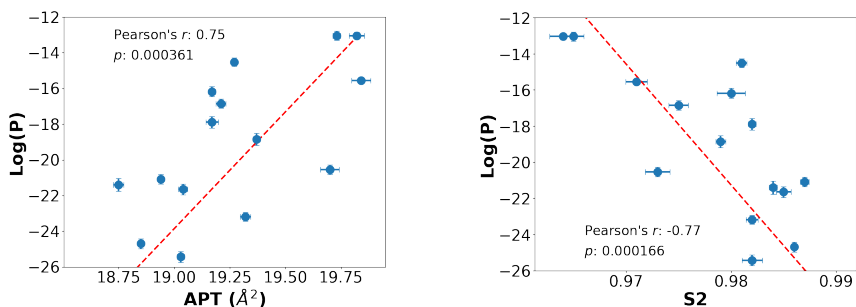
Figure 4.4: Permeability coefficients compared to APT (left) and S2 (right). APT appears to have a positive correlation with permeability. S2 appears to have a negative correlation with permeability

While structure-permeability relationships have been well-documented through phospholipid bilayers (more tightly-packed bilayers demonstrate lower permeability), the role of composition has yet to be elucidated. In earlier work, we presented a composition-structure study for gel-phase phospholipid bilayers, but here we briefly discuss composition effects on offset, APT, and S2. APT and S2 appear very related – a tighter-packed bilayer (lower APT) results in a more-organized bilayer with fewer defects (higher S2), and vice versa. In general, gel-phase bilayer structure is dictated by a balance of steric repulsion from head groups and van der Waals attractions from lipid tails.

In gel-phase bilayers, shorter-tailed components tend to localize more deeply within the bilayer. As a result, the head groups of shorter components localize closer to the lipid

tails and those of longer components localize closer to the bilayer-water interface. Shorter components with head groups nestled closer to the lipid tails introduce steric repulsions in the tail region, disturbing the packing and mostly *trans* configurations in the lipid tails. As a result, APT increases and S2 decreases in systems with shorter-tailed components. This is most notable in the mixtures containing FFA12, which exhibit inefficient packing and large permeability (see Figure 4.5).
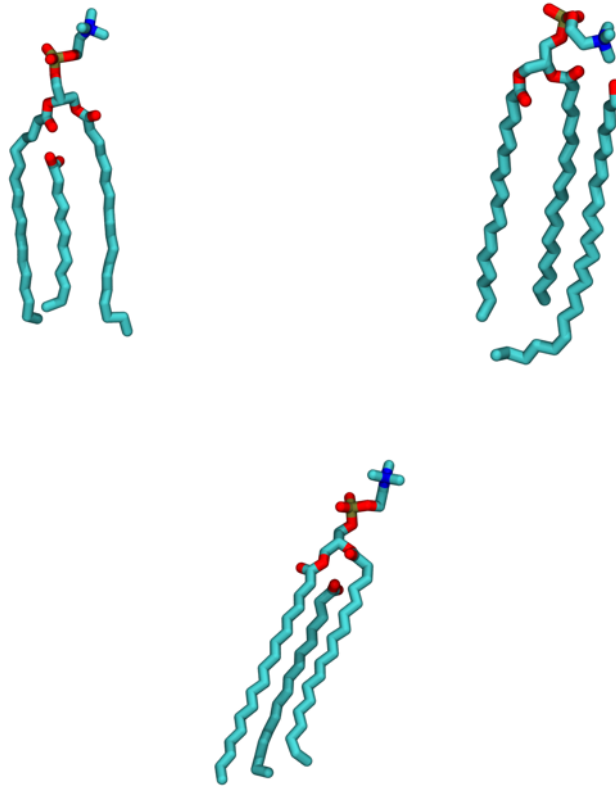
Figure 4.5: Snapshots of lipids in 33% DSPC, 67% FFA12 (left), 50% DSPC, 50% OH24 (right), 50% DSPC, 50% FFA16 (bottom) mixtures. Shorter components induce disorder around ester groups and tail ends due to head group offset and tail-length asymmetry. Longer components induce disorder around tail ends. Symmetric tails show greater order and improved packing.

On the other hand, components with longer tails cannot be supported and aligned by shorter tails, exhibiting more disorder. The tail-length asymmetry introduces disorder that reduces the lipid tail packing. This is most notable in mixtures containing OH24, which

exhibit inefficient packing and large permeability (see Figure 4.5).

While increasing the number or length of lipid tails can improve the van der Waals attractions and bring lipid tails together, the resultant tail length asymmetry introduces disorder that can reduce packing efficiency. Due to these competing effects, there appears to be a balance-point in which component tail length yields the tightest packing (see Figure 4.5).

For OH systems, tail-length symmetry (OH16) appears to improve packing and barrier function in 50% DSPC systems. In 33% DSPC systems, OH16 and OH24 mixtures exhibit similar packing and barrier properties.

For FFA systems, the larger head group introduces greater steric repulsions compared to OH systems, which can be ameliorated by introducing more van der Waals attractions via more two-tailed DSPC molecules or lengthening the FFA components. In 50% DSPC systems, tail-length symmetry (FFA16) appears to improve packing and barrier function. On the other hand, in 33% DSPC systems, lengthening the FFA component appears to improve packing and barrier function. This may be possible due to a greater fraction of long tails able to align with each other. However, there may be a point at which lengthening the FFA components will eventually introduce enough tail-length asymmetry and disorder to reduce packing and barrier function in 33% DSPC systems.

It is also worth comparing these trends with the properties of the pure DSPC system. Although the pure DSPC system has symmetric tails throughout the leaflet, the source of disorder and inefficient packing comes from the large phosphocholine head groups that sterically repel each lipid molecule apart (see Figure 4.6). Consequently, the pure DSPC system exhibits a somewhat large permeability.

In general, gel-phase bilayer mixtures with longer tails and tail-length symmetry yield the most densely-packed structures with the lowest water permeability.

The Trauble-Haines-Liebowitz model also considers interfacial behavior to influence the initial formation of kinks, thus having a possible influence on permeability.[12–14,59] Fig-
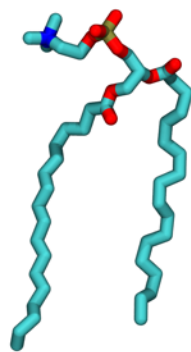
Figure 4.6: Snapshot of DSPC in pure DSPC bilayer. Large head groups drive lipid tails apart and induce disorder

ure 4.7 presents permeability correlations with intra-bilayer hydrogen bonding at the interface in addition to interfacial water dipole relaxation. The weak correlation coefficients, presence of possibly highly-influential data points, and large noise in structural quantities suggest that interfacial properties have little to no influence on water permeability.
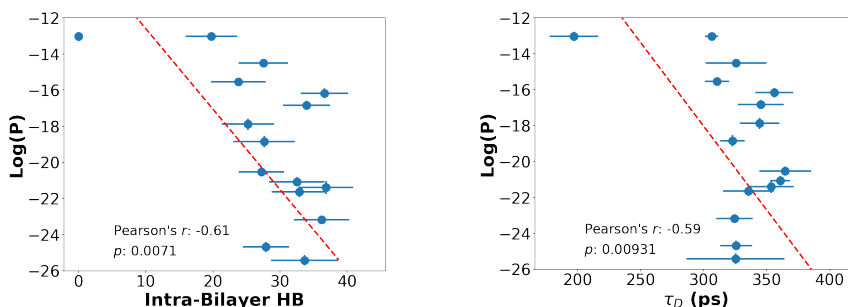
Figure 4.7: Permeability coefficients compared to intra-bilayer hydrogen bonding (HB, left) and water dipole relaxation (τ_D, right). HB appears to have a very weak correlation with permeability. Dipole relaxation appears to have a very weak correlation with permeability

Some preliminary experiment and simulation comparison can be found in the Appendix B. It should be noted that corresponding experimental WVTR measurements are computed from formulations containing a dilute fraction of phospholipid and OH/FFA, thus muting the influence of composition on experimental barrier properties compared to simulations of more-concentrated systems.

4.3.3 The Influence of Ripples on Water Permeability

Phopsholipid bilayers have computationally and experimentally demonstrated a ripple phase between gel and fluid phase temperatures.[60–63] Although the ripple phase is mainly a transition phase between gel and fluid, phospholipid bilayers at physiological temperatures (about 305 K) could exhibit some transient ripple domains in addition to gel domains. For example, DPPC molecules, which have shorter tails than those of DSPC molecules by two carbons, have demonstrated ripple phases at 311 K.[23] The presence of such ripples could have an effect on the permeability properties, providing a potential route for water permeation (see Figure 4.8).
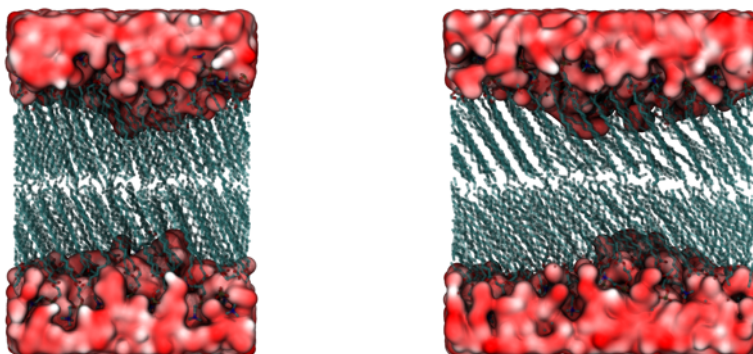
Figure 4.8: DSPC bilayers show some signs of disordered regions or ripples at 305 K. Snapshots are from the same configuration but different angles.

To examine the influence, similar constrained simulations were performed, except water molecules were pulled into the location of the bilayer kinks, which are regions of disorder similar to ripples. Free energy and diffusion profiles for ripple-phase sampling are presented in Figure 4.9. For comparison, uniform lateral sampling profiles from earlier are presented again. Through the bilayer kink, the permeability coefficient is estimated to be 5.21e-5$\frac{cm}{sec}$. For comparison, the uniform lateral sampling case exhibits a lower permeability coefficient of 2.16e-6$\frac{cm}{sec}$. The formation of the ripple creates an environment more similar to that of bulk water, reducing the free energy barrier and facilitating permeation.

However, given that the ripple phase temperatures are generally higher than physiological temperatures, any formation of ripples is likely to be short-lived.
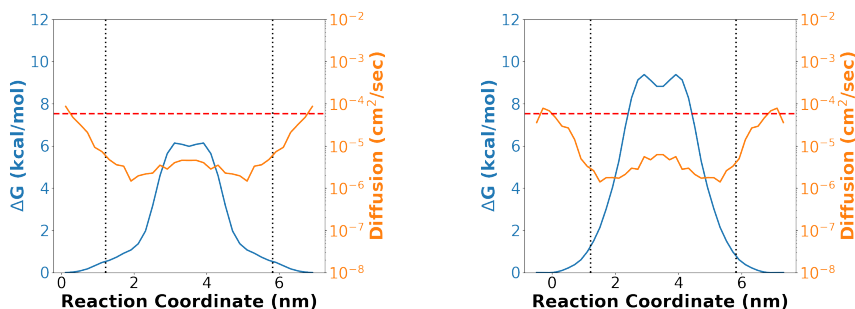
Figure 4.9: Free energy (blue) and diffusion (orange) profiles of water permeation with ripple sampling (left) and uniform lateral sampling (right). Self-diffusion coefficient of bulk TIP3P water is shown in red. Bilayer head group depths are shown in black dotted lines for reference.

4.4   Conclusions

We utilize constrained molecular dynamics, the inhomogeneous solubility-diffusion model, and bootstrap methods to study water permeability through multi-component, gel-phase phospholipid bilayers. Our structure-permeability trends are consistent with those found via theory and experiment. When looking at composition effects, we find that gel-phase bilayers with longer tails and tail-length symmetry yield the most densely-packed structures with the lowest permeability. We also observe the influence of bilayer ripples on increased permeability in single-component DSPC bilayers. These findings help identify relevant factors for designing topical formulations with specific water barrier function.

4.5   Bibliography

[1]   Gonneke S K Pilgram et al. "Aberrant Lipid Organization in Stratum Corneum of Patients with Atopic Deramtitis and Lamellar Ichthyosis". In: *Journal of Investigative Dermatology* 117.3 (2001), pp. 710–717.

[2]   J. Van Smeden et al. "The important role of stratum corneum lipids for the cutaneous barrier function". In: *Biochimica et Biophysica Acta - Molecular and Cell Biology of Lipids* 1841.3 (2014), pp. 295–313.

[3]   J A Bouwstra et al. "Phase behavior of lipid mixtures based on human ceramides: Coexistence of crystalline and liquid phases". In: *Journal of Lipid Research* 42.11 (2011), pp. 1759–1770.

[4]   Charlotte M Beddoes, Gert S Gooris, and Joke A Bouwstra. "Preferential arrangement of lipids in the long periodicity phase of a stratum corneum matrix model." In: *Journal of lipid research* (2018), jlr.M087106.

[5]   D Groen et al. "Is an orthorhombic lateral packing and a proper lamellar organization important for the skin barrier function?" In: *Biochimica et Biophysica Acta - Biomembranes* 1808.6 (2011), pp. 1529–1537.

[6]   Daniël Groen et al. "Investigating the barrier function of skin lipid models with varying compositions". In: *European Journal of Pharmaceutics and Biopharmaceutics* 79.2 (2011), pp. 334–342.

[7]   J. Caussin et al. "Interaction of lipophilic moisturizers on stratum corneum lipid domains in vitro and in vivo". In: *Skin Pharmacology and Physiology* 20.4 (2007), pp. 175–186.

[8]   G. Pennick et al. "The effect of an amphiphilic self-assembled lipid lamellar phase on the relief of dry skin". In: *International Journal of Cosmetic Science* 34.6 (2012), pp. 567–574.

[9] P. A. Bulsara et al. "The rational design of biomimetic skin barrier lipid formulations using biophysical methods". In: *International Journal of Cosmetic Science* 39.2 (2017), pp. 206–216.

[10] Michelle Janssens et al. "Increase in short-chain ceramides correlates with an altered lipid organization and decreased barrier function in atopic eczema patients." In: *Journal of lipid research* 53.12 (2012), pp. 2755–66.

[11] G Pennick et al. "Superior effect of isostearyl isostearate on improvement in stratum corneum water permeability barrier function as examined by the plastic occlusion stress test". In: *International Journal of Cosmetic Science* 32.4 (2010), pp. 304–312.

[12] R O Potts and M L Francoeur. "Lipid biophysics of water loss through the skin." In: *Proc. Natl. Acad. Sci.* 87.10 (1990), pp. 3871–3873.

[13] Thomas H Haines. "Water Transport Across Biological Membranes". In: *FEBS Letters* 346 (1994), pp. 115–122.

[14] Thomas H. Haines and L. S. Liebovitch. "Permeability and Stability of Lipid Bilayers". In: *Permeability and Stability of Lipid Bilayers*. Ed. by E. A. Disalvo and S. A. Simon. CRC Press, 1994. Chap. 6, pp. 123–136.

[15] Wataru Shinoda. "Permeability across lipid membranes". In: *Biochimica et Biophysica Acta - Biomembranes* (2016).

[16] Christopher T. Lee et al. "Simulation-Based Approaches for Determining Membrane Permeability of Small Compounds". In: *Journal of Chemical Information and Modeling* 56.4 (2016), pp. 721–733.

[17] Richard M. Venable, Andreas Kramer, and Richard W. Pastor. "Molecular Dynamics Simulations of Membrane Permeability". In: *Chemical Reviews* (2019), pp. 147–160.

[18] Thomas B. Woolf and Benoît Roux. "Conformational Flexibility of o-Phosphorylcholine and o-Phosphorylethanolamine: A Molecular Dynamics Study Solvation Effects". In: *Journal of the American Chemical Society* 116.13 (1994), pp. 5916–5926.

[19] Gerhard Hummer. "Position-dependent diffusion coefficients and free energies from Bayesian analysis of equilibrium and replica molecular dynamics simulations". In: *New Journal of Physics* 7 (2005).

[20] Eric Wang and Jeffery B. Klauda. "Structure and Permeability of Ceramide Bilayers and Multilayers". In: *Journal of Physical Chemistry B* 123.11 (2019), pp. 2525–2535.

[21] Christophe Chipot and Jeffrey Comer. "Subdiffusion in Membrane Permeation of Small Molecules". In: *Scientific Reports* 6.1 (2016), p. 35913.

[22] Jeffrey Comer, Klaus Schulten, and Christophe Chipot. "Permeability of a Fluid Lipid Bilayer to Short-Chain Alcohols from First Principles". In: *Journal of Chemical Theory and Computation* (2017), acs.jctc.7b00264.

[23] John L R Rubenstein, Barton A Smith, and Harden M Mcconnell. "Lateral diffusion in binary mixtures of cholesterol and phosphatidylcholines". In: *Proceedings of the National Academy of Sciences USA* 76.1 (1979), pp. 15–18.

[24] Siewert-Jan Marrink and Herman J. C. Berendsen. "Simulation of water transport through a lipid membrane". In: *Journal of Physical Chemistry* 98.15 (1994), pp. 4155–4168.

[25] R Thind et al. "Ethanol induces the formation of water-permeable defects in model bilayers of skin lipids." In: *Chemical communications (Cambridge, England)* 51.25 (2015), pp. 5406–9.

[26] Annalaura Del Regno and Rebecca Notman. "Permeation pathways through lateral domains in model membranes of skin lipids". In: *Physical Chemistry Chemical Physics* 20.4 (2018), pp. 2162–2174.

[27] Chinmay Das, Peter D Olmsted, and Massimo G Noro. "Water permeation through stratum corneum lipid bilayers from atomistic simulations". In: *Soft Matter* 5.22 (2009), p. 8. arXiv: 0907.1664.

[28] Remco Hartkamp et al. "Composition Dependence of Water Permeation Across Multicomponent Gel-Phase Bilayers". In: *Journal of Physical Chemistry B* 122.12 (2018), pp. 3113–3123.

[29] Christoph Klein et al. "A Hierarchical, Component Based Approach to Screening Properties of Soft Matter". In: *Foundations of Molecular Modeling and Simulation: Select Papers from FOMMS 2015*. Ed. by Randall Q Snurr, Claire S Adjiman, and David A Kofke. Singapore: Springer Singapore, 2016, pp. 79–92.

[30] Remco Hartkamp et al. "Structural Properties of Phospholipid-based Bilayers with Long- Chain Alcohol Molecules in the Gel Phase". In: *Journal of Physical Chemistry B* 120.50 (2016), pp. 12863–12871.

[31] Remco Hartkamp et al. "Investigating the Structure of Multicomponent Gel-Phase Lipid Bilayers". In: *Biophysical Journal* 111.4 (2016), pp. 813–823.

[32] Karthik Uppulury, Patrick S. Coppock, and James T. Kindt. "Molecular Simulation of the DPPE Lipid Bilayer Gel Phase: Coupling between Molecular Packing Order and Tail Tilt Angle". In: *Journal of Physical Chemistry B* 119.28 (2015), pp. 8725–8733.

[33] Erik Lindahl, Berk Hess, and David van der Spoel. "GROMACS 3.0: a package for molecular simulation and trajectory analysis". In: *Molecular Modeling Annual* 7.8 (2001), pp. 306–317.

[34] David Van Der Spoel et al. "GROMACS: Fast, flexible, and free". In: *Journal of Computational Chemistry* 26.16 (2005), pp. 1701–1718.

[35] Berk Hess et al. "GROMACS 4: Algorithms for Highly Efficient, Load-Balanced, and Scalable Molecular Simulation". In: *Journal of Chemical Theory and Computation* 4.3 (2008), pp. 435–447.

[36] Sander Pronk et al. "GROMACS 4.5: a high-throughput and highly parallel open source molecular simulation toolkit". In: *Bioinformatics* 29.7 (2013), p. 845.

[37] Szilárd Páll et al. "Tackling Exascale Software Challenges in Molecular Dynamics Simulations with GROMACS". In: *Solving Software Challenges for Exascale: International Conference on Exascale Applications and Software, EASC 2014, Stockholm, Sweden, April 2-3, 2014, Revised Selected Papers*. Ed. by Stefano Markidis and Erwin Laure. Cham: Springer International Publishing, 2015, pp. 3–27.

[38] Mark James Abraham et al. "GROMACS: High performance molecular simulations through multi-level parallelism from laptops to supercomputers". In: *SoftwareX* 1-2 (2015), pp. 19–25.

[39] Sunhwan; Jo et al. "CHARMM-GUI: A Web-Based Graphical User Interface for CHARMM". In: *Journal of computational chemistry* 29 (2008), pp. 1859–1865. arXiv: NIHMS150003.

[40] Jeffery B Klauda et al. "Update of the CHARMM all-atom additive force field for lipids: validation on six lipid types". In: *The Journal of Physical Chemistry B* 114.23 (2010), pp. 7830–7843.

[41] William L. Jorgensen et al. "Comparison of simple potential functions for simulating liquid water". In: *The Journal of Chemical Physics* 79.2 (1983), pp. 926–935. arXiv: arXiv:1011.1669v3.

[42] Shuichi Miyamoto and Peter A Kollman. "Settle: An analytical version of the SHAKE and RATTLE algorithm for rigid water models". In: *Journal of Computational Chemistry* 13.8 (1992), pp. 952–962.

[43] Berk Hess. "P-LINCS: A Parallel Linear Constraint Solver for Molecular Simulation". In: *Journal of Chemical Theory and Computation* 4.1 (2008), pp. 116–122.

[44] Ulrich Essmann et al. "A smooth particle mesh Ewald method". In: *The Journal of Chemical Physics* 103 (1995), pp. 8577–8593.

[45] Shuichi Nosé. "A unified formulation of the constant temperature molecular dynamics methods". In: *The Journal of Chemical Physics* 81.1 (1984), pp. 511–519. arXiv: 9807099 [cond-mat].

[46] William G Hoover. "Canonical dynamics: Equilibrium phase-space distributions". In: *Phys. Rev. A* 31.3 (1985), pp. 1695–1697.

[47] Michele Parrinello and Aneesur Rahman. "Polymorphic transitions in single crystals: A new molecular dynamics method". In: *Journal of Applied physics* 52.12 (1981), pp. 7182–7190.

[48] Timothy C. Moore et al. "Effect of Ceramide Tail Length on the Structure of Model Stratum Corneum Lipid Bilayers". In: *Biophysical Journal* 114.1 (2018), pp. 113–125.

[49] Enzo Marinari and Giorgio Parisi. "Simulated Tempering: A New Monte Carlo Scheme". In: (1992). arXiv: 9205018 [hep-lat].

[50] S Mabrey and J M Sturtevant. "Investigation of Phase Transitions of Lipids and Lipid Mixtures by High Sensitivity Differential Scanning Calorimetry". In: *Proceedings of the National Academy of Sciences* 73.11 (1976), pp. 3862–3866.

[51] Shan Guo et al. "Simulation study of the structure and phase behavior of ceramide bilayers and the role of lipid head group chemistry." In: *Journal of chemical theory and computation* 9.11 (2013), pp. 5116–5126.

[52] Christoph Klein et al. "Formalizing atom-typing and the dissemination of force fields with foyer". In: *Computational Materials Science* 167.May (2019), pp. 215–227.

[53] S. Plimpton. "Fast Parallel Algorithms for Short Range Molecular Dynamics". In: *Journal of Computational Physics* 117.June 1994 (1995), pp. 1–19. arXiv: nag.2347 `[10.1002]`.

[54] B Efron and R Tibshirani. "Bootstrap Methods for Standard Errors, Confidence Intervals, and Other Measures of Statistical Accuracy". In: *Statistical Science* 1.1 (1986), pp. 54–75.

[55] Sabine Niederl et al. "Co-Permeability of 3 H-Labeled Water and 14 C-Labeled Organic Acids across Isolated Plant Cuticles 1 Investigating Cuticular Paths of Diffusion and Predicting Cuticular Transpiration". In: *Plant Physiology* 115 (1998), pp. 117–123.

[56] Peter Baur. "Lognormal distribution of water permeability and organic solute mobility in plant cuticles". In: *Plant, Cell and Environment* 20 (1997), pp. 167–177.

[57] M. Jansen and A. Blume. "A comparative study of diffusive and osmotic water permeation across bilayers composed of phospholipids with different head groups and fatty acyl chains". In: *Biophysical Journal* 68.3 (1995), pp. 997–1008.

[58] Pekka Mark and Lennart Nilsson. "Structure and dynamics of the TIP3P, SPC, and SPC/E water models at 298 K". In: *Journal of Physical Chemistry A* 105.43 (2001), pp. 9954–9960.

[59] E. A. Disalvo et al. "Functional role of water in membranes updated: A tribute to Träuble". In: *Biochimica et Biophysica Acta - Biomembranes* 1848.7 (2015), pp. 1552–1562.

[60] Thomas Kaasgaard et al. "Temperature-controlled structure and kinetics of ripple phases in one- and two-component supported lipid bilayers". In: *Biophysical Journal* 85.1 (2003), pp. 350–360.

[61] Pouyan Khakbaz and Jeffery B. Klauda. "Investigation of phase transitions of saturated phosphocholine lipid bilayers via molecular dynamics simulations". In: *Biochimica et Biophysica Acta - Biomembranes* 1860.April (2018), pp. 1489–1501.

[62] Stephanie Tristram-Nagle et al. "Structure of gel phase DMPC determined by x-ray diffraction". In: *Biophysical Journal* 83.6 (2002), pp. 3324–3335.

[63] K. Akabori and J. F. Nagle. "Structure of the DMPC lipid bilayer ripple phase". In: *Soft Matter* 11.5 (2015), pp. 918–926. arXiv: 15334406.

Chapter 5

Influence of Single-Stranded DNA Coatings on the Interaction Between Graphene

Nanoflakes and Lipid Bilayers

5.1   Introduction

Since its discovery,[1] graphene and other related materials (e.g., carbon nanotubes, fullerenes) have received considerable attention due to their physical and electronic properties,[2] and have shown promise for use in biomedical applications,[3–5] such as drug delivery,[6,7] tissue engineering,[8,9] gene delivery,[10] and biosensing.[11] In particular, one promising application is the use of graphene-based electrodes to measure membrane potential changes and detect electrical activity in neuronal networks. However, the efficiency of these graphene-based sensors falls off exponentially with the distance from the cell or tissue; as such, maximizing the efficiency of these devices requires graphene be placed close to the cell or tissue surface.[12] Bringing graphene in close contact to cell membranes may be problematic since graphene is reportedly cytotoxic[13] due to its ability to induce oxidative stress[14] and disturb cell membranes.[15,16] Furthermore, interactions between graphene and membranes could complicate their utility as sensors. For example, in experiments by Kitko *et al.*, cholesterol (CHOL) content increased and lipid packing enhanced when cells resided directly on single-layer graphene film,[17] which resulted in neurotransmission changes and activation of G protein-coupled receptors.[12]

The literature, in particular aided by molecular dynamics (MD) simulation, has established that the hydrophobicity of graphitic materials is a significant driving force in terms of their interactions with lipid membranes. For example, MD simulation calculations of the free energy of C60 buckyballs penetrating phospholipid membranes revealed a strong energetic driving force ($\sim 20\ \frac{kcal}{mol}$), for insertion into the membrane;[18] this hydrophobic

driving force was seen to increase by a factor $\sim$2 as the C60 adopts a more planar geometry (e.g., an open-shell buckyball, intermediate between a sphere and flat sheet).[19] This strong hydrophobic interaction has been directly related to membrane disruption in other studies. For example, atomistic simulation studies have shown that bare, partially inserted graphene nanoflakes (GNFs) extract lipids from pure phospholipid bilayers,[20] in order to shield the portion of the GNF exposed to water.[16,21] In other simulations, Santiago *et al.*, using a coarse-grained approach, observed graphene insertion and lipid rearrangement in liposomes, in addition to graphene-facilitated-lipid-extraction during vesicle fusion.[22] Using a mesoscale model, Zhang *et al.* reported that GNFs selectively remove cholesterol from phospholipid-cholesterol membranes,[21] which was hypothesized to be related to the strong ring stacking that occurs between cholesterol and graphene. In other work, simulations of smaller GNFs that could fully insert into the membranes, and thus shield the hydrophobic surface of the GNF from water, did not demonstrate signifcant membrane disruption or lipid extraction.[23] To this end, biomolecular coatings[4] hold promise as a means of mitigating the effects of the hydrophobicity of graphitic materials, reducing membrane insertion and disruption. DNA is an attractive choice for coating GNFs, as it has been shown that the nucleobases can readily adsorb onto the hydrophobic surface of graphitic materials due to dispersion an π-π stacking interactions.[24–30] Such coatings have been shown to increase the dispersibility of graphene in solution, which suggests that the adsorbed DNA is indeed effective at reducing the hydrophobic interaction of graphene with the environment.[31] Additionally, similar materials, such as DNA coated single-walled carbon nanotubes, have seen success in areas such as gene delivery, providing a strong basis for their use.[32] However, it is currently unknown how the presence of a DNA coating affects the interaction between GNFs and lipid bilayers and how it changes GNF's penetration and disruption of cell membranes.

In this work, the interactions between lipid membranes and both bare GNFs and GNFs coated with singled stranded DNA (ssDNA) are investigated via MD simulations with

atomistically-detailed molecular models using the CHARMM force field.[33–37] Bilayers are modeled as a mixture of 1,2-dioleoyl-sn-glycero-3-phosphocholine (DOPC) and CHOL. Bare GNF simulations are conducted to provide a baseline for comparison to coated GNFs and to compare, using atomistically detailed models, to the results of Zhang *et al.*, show found that CHOL is selectively removed from membranes.[21] The effect of ssDNA coating the GNFs is examined as a function of the ssDNA coating density, focusing on the impact of the coating on the penetration behavior of the GNF into the bilayer membrane. The effect of proteins and other molecules that naturally occur in biological systems are not considered in order to isolate the interactions between membranes, GNFs and ssDNA. Steered MD simulations, whereby GNFs are directed into the membrane, are also performed to further probe the molecular interactions and insertion of the bare and coated GNFs. To the best of our knowledge, this is the first computational study of the interaction between graphene-ssDNA complexes and lipid bilayers.

5.2   Simulation Methods and Models

Bilayer construction: Preassembled DOPC-CHOL bilayers containing 200 lipids per leaflet were generated via the CHARMM-GUI.[38–43] The mixed DOPC-CHOL bilayer contained 44 CHOL molecules per leaflet, randomly dispersed throughout the bilayer leaflets with an equal amount of CHOL molecules in either leaflet. The bilayers were immersed in water, such that there was approximately a 5 nm layer of water one ach side when considering small GNFs (5 nm x 5 nm) (i.e., 10 nm separation between the bilayer and its periodic image); simulations of larger GNFs (5 nm x 10 nm) double this separation between the bilayer and its periodic image. The configurations generated by the CHARMM-GUI are representative of equilibrated liquid-crystalline bilayers.[41,42] A steepest descent energy minimization was performed on the hydrated bilayers generated by the CHARMM-GUI, followed by a short isobaric simulation (i.e., simulated in the NPT ensemble) of 375 ps to ensure relaxation rior to the addition of GNF and/or DNA. It was confirmed that the bilayer

properties (i.e., area-per-lipid and bilayer height) were stable during this short simulation.

GNF construction: GNFs were created with the VMD carbon nanostructure builder.[44] Two GNFs with dimensions 5 nm x 5 nm and 5 nm x 10 nm were constructed. While in practice GNFs are generally on the order of hundreds of nm in lateral dimensions and can have more complex shapes,[45,46] the model GNFs in this study enable us to investigate how the edges and sharp corner that can be present on realistic GNFs interact with phospholipid bilayers. Additionally, these sizes allow us to examine: (1) a GNF that can fully insert in the bilayer and (2) a GNF that is large enough that the GNF does not fit completely within the hydrophobic core of the bilayer, yet allows for a system size (i.e., size of bilayer and water layer) small enough that it can be simulated with atomistic models without computational expense being a limiting factor.

ssDNA coating: ssDNA strands were initialized with the make-na server,[47] which uses the nucleic acid builder of AmberTools to construct geometrically accurate DNA molecules.[48] Sequences of single-stranded poly-G_{10} were initialized with a type-B helix. The ssDNA coils were approximately 3.5 nm long with a radius of 2 nm. The ssDNA chains were placed on each side of a 5 x 5 nm GNF. The chains were initially placed with their long axis parallel to the GNF, approximately 5 Å from the surface. The system was then solvated and neutralized with Na ions. 50 ns of simulated tempering[49] was performed with a temperature range $300 \leq T \leq 700K$, to allow the DNA molecules to adopt low-energy configurations on the GNF. The upper temperature limit of 700 K was chosen to induce large conformational changes in the ssDNA.[29] Since ring-ring stacking interactions are expected to drive the ssDNA-GNF complex towards configurations with the nucleobases lying flat on the GNF surface,[31] the ssDNA that had the most (eight out of ten) bases lying flat on the surface was used to build the coated GNF systems. The flat ssDNA chain is approximately 6 nm x 2 nm in size. These chains were replicated to generate sparsely, moderately, and densely coated GNFs by placing one, two, and three ssDNA molecules, respsectively, on each side of the GNF (referred to as 2 ssDNA, 4 ssDNA, and 6 ssDNA,

respectively, throughout the paper).

Simulation details: All simulations were performed in GROMACS 5.1[50–55] using a timestep of 1 fs. The non-bonded interaction potential was smoothly switched off between 10 and 12 Å, beyond which Coulombic interaction were tread with the particle-mesh Ewald method.[56] A temperature of 300 K was maintained via the Nosé-Hoover thermostat.[57,58] The simulation system was copuled semi-isotropically to the Parrinello-Rahman barostat to maintain a pressure of 1 atm independently in the bilayer normal and lateral directions.[59] The atomistic CHARMM36 force field was used to model DOPC and CHOL,[35] and TIP3P was used to model water.[60] Similar to a recent study,[61] the atoms in the graphene sheet were treated as aromatic ring carbons, i.e., type CG2R61 in the CHARMM General Force Field (CGenFF),[62] with the appropriate bond-stretching and angle-bending interactions also from CGenFF. Note, dihedral interactions were not included in the graphene model, consistent with the previous studies.[31] CHARMM27[33,63] was used to model the ssDNA.

GNF insertion simulations: In all cases, the GNF (coated or uncoated) was positioned with a corner pointing toward the bilayer surface approximately 0.5 nm from the bilayer surface. This orientation was chosen to increase the likelihood of insertion, based on preliminary tests and prior work that suggests GNFs typically insert into the bilayers in a corner-first fashion.[20] With the exception of the steered simulations discussed later, the position/orientation of the GNF was not constrained prior to insertion, and was allowed to freely move throughout the system in all directions; since periodic boundary conditions are used, the GNF is able to interact with either side of the membrane further increasing the likelihood of insertion. For systems with ssDNA molecules, overlapping water molecules were removed and neutralizing Na ions were added; these systems each contained approximately 170,000 atoms. The complete process of constructing the system is graphically shown in the AppendixC. A steepest descent energy minimization was performed to remove high-energy atomic overlaps, after which systems were simulated in the NPT ensemble. For simulations with ssDNA coatings, simulation times ranged from 60 to 508 ns,

depending on the time required for penetration/steady state behavior to occur, where, in general, simulation time increase with coating density. Four independent simulations were performed for the insertion of bare GNF and six for each of the three ssDNA coating densities studied. The individual simulation times for the coated GNF simulations are reported in Table 5.1.

Steered MD procedure: Steered MD simulations were conducted by attaching harmonic springs to the corner of the GNF and then pulling the GNF into the bilayer midplane over the course of a 5 ns simulation for the 5 nm x 5 nm GNF as a function of the ssDNA coating. The bilayer was not held fixed, but no noticeable drift was observed over the course of the short simulation. As described in the results, a spring constant (k) of 50 kJ mol^{-1} nm^{-2} was chosen for these calculations as it provided the closest match to the free (i.e., non-steered) simulations in terms of penetration depth. The force of the harmonic spring and the distance traveled by the GNF is recorded during the course of these simulations and the work computed by integrating the force over the distance traveled.

5.3   Results and Discussion

5.3.1   Bare GNF insertion

The prototypical insertion of a small (5 nm x 5 nm) unrestrained, bare GNF into a phospholipid-cholesterol bilayer is shown in 5.1. From a visual inspection of the simulation trajectory, the penetration occurs corner first with the sheet oriented roughly perpendicular to the bilayer surface, in agreement with the preferred orientation from other work.[20] To quantify the insertion process beyond visual inspection, three metrics are considered: (1) the distance, D, between the center-of-mass of the GNF and the center-of-mass of the bilayer, projected in the direction normal to the bilayer (5.1g); (2) the magnitude of the dot-product between the two measures indicates a corner first orientation when the GNF is aligned with the bilayer normal (labeled as "corner" in 5.1h); (3) and the angle between

GNF and bilayer normal (see 5.1i), where a value of 0° indicates perpendicular alignment with the bilayer interface. These measures confirm a rapid (< 5 ns) insertion of the GNF into the bilayer after it initially comes into close contact, where insertion is indeed corner first and with the GNF slightly tilted with respect to the bilayer normal ($\sim 10°$). The corner first orientation of the GNF, whereby part of the GNF is exposed to water, results in a small number of DOPC molecules partially extracted from the bilayer to shield the hydrophobic surface as shown in Figure 5.1c, d. This corner first orientation persists until ~ 30 ns (5.1e), at which point the GNF reorients slightly do adopt a more edge-first configuration, as evidenced visually by the final simulation snapshot (5.1f) and by the change in the value of the corner orientation metric (5.1h); this reorientation allows the GNF to be more effectively shielded by the membrane. At the end of the simulation, the GNF has further aligned with the bilayer normal (i.e., tilt angle $\sim 10°$, in Figure 5.1i). This alignment with the bilayer normal is not unexpected since the lipids in the fluid-state bilayer do not adopt a uniform tilt angle that might otherwise GNF orientation. A small amount of disruption around the GNF is observed at the bilayer-water interface at the end of the simulation (e.g., see 5.1f), where a small number of DOPC molecules nearest the GNF have risen up slightly from the membrane to provide additional shielding, since the GNF is slightly larger than the height of the membrane tail-region. We note that there does not appear to be any significant disruption of the membrane itself aside from the small region around the GNF at the end of the simulation. These results are consistent with Chen *et al.* who also considered a GNF whose dimensions closely match that of the bilayer height, and did not observe any significant bilayer disruption.[23]

(a) 2 ns   **(b)** 4 ns   **(c)** 6 ns

(d) 10 ns   **(e)** 30 ns   **(f)** 80 ns
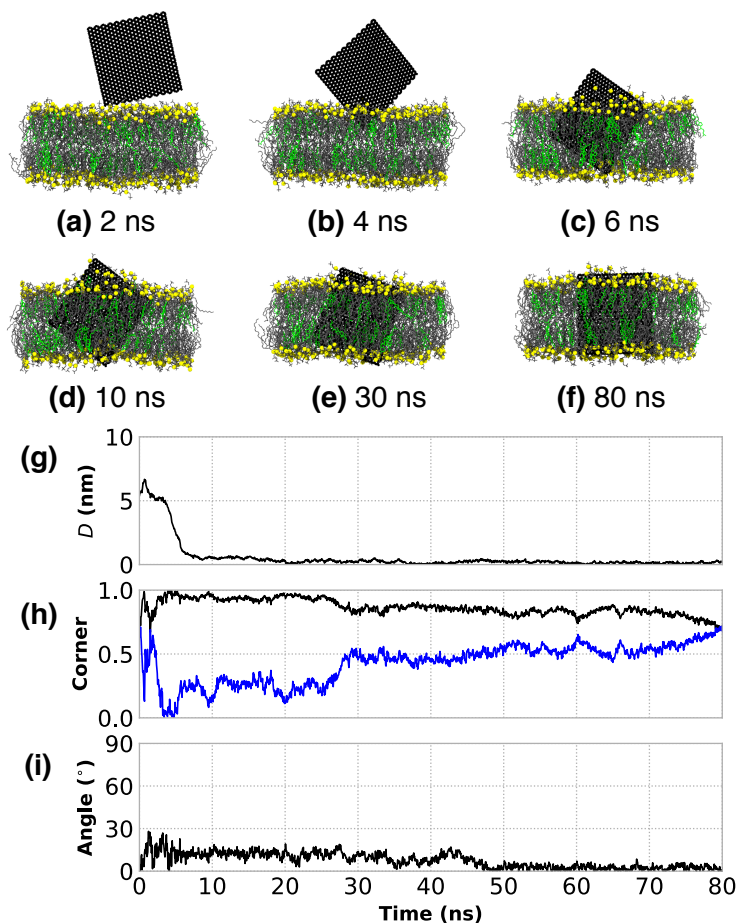
Figure 5.1: The rapid corner first, insertion of a bare 5 nm x 5 nm GNF into a bilayer. (a-f) Simulation renderings of the insertion process as a function of time; water is not shown for clarity, phosphorous atoms of DOPC are shown in yellow to highlight boundary, DOPC tails are shown as gray, and CHOL colored green. (g) Distance between the centers-of-mass of the GNF and bilayer, projected along the bilayer normal, shows the rapid insertion at ~ 8 ns. (h) The value of unity for normalized dot product calculated between the vectors describing the GNF diagonals (blue and black) and the bilayer normal indicates corner first insertion. (i) The angle between the GNF and bilayer normal, where GNF inserts at $\sim 10°$ from normal; after ~ 50 ns, the value is close to $0°$, closely aligned with the bilayer normal.

Figure 5.2a-f presents a second prototypical example of GNF insertion. In contrast to Figure 5.1, the insertion process is slower after the GNF first comes into close contact with the membrane, because the GNF initially lies flat upon the bilayer surface, as shown visually in Figure 5.2b, c, and evidenced by a value of $\sim 90°$ for the GNF angle between 20 and 50 ns plotted in Figure 5.2i. While this flat configuration is certainly less favorable than an

inserted configuration, coarse-grained studies of graphene and bilayer liposomes identified a similar configuration where lipids rearrange to coat the flat graphene configuration.[22] At $\sim$55 ns of simulation time, the GNF begins to extract a small number of phospholipids onto the GNF surface nearest the corner, as it begins to slowly increase its tilt and start a corner first insertion into the bilayer (Figure 5.2d, e); the corner first orientation metric (Figure 5.2h) increase towards unity during this stage from 55-100 ns. Note, in this case, the GNF is not perpendicular to the bilayer interface when insertion occurs at $\sim$60 ns, but instead at $\sim$60° with the GNF gradually transitioning to a more perpendicular alignment by the end of the simulations, as shown in Figure 5.2i. As in Figure 5.1, the edge first configuration of the GNF results in part of the GNF exposed to water, where again partial extraction of a small number of phospholipids is observed to coat the GNF (Figure 5.2e). Visually, near the end of the simulation time considered (150 ns, Figure 5.2f), the GNF maintains a configuration intermediate between a corner-first and edge-first orientation, with a small amount of DOPC partially extracted to coat the surface; increased simulation time would likely result in an edge first orientation, similar to 5.1, as this maximizes shielding of the GNF. A third independent trial in the AppendixC demonstrates behavior intermediate between the cases shown in Figures 5.1 and 5.2, where the GNF contacts the membrane at an unfavorable orientation ($\sim$70° from the bilayer normal) and reorients during insertion, but does not lie flat upon the bilayer surface.
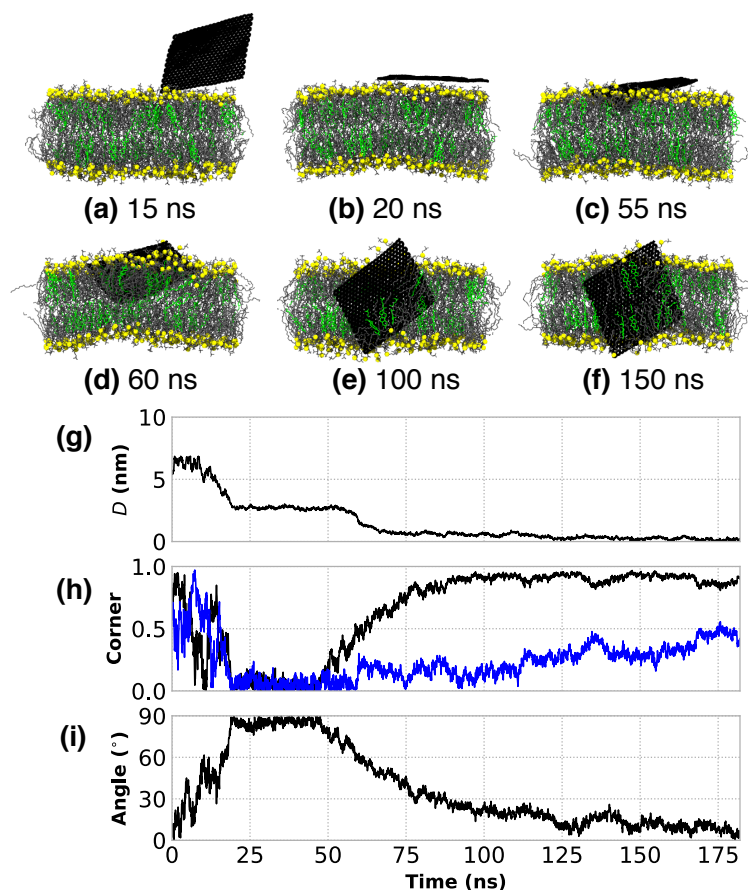
Figure 5.2: Insertion of a bare 5 nm x 5 nm GNF into the bilayer, whereby the GNF first adopts a "flat" configuration perpendicular to the bilayer normal. (a-f) Simulation renderings of the insertion process as a function of time; the same color scheme as Figure 5.1 is used. (g) The distance between the centers-of-mass of the GNF and bilayer, projected along the bilayer normal, capturing the flat configuration between ∼20-60 ns, and the eventual insertion at ∼60 ns. (h) The normalized dot product calculated between the vectors describing the GNF diagonals (blue and black) and the bilayer normal, capturing the corner first insertion as shown by the gradual increase towards unity of one of the vectors starting at ∼50 ns. (i) The value of ∼90° between ∼20 and 50 ns for the angle between the GNF and bilayer normal indicates the regime where the GNF adopts a flat configuration; the gradual increase towards 0° after ∼60 ns demonstrates that the GNF does not insert perpendicularly, but rather gradually aligns with the bilayer normal after insertion.

5.3.2 GNF-induced lipid extraction

Experimentally, GNFs are typically much larger (10-1000 μm) than the bilayer thickness (∼5 nm) and thus insertion would require the GNF to protrude from the bilayer, with

a significant portion of the hydrophobic surface exposed to water. To mimic a situation in which a large GNF penetrates a cell membrane and a portion of the GNF is still exposed to the extracellular fluid, simulations of an uncoated 5 nm x 10 nm GNF are considered. This configuration was realized by allowing an unrestrained GNF to freely penetrate into the bilayer and then, after insertion, restraining the motion of the GNF atoms in the direction normal to the bilayer using a harmonic potential with a force constant of 1000 kJ mol^{-1} nm^{-2}. The restraints were used to prevent the GNF from completely sinking into the bilayer, thus mimicking the more realistic case where the GNF is much larger than the bilayer thickness. Note, the insertion behavior of this larger GNF closely resembles that of the prototypical insertion shown in Figure 5.1 of the smaller 5 nm x 5 nm GNF. After insertion, lipids are extracted from the bilayer to coat the hydrophobic GNF surface as shown in Figure 5.3a, consistent with prior simulation studies.[16] This is also consistent with the partial extraction of lipids seen in Figures 5.1 and 5.2 for the corner first configuration of the smaller GNF. Visually, the lipids leave the bilayer in the direction roughly perpendicular to the perpendicular plane, without larger rotational motion or dragging surrounding lipids along. The extracted lipids on the GNF align with the GNF surface form an efficient packing and coat the GNF surface, where the hydrophilic phosphatidylcholine head groups of DOPC protrude from the GNF edge or perpendicular to its surface to maximize their exposure to water. Lipid extraction onto the GNF surface is quantified in Figure 5.3b by identifying lipids that are close to the surface of the GNF and 2.5 nm above/below the bilayer center-of-mass (roughly approximating the bilayer-water interface). A simple distance cutoff of 0.5 nm between a GNF carbon atom and the first carbon atom in the DOPC chain and the first carbon in the CHOL ring structure was used to identify molecules on the GNF surface. Figure 5.3b quantifies that the number of lipids increases until approximately 15 ns, consistent with visual inspection (see Figure 5.3a), at hwich point the values appear roughly constant ($\sim$20 total lipids). Figure 5.3c plots the solvent accessible surface area (SASA) of the GNF calculated using VMD[44] with a probe of 2.75 Å (roughly

the diameter of water). The SASA measurement rapidly decreases and becomes roughly constant at 15 ns, consistent with visual inspection and quantification of lipid extraction, and clearly demonstrates the role of lipid extraction as a means to shield the GNF from the water solvent. As the simulation time progresses, we visually observe that additional lipids are extracted from the bilayer (see Figure 5.3a), however these do not directly lie upon the GNF itself. These additional lipids coat the existing layer of lipids and act to further shield the hydrophobic lipid tails on the lipids GNF surface from water. Significant bilayer disruption is observed at the end of the 75 ns simulation time, as shown in Figure 5.3a.

As previously discussed, prior simulations have demonstrated that an uncoated GNF can disrupt bilayers by extracting lipids to cover the hydrophobic graphene surface.[13,16] Our simulations are consistent with these results and clearly demonstrate that the GNF must be larger than the dimensions of the bilayer height for such extraction to occur, i.e., the difference between the work of Tu *et al.*[16] where significant extraction was observed, and Chen *et al.*[23] where no extraction was observed, can be associated with the GNF size and not necessarily dependent on any other methodological differences. It is worth noting that Tu *et al.* performed simulations with very large GNFs, where there was an apparent, continual extraction of lipids due to the large availability of exposed sites on the GNF surface. For the simulations reported herein, a termination of lipid extraction directly onto the GNF is observed once there is no more available space on the surface of the GNF, although additional lipid extraction occurs to further envelope the lipids that lie directly on the GNF surface.
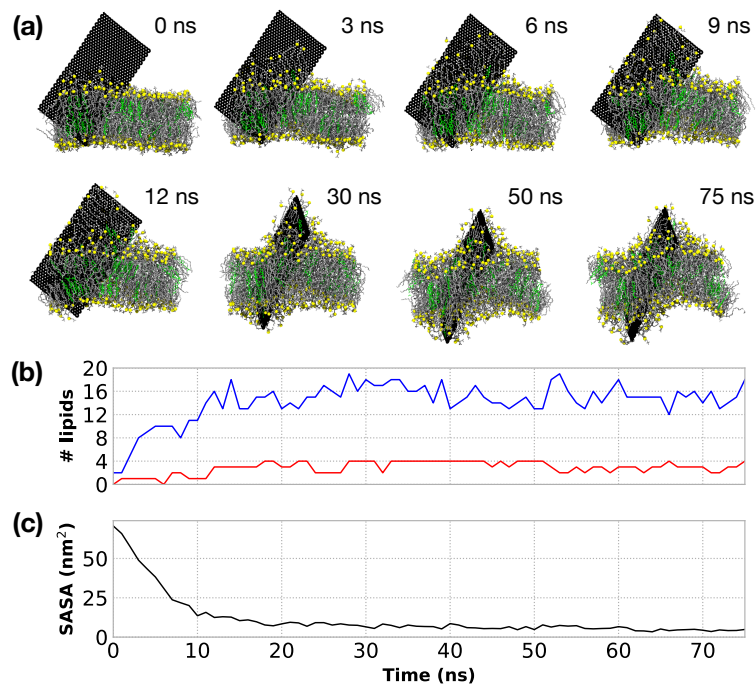
Figure 5.3: (a) Simulation snapshots of the extraction of lipids for a 5 nm x 10 nm GNF. The GNF surface is fully coated by a single layer of lipids ~15 ns. After which additional lipids are extracted to further coat the lipids already on the surface of the GNF, providing additional shielding of the lipid tails, resulting in significant membrane disruption by the end of the simulation time considered (75 ns). Phosphorus atoms shown in yellow, DOPC tails in grey, CHOL colored green. Water is not shown for clarity. The camera location is changed (i.e., rotated) for the final three snapshots to highlight the further extraction and disruption of the bilayer; the position of the GNF itself does not change during the course of the simulation due to the applied restraints. (b) Quantification of the number of lipids extracted from the bilayer. DOPC shown in blue and CHOL shown in red. (c) Calculation of the solvent accessible surface area of the GNF as a function of time.

Upon examination of extraction by lipid type, we find phospholipids are primarily extracted, with only a few CHOL molecules removed from the bilayer; this can be observed visually in Figure 5.3a and is quantified in Figure 5.3b. Specifically, at 12 ns, there are 16 DOPC molecules and 3 CHOL on the GNF (in the region outside the membrane) and these values remain roughly consistent throughout the remainder of the simulation. As such, the CHOL concentration on the GNF is approximately 16%, slightly lower than 22% concentration of CHOL in the membrane. The slight preference to DOPC extraction could be related to the hydrophilic phosphatidylcholine head group attenuating the cost of the DOPC

90

molecules to be near water, given that CHOL lacks a similarly large, flexible hydrophilic head group. While ring stacking of CHOL on the honeycomb surface of the GNF may result in a stronger binding, the results herein suggest that there is not a stronger driving force to extract CHOL from the bilayer compared to extracting DOPC. At best, the tendency for lipid extraction is equal between the two species and largely dictated by the lipid concentration in the membrane. This finding contradicts the results of Zhang *et al.*,[21] who found that CHOL molecules fully coated the GNF, while no phospholipids were extracted from the bilayer. We note that such drastic differences in behavior likely arise as a result of teh different models used; whereas the present work uses the fully atomistic CHARMM force field, the work presented in Zhang *et al.*[21] used a mesoscale dissipative particle dynamics (DPD) model. DPD relies on treating all interactions as repulsive, soft spheres, where spatial organization (e.g., such as a phase separation) are driven by the relative scale of the repulsion between beads. The findings of Zhang *et al.* are consistent with the fact that, in their DPD model, the repulsive force between graphene and phospholipid head or tail beads was set to much higher values than the repulsion between graphene and cholesterol beads in their simulations; modification of these strengths would likely result in a different behavior. Based on the atomistic simulations presented here, the interactions used by Zhang *et al.* do not accurately model the underlying behavior. Although no complete bilayer destruction occurred over the timescale considered for the 5 nm x 10 nm GNF system, a larger sheet would likely extract more lipids and thus have a larger influence on the bilayer structure. Furthermore, if DOPC is selectively removed, the relative concentration of CHOL must increase within the membrane, which could potentially alter the structure and behavior of the membrane (e.g., the creation of CHOL-rich microdomains). While our results strongly suggest CHOL is not preferentially extracted from the bilayer onto the GNF portion that is exposed to water, larger simulations and longer timescales would be required to investigate whether there is a preferential CHOL organization around the GNF within the bilayer membrane.

5.3.3 Influence of ssDNA coating on the Insertion of GNFs

Since the hydrophobic shielding provided by a bilayer drives the insertion of a GNF, the question arises whether a coating on the GNF, in this case ssDNA, can provide the same level of shielding and thus reduce or eliminate insertion. This question is explored by examining the insertion behavior of GNFs with different levels of ssDNA coating. Here, the insertion of small GNFs (5 nm x 5 nm) with differing levels of ssDNA on the surface (2, 4, and 6 ssDNA per GNF, distributed evenly on each side) into DOPC-CHOL bilayers are considered. We calculate the solvent accessible surface area (SASA) of the GNFs with a test particle of diameter 2.75 Å (approximate diameter of water) for each coating density at 1 ns (i.e., prior to insertion) using VMD.[44] For each of the six replicates an average GNF SASA of 49.8 ± 4.3, 33.8 ± 1.4, and 17.3 ± 0.5 nm^2 is found for the 2, 4, and 6 ssDNA per GNF systems, respectively. As expected, the ssDNA provides increased shielding of the GNF as the number of strands increases. The total GNF area occupied by ssDNA using SASA was also calculated and areas of 19.6 ± 3.2, 48.3 ± 6.6, and 65.1 ± 6.6 nm^2 were obtained for the 2, 4, and 6 ssDNA per GNF systems, respectively; these values are reported in 5.1 for each replicate and simulation snapshots of representative coated GNFs are included in Figure 5.4. For reference, the GNF itself (ignoring the lipids and ssDNA) has an average SASA of 77.7 ± 8.6 nm^2, calculated from the initial (at 1 ns) and final configuration of the GNF in the 18 replicates presented in Table 5.1 (note, this is higher than a simple area estimate of 50 nm^2 based on nominal dimensions of the GNF as the SASA calculation considers edge effects and does not treat the surface as perfectly smooth). The GNF SASA and area-occupied by the ssDNA do not scale linearly with the number of ssDNA, likely due to the fact that a larger number of ssDNA conformations/GNF binding locations are accessible for lower surface coverages of ssDNA than higher.

Table 5.1 reports the behavior as a function of ssDNA coating density for each of the 6 independent simulations performed for each coating density. Figure 5.4 provides a visualization of the final configuration of each of the 18 simulations presented in Table 5.1. Anal-

ysis of the center-of-mass separation and the orientation metrics as a function of time are presented in the Appendix C for each simulation. In general, as the ssDNA coating density increases, the likelihood of a GNF inserting into the bilayer is reduced (over the simulation timescales considered). For the lowest density, the GNF inserted in all six simulations, whereas only two simulations showed GNF insertion for the highest density. Similarly, as the ssDNA coating density increases, the center-of-mass separation (D) between the GNF and bilayer also increases, i.e., reduced insertion. This is because the ssDNA is not removed from the GNF surface after insertion and the ssDNA does not enter the bilayer, thus it prevents the GNF from fully penetrating into the bilayer. As such, while the hydrophobic driving force for insertion is insignificant, it is likely weaker than the ssDNA-GNF insertion, since the ssDNA remains largely adsorbed (note, this is discussed in more detail in the context of the steered simulations below). The number of ssDNA per side of the GNF remains constant during the simulations. We note that, as can be seen in the visualizations in Figure 5.4, there are several cases where parts of the ssDNA strand dangle from the edge of the GNF, although there are no cases where the ssDNA fully desorbed from the GNF over the course of the simulation times considered. This behavior can also be quantified by comparing the initial to final area occupied by the ssDNA on the GNF presented in Table 5.1, where significant drops in the area occupied by the ssDNA are observed for systems with dangling strands; in almost all cases, the area occupied by the ssDNA is reduced by the end of the simulations, related to the compaction of the ssDNA to a smaller portion of the GNF as a result of the penetration process. The simulation time taken for the GNF to reach a center-of-mass separation of less than 3.5 nm, labeled as Time (D < 3.5 nm), is also reported in Table 5.1, rounded to the nearest nanosecond. This distance of 3.5 nm reasonable captures when the GNF starts strongly interacting with the bilayer, as the GNF at this distance has either begun to insert in the bilayer or is lying flat upon the bilayer surface. Table 5.1 demonstrates that, despite all simulations starting from the same basic configuration, the time it takes for a GNF to start strongly interacting with the bilayer increases with

ssDNA density; this further supports the idea of reduced GNF-ssDNA hydrophobicity as ssDNA density increases (i.e., SASA of the GNF decreases), since the GNF, on average, spends more time dispersed in the water. In general, there is no significant extraction of lipids at the end of the simulation time, although for systems that first adopt a flat configuration before insertion, a small amount of lipid extraction occurs during the intermediate configurations prior to insertion (as shown in Figure 5.2 for a bare GNF).

Table 5.1: Summary of simulations performed with ssDNA coating. Center-of-mass separation, D, is calculated from the last 10 ns of simulation data, representing the mean and standard deviation. The time for the GNF to insert to a depth less than 3.5 nm, Time (D < 3.5), and total simulation time are both truncated to the nearest nanosecond. The area occupied by the ssDNA at the 1 ns (initial) and the final snapshot are also reported

ssDNA coating	Trial	D (nm)	Time (D<3.5 nm)	Total Simulation Time (ns)	ssDNA area, initial : final (nm^2)	Insert/Flat
2-chains	run1	0.58 (0.07)	6	100	15.6 : 13.9	Insert
2-chains	run2	0.91 (0.08)	43	133	21.1 : 19.9	Insert
2-chains	run3	0.95 (0.07)	13	168	17.4 : 15.9	Flat, Insert at ~100 ns
2-chains	run4	0.68 (0.06)	10	100	20.3 : 13.5	Insert
2-chains	run5	0.75 (0.11)	19	168	18.6 : 11.0	Insert
2-chains	run6	0.53 (0.10)	12	100	24.7 : 14.2	Insert
4-chains	run1	2.20 (0.08)	90	182	39.6 : 38.4	Insert
4-chains	run2	2.85 (0.10)	30	318	49.6 : 47.2	Flat
4-chains	run3	1.95 (0.14)	56	250	53.6 : 36.7	Flat, Insert at ~160 ns
4-chains	run4	3.20 (0.07)	36	269	43.3 : 44.8	Flat
4-chains	run5	1.93 (0.08)	30	134	57.4 : 23.1	Insert
4-chains	run6	1.36 (0.09)	10	134	46.1 : 23.9	Insert
6-chains	run1	3.11 (0.08)	49	180	60.9 : 59.2	Flat
6-chains	run2	2.70 (0.07)	313	400	70.2 : 46.1	Insert
6-chains	run3	3.21 (0.06)	68	492	58.0 : 57.1	Flat
6-chains	run4	3.06 (0.09)	276	508	73.7 : 57.4	Flat
6-chains	run5	3.01 (0.09)	127	493	68.8 : 62.3	Flat
6-chains	run6	2.44 (0.08)	179	303	59.1 : 52.4	Insert
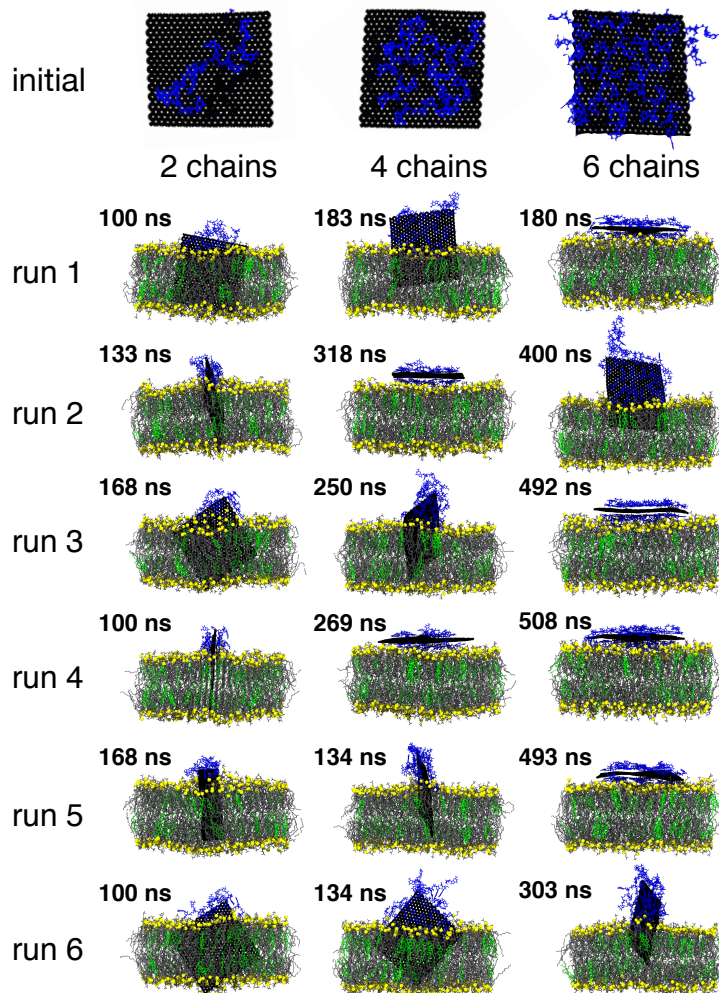
Figure 5.4: Visualization of a representative initial configuration of the ssDNA coated GNF and the final simulation snapshot for each of the 18 independent simulations; the color scheme is consistent with prior figure (see Figure 5.1) with ssDNA uniformly colored blue. Water is not shown for clarity; simulations are rendered such that the GNF is positioned in the center of the simulation cell.

More specifically, considering the case of the lowest ssDNA coating (2 ssDNA, 1 per side) where the GNF inserts into the bilayer in all six independent simulations, the general insertion behavior closely matches that of the bare, uncoated GNFs, discussed above. Five of the six independent simulations conducted directly insert into the bilayer, corner first, where the GNF is roughly parallel to the bilayer normal (similar to Figure 5.1). A single case initially adopts a flat configuration (run 3), before eventually inserting after ∼100 ns, with a mechanism that appears the same as in Figure 5.2 (i.e., temporary extraction of a

small number of lipids, followed by the GNF increasing its tilt and inserting corner first). The center-of-mass separation, D, varies from 0.53 nm to 0.95 nm between runs, which appears related to the location of the ssDNA on the GNF and the orientation of the GNF (e.g., corner vs. edge conformations, see Figure 5.4). Increasing the coating density (4 ssDNA), the GNF inserted into the bilayer in four of the six independent simulations. In three cases the GNF inserts directly, corner first and roughly normal to the bilayer, similar to Figure 5.1. A single case (run 3) first adopts a flat configuration before reorienting and inserting into the bilayer, similar to Figure 5.2. The increased ssDNA density further reduces the insertion, where center-of-mass separation, D, ranges from 1.36 to 2.20 nm for inserted GNFs, where again, variability between runs appears to be associated with the arrangement of the ssDNA on the GNF and GNF orientations (see Figure 5.4). In the remaining two simulations, GNFs adopt flat configurations and do not insert over the timescale of the simulations considered (318 ns and 269 ns for runs 2 and 4, respectively). It is possible that insertion may occur in these two cases if the simulation time were extended, given that run 3 was also seen to insert from a flat configuration. However, the shielding of the water-GNF interactions by the ssDNA likely mitigates some of the driving force associated with the lipid extraction, which appears to precede the start of the GNF insertion.

Further increasing the ssDNA density (6 ssDNA) results in different behavior being observed. Four of the six cases adopt flat configurations and do not insert over insert over the simulation times considered (180, 492, 508, and 493 ns for runs 1, 3, 4, and 5, respectively), suggesting the ssDNA at this density strongly shields the GNF, removing much of the driving force for insertion and lipid extraction that appears to precede insertion for flat configurations. The other two cases (runs 2 and 6) do not insert into the bilayer; however, the process appears much slower than for the lower density cases and follows a slightly different mechanism. Specifically, Figure 5.5g plots the insertion of the GNF into the bilayer (run 2 in Table 5.1); the GNF first interacts with the bilayer sheet in a corner-first configuration, with the corner residing within the head group region without

any appreciable insertion for nearly 200 ns (between ∼75-275 ns), after which the GNF begins to insert (Figure 5.5a-f). At the end of the simulation (400 ns, see Figure 5.5f), portions of the ssDNA appear to dangle off the side of the GNF as a result of the insertion (area occupied by the ssDNA is reduced from 70.6 to 46.1 nm^2), since the amount of free space on the GNF for which the ssDNA can be compressed is comparatively lower due to the increased number of ssDNA, thus requiring more amount of shedding to enable this insertion amount; note, since parts of the ssDNA are hydrophilic, this would not necessarily be an unfavorable configuration for the system, assuming that the GNF itself remains fully shielded from the water, as discussed in more detail below. Similarly, for the run 6, insertion of the GNF only begins after ∼100 ns of simulation time, requiring an additional ∼125 ns for the GNF to reach its final depth (see Appendix C).

The trends as a function of coating density can be rationalized by considering the driving force for bilayer penetration. The ssDNA coating provides a hydrophobic shielding similar to lipid shielding following GNF's membrane insertion or lipid extraction, since the $\pi - \pi$ stacking allows the hydrophobic bases of ssDNA to lie flat on the GNF surface, while the sugar-phosphate backbone favorably interacts with water. As such, instead of ssDNA desorption from the GNF, in general, the ssDNA is compacted on the sheet during insertion, owing to the ability of ssDNA to freely rotate and translate on the GNF surface. The adsorbed DNA prevents the GNF from inserting into the bilayer until the ssDNA moves away from the bilayer interface and locally rearranges into a denser packing on the GNF. This process appears to occur on a longer timescale than bare GNF entry into the bilayer, hence the increased timescales as coating density increases. As such, ssDNA translation appears to be the rate determining step after insertion starts, since more ssDNA must translate and compress in the more densely coated systems and must do so in a concerted manner, slowing the dynamics of the process. The Appendix C presents additional information about the potential energies of the various simulations, comparing energies of flat and inserted configurations.
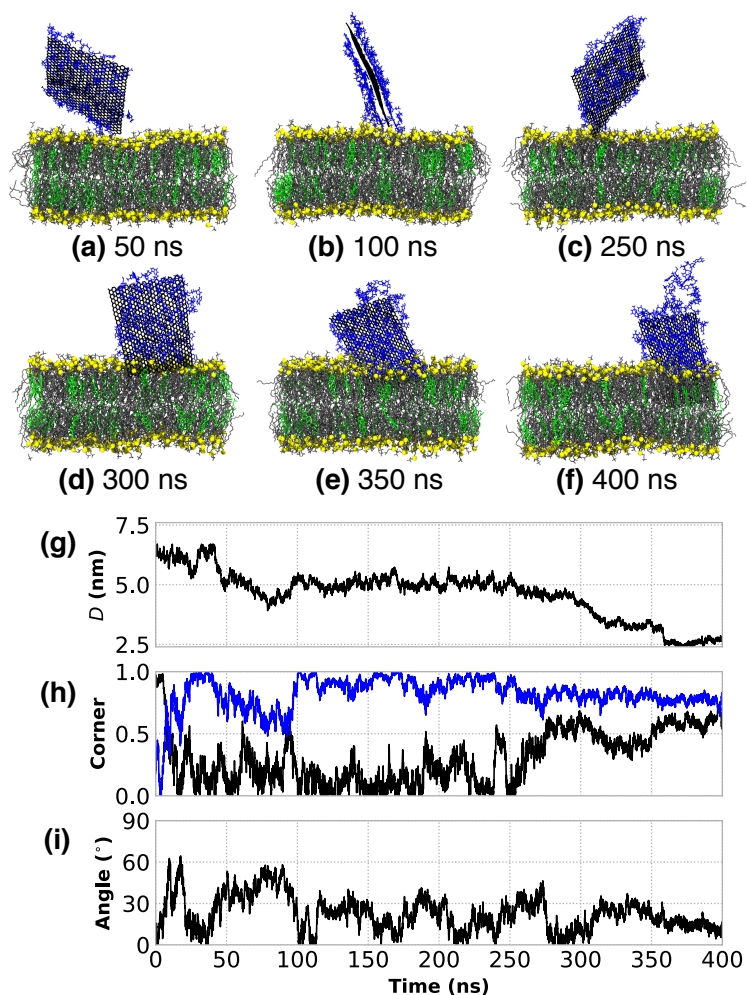
Figure 5.5: (a-f) Visualization of the insertion process of "run2" (see Table 5.1) for a GNF coated with 6 ssDNA. (g) The distance between the centers-of-mass of the GNF and bilayer, projected along the bilayer normal, where the GNF sits at the interface for ∼75-275 ns, and the eventual insertion at ∼300 ns. (h) The normalized dot product calculated between the vectors describing the GNF diagonals (black and blue) and the bilayer normal, capturing the corner first orientation of the GNF during the time it sits at the interface (∼75-275ns), and the transition to a more edge first configuration after insertion at ∼300 ns (i.e., the convergence of the value of the two diagonals). (i) The angle between the GNF and bilayer normal.

5.3.4 Steered simulations

To further examine the insertion behavior, steered MD simulations are performed in which the GNF is pulled from the solution into the middle of the bilayer using a harmonic

99

spring. Note, in all cases, the GNF is oriented "corner first" and perpendicular to the bilayer interface (insertion angle of 0°), consistent with the preferred insertion of the free (i.e., non-steered) simulations previously performed and the observations made in prior studies.[16,21,23] To further support the use of a 0°() insertion angle, the relative work required to insert a bare GNF as a function of insertion angle is reported in Table 5.2, where an angle of 0° was observed to require the least amount of work. Table 5.3 summarizes the center-of-mass separation, D, average D, are occupied by the ssDNA (using the same procedure or the free simulations), and relative work to insert the GNF to the final penetration depth (i.e., relative to the work to insert a bare GNF to its final penetration depth). The center-of-mass separations are seen to increase as the ssDNA coating increases (i.e., reduced penetration), consistent with the free simulations discussed above (see Table 5.1). The average D for the GNFs in the steered simulations closely matches the average value of the GNFs that insert in the free simulations, as reported in Table 5.3. The area on the GNF occupied by the ssDNA is also reported in Table 5.3, where good agreement is observed between free and steered simulations (note, the average values of the area occupied by the ssDNA for the free simulations only includes the systems where insertion was observed); for the 6 ssDNA case, the steered simulations, on average, have a slightly higher occupied area, likely because the steered simulations insert less (i.e., larger value of D); longer timescales that allow the ssDNA to translate/compact on the GNF would likely be required to increase insertion. As shown in Table 5.3, the relative work of insertion increases with ssDNA coating density, resulting from compaction of the ssDNA on the surface, although the relative work increase does not appear to scale linearly with the ssDNA density. The increased work to insert as ssDNA density increases is consistent with the increased timescales and reduced likelihood of insertion seen in the free simulations as coating density increases. Since the GNFs that first lie flat at the bilayer interface enter the bilayer at an angle much greater than 0°, for the cases where insertion is observed (e.g., the insertion of the bare GNF in Figure 5.2 starts when the GNF is ~60°), we could expect the relative work required for the insertion of

coated GNFs that first lie flat to be further increased beyond the values in Table 5.3. This may explain why, for example, we did not observe insertion in any of the cases where the GNFs adopted a flat configuration for the 6 ssDNA systems (i.e., runs 1 and 3-5). Note, the above work uses a spring constant of 50 kJ mol^{-1} nm^{-2}). Stronger spring constants to steer the GNF were also considered (specifically, 125, 250, and 500 kJ mol^{-1} nm^{-2}), however these resulted in increased penetration and the gradual shedding of some of the ssDNA from the GNF, and thus were not consistent with the free simulations; simulation snapshots for each of the coating densities as a function of spring constant are included in the Appendix C. However, we note that the increased insertion and shedding observed as the spring constant was increased (i.e., additional work applied to insert the GNF) further supports the prior observation that the ssDNA-GNF interactions are stronger than the hydrophobic driving force for insertion; significant ssDNA shedding is only observed when additional work is applied to the system.

Table 5.2: Relative work to insert a bare, corner GNF as a function of the angle of insertion; the relative work is the ratio of the work between a given angle and a corner-first insertion at 0°

Angle (°)	Relative work
0	1
15	1.11 (0.16)
30	1.15 (0.12)
45	1.47 (0.10)

The consistency between the free and steered simulations (with a spring constant of 50 kJ mol^{-1} nm^{-2}) suggests that steered simulations can serve as a means of rapidly screening different GNF coatings, as each of the steered simulations required only 5 ns of simulation time, as compared to the upwards of 500 ns for some of the free simulations. Based on the results presented herein, steered simulations that result in high values of D (i.e., reduced insertion) would be less likely to insert into the membranes. Similarly, given that the 6

ssDNA systems show a significantly reduced likelihood of membrane insertion, identifying coatings where the relative work exceeds the work associated with 6 ssDNA($\sim$3, see Table 5.3) could additionally identify biological coatings that could potentially prevent membrane insertion and disruption.

Table 5.3: Summary of steered simulations performed with ssDNA coating compared to steered MD. Center-of-mass separation, D, for the free simulations is calculated from the last 10 ns of simulation data for runs that insert, representing the mean and standard deviation. For the steered MD simulations, D is calculated after 5 ns of simulation time. Area of the GNF occupied by the ssDNA at the end of the simulation is also presented for the free and steered simulations. The relative work is calculated from the steered MD simulations, where the work required for a coated GNF to reach its final insertion depth is scaled by the work of a bare GNF to reach its final penetration depth

ssDNA coating	Free, D (nm)	Steered, D (nm)	Free, final ssDNA SASA (nm^2)	Steered, final ssDNA SASA (nm^2)	Relative work increase
2-chains	0.73 (0.20)	0.65 (0.17)	14.7 (3.0)	18.6 (2.3)	1.73 (0.26)
4-chains	1.86 (0.20)	1.80 (0.26)	30.5 (8.1)	36.4 (4.8)	2.95 (0.24)
6-chains	2.57 (0.11)	2.81 (0.18)	54.2 (11.4)	69.0 (4.5)	3.28 (0.25)

5.4 Conclusions

The interactions between bare and coated graphene nanoflakes (GNFs) and membranes have been examined, demonstrating how the surface adsorption of single-stranded DNA (ssDNA) molecules modulates GNF's interaction with a lipid membrane. Specifically, MD simulations show that small GNFs penetrate phospholipid/cholesterol bilayers, typically with a corner of the sheet first entering the bilayer, while the sheet surface is oriented

approximately perpendicular to the bilayer plane. Examination of small, bare GNFs of the same dimensions as the bilayer height showed no significant disruption of the biayer. Examination of a larger GNF that protrudes from the bilayer showed lipids almost immediately migrate to coat the exposed hydrophobic graphene surface and shield it from water. Disproportionately more phospholipids left the bilayer than cholesterol molecules, likely due to cholesterol's less hydrophilic lipid head group and deeper position within the bilayer. Coating the GNF with short ssDNA chains (10 repeat units) was shown to attenuate the hydrophobic interaction of the GNF with water. In general, the hydrophobic interaction driving the GNF into the bilayer was insufficient to expel the ssDNA from the surface due to strong non-covalent binding (hydrophobic and $\pi - \pi$ stacking) of nucleobases to the honeycomb lattice of the graphene surface. As the sheet sinks into the bilayer, the ssDNA molecules are pushed closer together on the protruded portion of the GNF. The surface area occupied by the compressed ssDNA molecules was found to dictate the final penetration depth of the GNF. As the ssDNA coating density increased, the timescale of GNF insertion into the lipid bilayer increased and the likelihood of insertion decreased. The steered MD simulations reaffirmed that the ssDNA coating reduces the GNF's ability to penetrate the bilayer by increasing the work required for membrane insertion.

Together, these results demonstrate a possible biocompatibility mechanism of biomolecular coatings on GNFs. By providing hydrophobic screening, the coating acts as a surfactant and reduces the driving force for penetration of the cell membrane by GNFs, which is a source of cytotoxicity of graphene.[15,16] However, one must keep in mind that the relative interaction strengths of the coating and cell membrane with the GNF are important, and that the coating chemistry will play a large role in these interactions. Here, we have shown that 10-mer oligonucleotides composed of strictly guanosine repeat units provide an adequate coverage to minimize de-coating. The coating strength my change with different nucleotides and length as different nucleobases have different interaction strengths with graphene.[24–27] Moreover, the coating density on a GNF should be expected to play an

important role in the relative interactions of the coating and cell membrane with graphene. As shown for the most densely coated GNF here, it is possible to prevent GNF penetration into a lipid bilayer via a dense ssDNA coating in some cases. It has been reported that pristine graphene can lie flat on a cell membrane and cut off large areas of the membrane surface, causing complete loss of membrane integrity.[16] Notably, however, for the most densely coated GNF, which lies flat on the bilayer surface, our studies indicate no lipids were extracted from the bilayer in simulations in excess of 500 ns, and thus the effect of this interaction on a cell membrane is unknown. In fact, generally no lipids were extracted from the bilayer in any of the coated simulations, likely because the minimal amounts of bare graphene protruded into the aqueous phase in any of the systems.

5.5   Bibliography

[1] K. S. Novoselov et al. "Electric Field Effect in Atomically Thin Carbon Films". In: *Science* 306.5696 (2004), pp. 37–66. arXiv: 0410550 `[cond-mat]`.

[2] Andrea C Ferrari et al. "Science and technology roadmap for graphene, related two-dimensional crystals, and hybrid systems". In: *Nanoscale* 7.11 (2015), pp. 4598–4810.

[3] Baomei Zhang, Yang Wang, and Guangxi Zhai. "Biomedical applications of the graphene-based materials". In: *Materials Science and Engineering: C* 61 (2016), pp. 953–964.

[4] Vanesa C Sanchez et al. "Biological interactions of graphene-family nanomaterials: an interdisciplinary review". In: *Chemical Research in Toxicology* 25.1 (2012), pp. 15–34.

[5] Yeonju Lee and Kurt E Geckeler. "Carbon nanotubes in the biological interphase: the relevance of noncovalence". In: *Advanced Materials* 22.36 (2010), pp. 4076–4083.

[6] Xiaoming Sun et al. "Nano-graphene oxide for cellular imaging and drug delivery". In: *Nano Research* 1.3 (2008), pp. 203–212. arXiv: 0808.3396.

[7] Junlang Chen et al. "Encapsulation and Release of Drug Molecule Pregabalin Based on Ultrashort Single-Walled Carbon Nanotubes". In: *The Journal of Physical Chemistry C* (2019).

[8] He Shen et al. "Biomedical applications of graphene". In: *Theranostics* 2.3 (2012), pp. 283–294.

[9] Yuqi Yang et al. "Graphene based materials for biomedical applications". In: *Materials Today* 16.10 (2013), pp. 365–373.

[10] Hongqian Bao et al. "Chitosan-functionalized graphene oxide as a nanocarrier for drug and gene delivery". In: *Small* 7.11 (2011), pp. 1569–1578.

[11] Jingquan Liu et al. "Molecularly engineered graphene surfaces for sensing applications: A review". In: *Analytica Chimica Acta* 859 (2015), pp. 1–19.

[12] Kristina E. Kitko et al. "Membrane cholesterol mediates the cellular effects of monolayer graphene substrates". In: *Nature Communications* 9.1 (2018).

[13] Yongbin Zhang et al. "Cytotoxicity Effects of Graphene and Single-Wall Carbon Nanotubes in Neural Phaeochromocytoma-Derived PC12 Cells". In: *ACS Nano* 4.6 (2010), pp. 3181–3186.

[14] Shaobin Liu et al. "Antibacterial Activity of Graphite, Graphite Oxide, Graphene Oxide, and Reduced Graphene Oxide: Membrane and Oxidative Stress". In: *ACS Nano* 5.9 (2011), pp. 6971–6980.

[15] Omid Akhavan and Elham Ghaderi. "Toxicity of graphene and graphene oxide nanowalls against bacteria". In: *ACS Nano* 4.10 (2010), pp. 5731–5736.

[16] Yusong Tu et al. "Destructive extraction of phospholipids from Escherichia coli membranes by graphene nanosheets". In: *Nature Nanotechnology* 8.8 (2013), pp. 594–601.

[17] Kristina E. Kitko et al. "Regulation of Lipid Membrane Trafficking and Transmembrane Signaling by Graphene". In: *Biophysical Journal* 108.2 (2015), 187a.

[18] Patrick S. Redmill and Clare McCabe. "Molecular dynamics study of the behavior of selected nanoscale building blocks in a gel-phase lipid bilayer". In: *Journal of Physical Chemistry B* 114.28 (2010), pp. 9165–9172.

[19] Steven L. Fiedler and Angela Violi. "Simulation of nanoparticle permeation through a lipid membrane". In: *Biophysical Journal* 99.1 (2010), pp. 144–152.

[20] Yinfeng Li et al. "Graphene microsheets enter cells through spontaneous membrane penetration at edge asperities and corner sites". In: *Proceedings of the National Academy of Sciences* 110.30 (2013), pp. 12295–12300.

[21] Liuyang Zhang, Bingqian Xu, and Xianqiao Wang. "Cholesterol Extraction from Cell Membrane by Graphene Nanosheets: A Computational Study". In: *The Journal of Physical Chemistry B* 120.5 (2016), pp. 957–964.

[22] Raul Santiago and Ramon Reigada. "Interaction modes between nanosized graphene flakes and liposomes: Adsorption, insertion and membrane fusion". In: *Biochimica et Biophysica Acta - General Subjects* 1863.4 (2019), pp. 723–731.

[23] Junlang Chen et al. "Interaction of Graphene and its Oxide with Lipid Membrane: A Molecular Dynamics Simulation Study". In: *The Journal of Physical Chemistry C* 120.11 (2016), pp. 6225–6231.

[24] S Gowtham et al. "Physisorption of nucleobases on graphene: Density-functional calculations". In: *Physical Review B* 76.3 (2007), p. 33401.

[25] Jens Antony and Stefan Grimme. "Structures and interaction energies of stacked graphene-nucleobase complexes". In: *Physical Chemistry Chemical Physics* 10 (2008), pp. 2722–2729.

[26] Neenu Varghese et al. "Binding of DNA Nucleobases and Nucleosides with Graphene". In: *ChemPhysChem* 10.1 (2009), pp. 206–210.

[27] Deivasigamani Umadevi and G Narahari Sastry. "Quantum mechanical study of physisorption of nucleobases on carbon materials: graphene versus carbon nanotubes". In: *The Journal of Physical Chemistry Letters* 2.13 (2011), pp. 1572–1576.

[28] Xiongce Zhao. "Self-Assembly of DNA Segments on Graphene and Carbon Nanotube Arrays in Aqueous Solution: A Molecular Simulation Study". In: *The Journal of Physical Chemistry C* 115.14 (2011), pp. 6181–6189.

[29] Robert R Johnson et al. "Free energy landscape of a DNA-carbon nanotube hybrid using replica exchange molecular dynamics". In: *Nano Letters* 9.2 (2009), pp. 537–541.

[30] M. Kabelac et al. "Influence of a charged graphene surface on the orientation and conformation of covalently attached oligonucleotides: A molecular dynamics study". In: *Physical Chemistry Chemical Physics* 14.12 (2012), pp. 4217–4229.

[31] Arun K. Manna and Swapan K. Pati. "Theoretical understanding of single-stranded DNA assisted dispersion of graphene". In: *Journal of Materials Chemistry B* 1.1 (2013), pp. 91–100.

[32] Cécile Caoduro et al. "Carbon nanotubes as gene carriers: Focus on internalization pathways related to functionalization and properties". In: *Acta Biomaterialia* 49 (2017), pp. 36–44.

[33] Alexander D. MacKerell and Nilesh K. Banavali. "All-Atom Empirical Force Field for Nucleic Acids: II. Application to Molecular Dynamics Simulations of DNA and RNA in Solution". In: *Journal of Computational Chemistry* 21.2 (2000), pp. 105–120.

[34] Alexander D. Mackerell. "Empirical force fields for biological macromolecules: Overview and issues". In: *Journal of Computational Chemistry* 25.13 (2004), pp. 1584–1604.

[35] Jeffery B Klauda et al. "Update of the CHARMM all-atom additive force field for lipids: validation on six lipid types". In: *The Journal of Physical Chemistry B* 114.23 (2010), pp. 7830–7843.

[36] A. D. MacKerell et al. "All-Atom Empirical Potential for Molecular Modeling and Dynamics Studies of Proteins". In: *The Journal of Physical Chemistry B* 102.18 (1998), pp. 3586–3616. arXiv: NIHMS150003.

[37] Alexander D. MacKerell, Joanna Wiórkiewicz-Kuczera, and Martin Karplus. "An All-Atom Empirical Energy Function for the Simulation of Nucleic Acids". In: *Journal of the American Chemical Society* 117.48 (1995), pp. 11946–11975.

[38] B R Brooks et al. "CHARMM: The biomolecular simulation program". In: *Journal of Computational Chemistry* 30.10 (2009), pp. 1545–1614.

[39] Sunhwan Jo, Taehoon Kim, and Wonpil Im. "Automated builder and database of protein/membrane complexes for molecular dynamics simulations". In: *PloS One* 2.9 (2007), e880.

[40] Sunhwan; Jo et al. "CHARMM-GUI: A Web-Based Graphical User Interface for CHARMM". In: *Journal of computational chemistry* 29 (2008), pp. 1859–1865. arXiv: NIHMS150003.

[41] Sunhwan Jo et al. "CHARMM-GUI Membrane Builder for Mixed Bilayers and Its Application to Yeast Membranes". In: *Biophysical Journal* 97.1 (2009), pp. 50–58.

[42] Emilia L Wu et al. "CHARMM-GUI Membrane Builder toward realistic biological membrane simulations". In: *Journal of Computational Chemistry* 35.27 (2014), pp. 1997–2004.

[43] Jumin Lee et al. "CHARMM-GUI Input Generator for NAMD, GROMACS, AMBER, OpenMM, and CHARMM/OpenMM Simulations Using the CHARMM36 Additive Force Field". In: *Journal of Chemical Theory and Computation* 12.1 (2016), pp. 405–413.

[44] William Humphrey, Andrew Dalke, and Klaus Schulten. "VMD: Visual Molecular Dynamics". In: *Journal of molecular graphics* 14 (1996), pp. 33–38. arXiv: arXiv: 1503.05249v1.

[45] Jannik C Meyer et al. "The structure of suspended graphene sheets". In: *Nature* 446.7131 (2007), pp. 60–63.

[46] Nai Gui Shang et al. "Catalyst-free efficient growth, orientation and biosensing properties of multilayer graphene nanoflake films with sharp edge planes". In: *Advanced Functional Materials* 18.21 (2008), pp. 3506–3514.

[47] James Stroud. *make-na server*. 2004.

[48] Thomas J Macke and David A Case. "Modeling Unusual Nucleic Acid Structures". In: *Molecular Modeling of Nucleic Acids*. 1997. Chap. 24, pp. 379–393.

[49] Enzo Marinari and Giorgio Parisi. "Simulated Tempering: A New Monte Carlo Scheme". In: (1992). arXiv: 9205018 [hep-lat].

[50] H J C Berendsen, D van der Spoel, and R van Drunen. "GROMACS: A message-passing parallel molecular dynamics implementation". In: *Computer Physics Communications* 91.1 (1995), pp. 43–56.

[51] David Van Der Spoel et al. "GROMACS: Fast, flexible, and free". In: *Journal of Computational Chemistry* 26.16 (2005), pp. 1701–1718.

[52] Berk Hess et al. "GROMACS 4: Algorithms for Highly Efficient, Load-Balanced, and Scalable Molecular Simulation". In: *Journal of Chemical Theory and Computation* 4.3 (2008), pp. 435–447.

[53] Sander Pronk et al. "GROMACS 4.5: a high-throughput and highly parallel open source molecular simulation toolkit". In: *Bioinformatics* 29.7 (2013), p. 845.

[54] Mark James Abraham et al. "GROMACS: High performance molecular simulations through multi-level parallelism from laptops to supercomputers". In: *SoftwareX* 1-2 (2015), pp. 19–25.

[55] Szilárd Páll et al. "Tackling Exascale Software Challenges in Molecular Dynamics Simulations with GROMACS". In: *Solving Software Challenges for Exascale: International Conference on Exascale Applications and Software, EASC 2014, Stockholm, Sweden, April 2-3, 2014, Revised Selected Papers*. Ed. by Stefano Markidis and Erwin Laure. Cham: Springer International Publishing, 2015, pp. 3–27.

[56] Ulrich Essmann et al. "A smooth particle mesh Ewald method". In: *The Journal of Chemical Physics* 103 (1995), pp. 8577–8593.

[57] Shuichi Nosé. "A unified formulation of the constant temperature molecular dynamics methods". In: *The Journal of Chemical Physics* 81.1 (1984), pp. 511–519. arXiv: 9807099 [cond-mat].

[58] William G Hoover. "Canonical dynamics: Equilibrium phase-space distributions". In: *Phys. Rev. A* 31.3 (1985), pp. 1695–1697.

[59] M. Parrinello and A. Rahman. "Polymorphic transitions in single crystals: A new molecular dynamics method". In: *Journal of Applied Physics* 52.12 (1981), pp. 7182–7190. arXiv: arXiv:1011.1669v3.

[60] William L. Jorgensen et al. "Comparison of simple potential functions for simulating liquid water". In: *The Journal of Chemical Physics* 79.2 (1983), pp. 926–935. arXiv: arXiv:1011.1669v3.

[61] Simone Conti et al. "Perchlorination of Coronene Enhances its Propensity for Self-Assembly on Graphene". In: *ChemPhysChem* 17.3 (2016), pp. 352–357.

[62] Kenno Vanommeslaeghe et al. "CHARMM general force field: A force field for drug-like molecules compatible with the CHARMM all-atom additive biological force fields". In: *Journal of Computational Chemistry* 31.4 (2010), pp. 671–690.

[63] Nicolas Foloppe and Alexander D. MacKerell. "All-Atom Empirical Force Field for Nucleic Acids: I. Parameter Optimization Based on Small Molecule and Condensed Phase Macromolecular Target Data". In: *Journal of Computational Chemistry* 21.2 (2000), pp. 86–104.

Chapter 6

Conclusions and Future Work

Lipid bilayers are extremely prevalent materials found throughout nature and engineering. For biological barrier and separation applications, lipid bilayers are very promising due to their tunability; modifying bilayer composition can fine-tune the bilayer structure toward a particular application. Molecular simulation serves as an excellent platform to study lipid bilayer materials, especially as models and force fields become more accurate and computational hardware allows scientists to study length (10s to 100s of nanometers) and timescales (100s to 1000s of nanoseconds) appropriate for lipid bilayers.

Chapter 3 utilizes molecular simulation to examine the role of composition on the structure of lipid bilayers within the gel phase. DSPC, FFA, and OH were modeled in order to elucidate the role of head group chemistry and chain length on a variety of structural properties and lipid organization. Components were found at different depths within the bilayer depending on the chain length and head group. This phenomena influenced the ability of tails to align and order with each other, affecting lipid packing. The head groups and offset effects were also found to influence hydrogen bonding networks and interfacial solvent dynamics.

Chapter 4 explores the permeability of water through gel-phase lipid bilayers, relating permeability to structural properties, with trends that can relate back to composition relationships found in Chapter 3. In agreement with both experimental and theoretical literature, lipid packing and ordering most strongly dictate water permeability. Thus, the strongest barriers will be those with the smallest tail-tail distances and the fewest *gauche* defects.

Chapter 5 explores how external compounds like graphene and biomolecular coatings can influence fluid-phase lipid bilayers. Hydrophobic interactions drive bare graphene

away from the water phase, either by inserting into a lipid bilayer or by extracting lipids from the lipid bilayer. With biomolecular coatings like ssDNA, graphene's cytotoxicity can be mitigated while still maintaining graphene's interaction with lipid bilayers; biomolecular coatings prevent lipid extraction, but still allow graphene insertion into the bilayer. Increasing the amount of coating will reduce the need and increase the work necessary for insertion.

The results presented in this Thesis are promising, but the vastness of chemical space still requires exploration, and advances in computational hardware and methods will facilitate this progress. The Molecular Simulation and Design Framework (MoSDeF) is a promising approach to high-throughput screening of materials,[1–3] enabling a robust, organized platform to conduct many simulations in a systematic manner and explore chemical space. Especially as computational hardware advances, the limitation then becomes the ability of the scientist to fully utilize these resources. From rapidly performing thousands of simulations to implementing big data and statistical analysis, molecular simulation certainly has a big future ahead for screening new materials.

6.1   Recommendations for Future Work

6.1.1   Screening Novel Additives for Gel-Phase Phospholipids

While the properties for good barriers have been characterized, the work lies within identifying the correct combination of compounds that yields the optimum water barrier to support the SC against ailments like dry skin. Computationally, thus far, OH and FFA have been studied. Experimentally, IPIS, ISIS, and GMIS have been tested in an SC context,[4] while alkanes have been tested in some phospholipid work.[5]

It stands to reason that modeling and simulating IPIS, ISIS, and GMIS could be promising materials. While they've shown some barrier function in gel-phase ceramide mixtures, they could show similar properties in gel-phase phospholipid mixtures. One initial obsta-

cle includes developing accurate molecular models for these three compounds – reference data would be necessary to develop the force field parameters that accurately describe the physical interactions of these compounds. Another consideration is the reports of these molecules not incorporating into the SC, and instead forming their own lamella. This issue requires studying the phase separation of these molecules and developing the correct simulation protocols to equilibrate these more complex mixtures. Furthermore, such length and timescales may be prohibitive for current atomistic levels of molecular simulation (thus requiring coarse-grained levels of simulation).

Alkanes, on the other hand, are more well-studied and parametrized. This class of compounds could be promising in that they do not possess head groups nearly as large as OH or FFA compounds, having a more uniform, rod-like structure as opposed to mild inverted-conical structures of OH and FFA.

Besides inverted-cone or rod-like structures, cone-like structures could be novel additions to lipid bilayers. This Thesis and Tardieu *et al.* observed a liquid-like, disordered region in the middle of the gel-phase bilayer, arising due to length heterogeneity.[6] Using cone-like structures would introduce narrow components into the already-dense tail region, not disturbing the tail packing, but could introduce bulkier groups that would enforce order and rigidity in the middle of the bilayer. This would involve first identifying cone-like molecules that would stably incorporate into gel-phase lipid bilayers, developing force field parameters for these molecules, and adequately equilibrating them.

While DSPC was chosen as the base material to form gel-phase bilayers, there are still many other compounds with different head groups and tail groups that could alter barrier properties. Notably, this Thesis reported the relevance of head group chemistry on barrier properties, but only by altering the secondary and tertiary single-tailed components. Work is needed to identify how head and tail chemistry of the two-tailed lipid can influence structure and barrier properties (e.g., packing, hydrogen bonding, water dynamics, permeability). Similar work as other proposed components is necessary – developing force field

parameters and proper equilibration protocols.

Beyond these proposed components, more diverse mixtures could be simulated to study the complex network of composition, structure, and permeability, increasing the possible dimensionality and degrees of freedom for these interactions. While studying systems of four or more components sounds interesting, the issue lies in building a sufficiently-large bilayer that sufficiently represents a physically-real four-component mixture and does not suffer from finite size artifacts.

When studying more diverse mixtures, the degree of heterogeneity is likely to increase, as observed in early SC work that demonstrated the formation of various domains.[4,7] While domains were not observed in these simulations of two- and three-component mixtures, larger mixtures could form domains and introduce new permeation pathways and mechanisms.[8] The possibility of alternative permeability mechanisms can be seen in the Appendix to Chapter 4, as the experimental permeability values show varying levels of relation with simulated structural, simulated permeability, and experimental permeability values. Furthermore, the somewhat-weak correlation between experimental structure and experimental permeability could indicate that experimental structural metrics are insufficient observables to characterize permeability. For example, phase separation or heterogeneity are not quantified, but could have an influence on experimental permeability. Again, using simulations to examine phase separation or heterogeneity would require larger simulations or alternative simulation methods.

While one can always hope for more computational resources to study more atoms, larger bilayers, and longer time scales, a variety of modeling techniques could prove useful. Among them includes coarse-graining, in which multiple atoms are represented as a single bead, reducing the number of particles to calculate, enabling larger time steps, and speeding up kinetics due to reduced degrees of freedom. Moore *et al.* have demonstrated the utility of multi-state iterative Boltzmann inversion (MSIBI) to build coarse-grained models of SC lipids.[9,10] MSIBI could be used to develop coarse-grained models and simulate larger, more

complex phospholipid mixtures.

6.1.2 Studying Phospholipid Incorporation into the SC

There has been preliminary evidence that phospholipids applied to the skin can be incorporated into the SC.[11] Rather than serving as a topical formulation that is external from the SC, phospholipid bilayers may join the SC lamella similar to earlier moisturizers.[4,7] This potential phenomenon could have application for restoring SC to proper lateral and lamellar organization.

This is a computationally-demanding task to appropriately study phospholipids and their interactions with SC lamella. A coarse-grained approach seems feasible[9,10] as outlined earlier in this section. The physical interactions of phospholipids with ceramides and cholesterol will also need to be parametrized along this vein.

6.1.3 Screening Novel Biomolecular Coatings to Mitigate Graphene Cytotoxicity

In this thesis, single-stranded DNA (ssDNA) was studied as a promising biomolecular coating to prevent lipid extraction and bilayer destruction by bare graphene. While a basic understanding of the mechanisms and relevant properties have been described, more work lies within studying other biomolecular coatings that could function "better" than ssDNA.

"Better" coatings could be those that can easily adsorb to the graphene surface or rapidly facilitate graphene insertion. Toward more engineering applications, "better" coatings could be those that are cheaper or more biocompatible.

6.1.4 Studying the Phase Behavior of Graphene-Bilayer Systems

The fundamental reason graphene was studied was its influence on cholesterol aggregation and facilitation of the liquid-ordered phase within lipid bilayers, promoting neurotransmission. More studies can be performed to study graphene's influence on phase

behavior in lipid bilayers. This is especially important as experimental methods do not provide the level of resolution to study this phenomena. Potential routes of study include identifying the mechanism by which graphene facilitates cholesterol aggregation, or how graphene helps form the liquid-ordered phase – are lipids rearranged or extracted from the membrane when graphene is introduced?

The systems examined in this Thesis could only simulate 30,000 atoms in a 10 x 10 x 13 nm box for up to hundreds of ns. Phase studies on systems of this scope will likely require more atoms, larger boxes, and longer timescales. This issue could potentially be ameliorated by enhanced sampling approaches, coarse-grained simulations, or alternative sampling approaches like Monte Carlo methods. Among all three approaches, extensive work will be necessary to validate the approach and obtain physically-realistic results.

6.2 Bibliography

[1] Christoph Klein et al. "Formalizing atom-typing and the dissemination of force fields with foyer". In: *Computational Materials Science* 167.May (2019), pp. 215–227.

[2] Christoph Klein et al. "A Hierarchical, Component Based Approach to Screening Properties of Soft Matter". In: *Foundations of Molecular Modeling and Simulation: Select Papers from FOMMS 2015*. Ed. by Randall Q Snurr, Claire S Adjiman, and David A Kofke. Singapore: Springer Singapore, 2016, pp. 79–92.

[3] Peter Cummings. "Computational screening of soft materials systems with application to nano-lubrication systems". In: (2017).

[4] Julia Caussin, Gert S. Gooris, and Joke A. Bouwstra. "FTIR studies show lipophilic moisturizers to interact with stratum corneum lipids, rendering the more densely packed". In: *Biochimica et Biophysica Acta - Biomembranes* 1778.6 (2008), pp. 1517–1524.

[5] Mafumi Hishida et al. "Effect of n-alkanes on lipid bilayers depending on headgroups". In: *Chemistry and Physics of Lipids* 188 (2015), pp. 61–67.

[6] A. Tardieu, Vittorio Luzzati, and F. C. Reman. "Structure and polymorphism of the hydrocarbon chains of lipids: A study of lecithin-water phases". In: *Journal of Molecular Biology* 75.4 (1973), pp. 711–733.

[7] J. Caussin et al. "Interaction of lipophilic moisturizers on stratum corneum lipid domains in vitro and in vivo". In: *Skin Pharmacology and Physiology* 20.4 (2007), pp. 175–186.

[8] Annalaura Del Regno and Rebecca Notman. "Permeation pathways through lateral domains in model membranes of skin lipids". In: *Physical Chemistry Chemical Physics* 20.4 (2018), pp. 2162–2174.

[9] Timothy C. Moore, Christopher R. Iacovella, and Clare McCabe. "Derivation of coarse-grained potentials via multistate iterative Boltzmann inversion". In: *Journal of Chemical Physics* 140.22 (2014). arXiv: 1410.1853.

[10] Timothy C. Moore et al. "A Coarse-Grained Model of Stratum Corneum Lipids: Free Fatty Acids and Ceramide NS (SI)". In: *Journal of Physical Chemistry B* 120.37 (2016), pp. 1–22.

[11] G. S. Gooris et al. "Interactions of dipalmitoylphosphatidylcholine with ceramide-based mixtures". In: *Biochimica et Biophysica Acta - Biomembranes* 1860.6 (2018), pp. 1272–1281. arXiv: S0005273618300658.

Appendix A

Appendix to Chapter 3

Table A.1: Area per lipid (APL), height, interdigitation (Idig), S2, and tilt values for 33% DSPC systems.

System	APL (Å^2)	Height (Å)	Idig (Å)	S2	Tilt Angle (°)
(1:2) DSPC-FFA12	26.79 (0.05)	49.79 (0.06)	3.27 (0.03)	0.9715 (0.0008)	11.2 (0.4)
(1:2) DSPC-FFA16	26.89 (0.06)	52.45 (0.11)	2.78 (0.01)	0.9801 (0.0005)	16.4 (0.5)
(1:2) DSPC-FFA24	27.18 (0.08)	60.51 (0.18)	5.98 (0.01)	0.9819 (0.0004)	18.5 (0.5)
(1:2) DSPC-OH12	25.98 (0.01)	49.95 (0.06)	3.48 (0.01)	0.9813 (0.0003)	10.0 (0.2)
(1:2) DSPC-OH16	25.41 (0.03)	54.24 (0.06)	2.02 (0.01)	0.9882 (0.0002)	9.1 (0.3)
(1:2) DSPC-OH24	26.44 (0.04)	61.23 (0.10)	6.06 (0.01)	0.9842 (0.0003)	15.0 (0.3)
(1:1:1) DSPC-OH12-FFA12	26.76 (0.03)	49.84 (0.08)	3.36 (0.06)	0.9778 (0.0006)	10.5 (0.2)
(1:1:1) DSPC-OH12-FFA16	26.42 (0.07)	51.75 (0.11)	2.66 (0.06)	0.9832 (0.0002)	13.1 (0.4)
(1:1:1) DSPC-OH12-FFA24	26.95 (0.03)	55.77 (0.09)	6.55 (0.13)	0.9753 (0.0005)	13.4 (0.2)
(1:1:1) DSPC-OH16-FFA12	26.33 (0.05)	52.21 (0.06)	2.99 (0.04)	0.9829 (0.0004)	11.1 (0.4)
(1:1:1) DSPC-OH16-FFA16	26.45 (0.10)	53.53 (0.18)	2.56 (0.04)	0.9861 (0.0004)	13.5 (0.9)
(1:1:1) DSPC-OH16-FFA24	26.38 (0.14)	57.98 (0.25)	5.23 (0.13)	0.9831 (0.0007)	14.6 (0.8)
(1:1:1) DSPC-OH24-FFA12	25.59 (0.05)	58.30 (0.07)	7.63 (0.20)	0.9775 (0.0005)	10.2 (0.5)
(1:1:1) DSPC-OH24-FFA16	27.20 (0.06)	56.73 (0.11)	5.94 (0.14)	0.9796 (0.0004)	15.0 (0.4)
(1:1:1) DSPC-OH24-FFA24	26.77 (0.08)	61.57 (0.14)	6.74 (0.12)	0.9833 (0.0004)	15.9 (0.6)

Table A.2: FFA offset, OH offset, area per tail (APT), intra-bilayer hydrogen bonding (HB), and dipole relaxation (Dip) for 33% DSPC systems.

System	FFA Offset (Å)	OH Offset (Å)	APT (Å^2)	HB x1000	Dip (ps)
(1:2) DSPC-FFA12	6.91 (0.06)		19.66 (0.03)	26.8 (2.3)	318 (10)
(1:2) DSPC-FFA16	5.60 (0.04)		19.30 (0.01)	33.0 (2.4)	325 (15)
(1:2) DSPC-FFA24	3.95 (0.06)		19.15 (0.02)	36.2 (2.2)	379 (39)
(1:2) DSPC-OH12		6.29 (0.05)	19.13 (0.01)	29.0 (2.5)	333 (10)
(1:2) DSPC-OH16		5.45 (0.04)	18.80 (0.01)	32.8 (1.7)	371 (8)
(1:2) DSPC-OH24		3.85 (0.06)	18.87 (0.01)	27.5 (2.6)	375 (18)
(1:1:1) DSPC-OH12-FFA12	6.59 (0.06)	6.56 (0.05)	19.45 (0.02)	25.9 (2.4)	326 (11)
(1:1:1) DSPC-OH12-FFA16	5.16 (0.04)	7.12 (0.05)	19.00 (0.02)	31.5 (2.4)	340 (17)
(1:1:1) DSPC-OH12-FFA24	4.75 (0.08)	7.15 (0.07)	19.23 (0.01)	30.7 (2.4)	354 (17)
(1:1:1) DSPC-OH16-FFA12	7.44 (0.06)	5.33 (0.05)	19.08 (0.01)	27.9 (2.4)	357 (8)
(1:1:1) DSPC-OH16-FFA16	5.50 (0.06)	5.69 (0.06)	18.95 (0.01)	32.3 (2.4)	355 (20)
(1:1:1) DSPC-OH16-FFA24	3.60 (0.08)	5.90 (0.04)	18.83 (0.01)	34.3 (2.4)	371 (26)
(1:1:1) DSPC-OH24-FFA12	8.41 (0.08)	4.09 (0.08)	18.67 (0.02)	32.2 (2.4)	391 (7)
(1:1:1) DSPC-OH24-FFA16	5.89 (0.06)	3.83 (0.12)	19.19 (0.01)	35.7 (2.5)	360 (15)
(1:1:1) DSPC-OH24-FFA24	4.24 (0.12)	4.09 (0.09)	18.99 (0.02)	37.3 (2.4)	377 (9)

Table A.3: Area per lipid (APL), height, interdigitation (Idig), S2, and tilt values for 50% DSPC systems.

System	APL (Å^2)	Height (Å)	Idig (Å)	S2	Tilt Angle (°)
(1:1) DSPC-FFA12	30.78 (0.04)	51.33 (0.08)	3.55 (0.07)	0.9675 (0.0009)	13.1 (0.3)
(1:1) DSPC-FFA16	30.95 (0.09)	52.66 (0.10)	3.13 (0.13)	0.9802 (0.0005)	19.5 (0.4)
(1:1) DSPC-FFA24	32.13 (0.12)	56.87 (0.18)	6.98 (0.13)	0.9631 (0.0013)	21.2 (0.6)
(1:1) DSPC-OH12	29.33 (0.05)	52.49 (0.04)	2.89 (0.08)	0.9816 (0.0002)	9.9 (0.4)
(1:1) DSPC-OH16	29.94 (0.07)	53.59 (0.11)	2.43 (0.08)	0.9828 (0.0002)	16.9 (0.5)
(1:1) DSPC-OH24	30.86 (0.06)	58.09 (0.13)	6.58 (0.10)	0.9778 (0.0006)	19.6 (0.5)
(2:1:1) DSPC-OH12-FFA12	29.99 (0.08)	51.74 (0.09)	3.44 (0.16)	0.9746 (0.0007)	13.4 (0.5)
(2:1:1) DSPC-OH12-FFA16	30.13 (0.08)	52.56 (0.14)	2.99 (0.13)	0.9780 (0.0003)	14.6 (0.6)
(2:1:1) DSPC-OH12-FFA24	30.80 (0.10)	54.88 (0.15)	5.95 (0.11)	0.9653 (0.0011)	15.6 (0.5)
(2:1:1) DSPC-OH16-FFA12	30.33 (0.08)	52.48 (0.12)	3.06 (0.01)	0.9794 (0.0007)	16.0 (0.7)
(2:1:1) DSPC-OH16-FFA16	29.93 (0.13)	53.88 (0.17)	2.76 (0.01)	0.9874 (0.0004)	16.6 (0.7)
(2:1:1) DSPC-OH16-FFA24	30.35 (0.11)	56.40 (0.21)	6.14 (0.14)	0.9781 (0.0006)	15.6 (0.7)
(2:1:1) DSPC-OH24-FFA12	29.79 (0.09)	56.43 (0.17)	7.14 (0.19)	0.9729 (0.0015)	11.2 (0.7)
(2:1:1) DSPC-OH24-FFA16	31.55 (0.08)	59.40 (0.09)	7.13 (0.09)	0.9655 (0.0015)	17.3 (0.5)
(2:1:1) DSPC-OH24-FFA24	31.12 (0.08)	58.14 (0.16)	6.50 (0.10)	0.9757 (0.0008)	20.1 (0.5)

Table A.4: FFA offset, OH offset, area per tail (APT), intra-bilayer hydrogen bonding (HB), and dipole relaxation (Dip) for 50% DSPC systems.

System	FFA Offset ($\mathring{A}$)	OH Offset ($\mathring{A}$)	APT ($\mathring{A}^2$)	HB	Dip (ps)
(1:1) DSPC-FFA12	7.90 (0.04)		19.81 (0.02)	20.5 (2.1)	313 (5)
(1:1) DSPC-FFA16	6.17 (0.06)		19.30 (0.02)	27.1 (2.0)	319 (24)
(1:1) DSPC-FFA24	4.80 (0.06)		19.79 (0.02)	31.1 (2.0)	320 (18)
(1:1) DSPC-OH12		7.23 (0.05)	19.14 (0.01)	24.4 (2.1)	333 (16)
(1:1) DSPC-OH16		7.23 (0.05)	19.14 (0.01)	27.5 (2.0)	323 (13)
(1:1) DSPC-OH24		4.29 (0.05)	19.03 (0.01)	34.1 (2.1)	342 (15)
(2:1:1) DSPC-OH12-FFA12	8.05 (0.22)	7.37 (0.07)	19.31 (0.02)	22.5 (2.0)	328 (10)
(2:1:1) DSPC-OH12-FFA16	5.87 (0.09)	7.83 (0.07)	19.28 (0.01)	26.2 (2.0)	326 (3)
(2:1:1) DSPC-OH12-FFA24	4.98 (0.14)	7.40 (0.08)	19.64 (0.02)	26.1 (1.9)	338 (11)
(2:1:1) DSPC-OH16-FFA12	8.28 (0.06)	5.79 (0.04)	19.26 (0.03)	24.7 (1.9)	321 (24)
(2:1:1) DSPC-OH16-FFA16	6.19 (0.09)	6.21 (0.05)	19.07 (0.01)	29.7 (2.3)	331 (10)
(2:1:1) DSPC-OH16-FFA24	5.63 (0.10)	6.10 (0.08)	19.36 (0.02)	27.9 (2.6)	344 (15)
(2:1:1) DSPC-OH24-FFA12	8.31 (0.09)	5.03 (0.14)	19.37 (0.01)	25.5 (2.0)	362 (11)
(2:1:1) DSPC-OH24-FFA16	6.03 (0.12)	4.87 (0.05)	19.92 (0.02)	27.7 (2.0)	336 (21)
(2:1:1) DSPC-OH24-FFA24	4.90 (0.13)	4.35 (0.09)	19.29 (0.02)	31.7 (2.1)	334 (12)

Appendix to Chapter 4
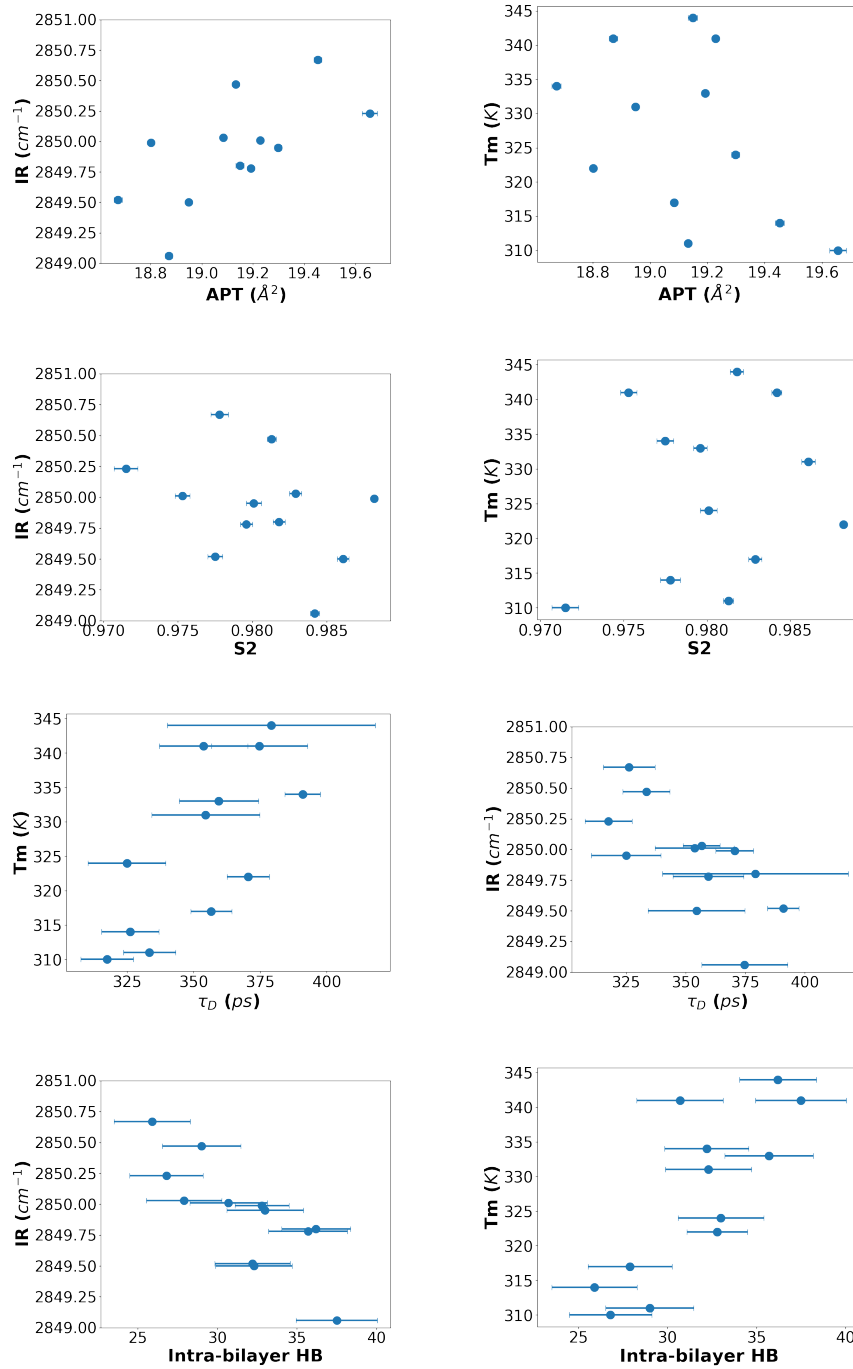
Figure B.1: Simulated structural data vs. experimental structural data. APT, S2, τ_D, and Intra-bilayer HB follow same notation as Chapter 4. Tm denotes bilayer melting point; IR denotes CH_2 symmetric stretch frequency.
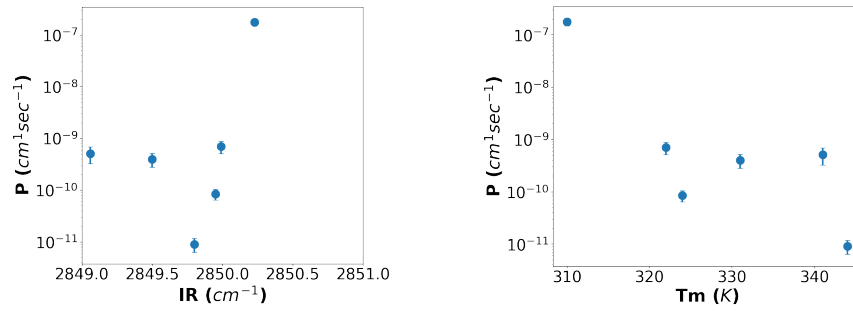
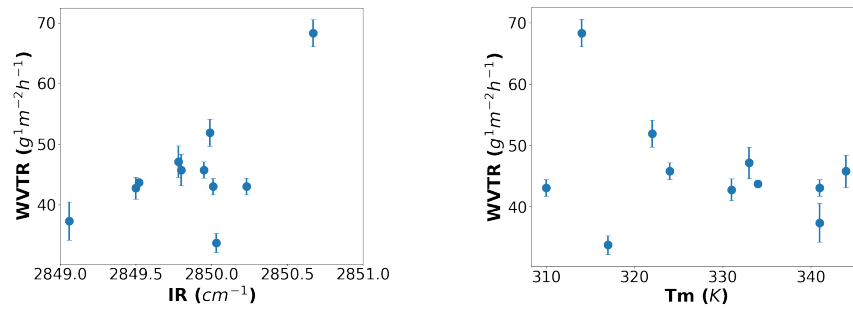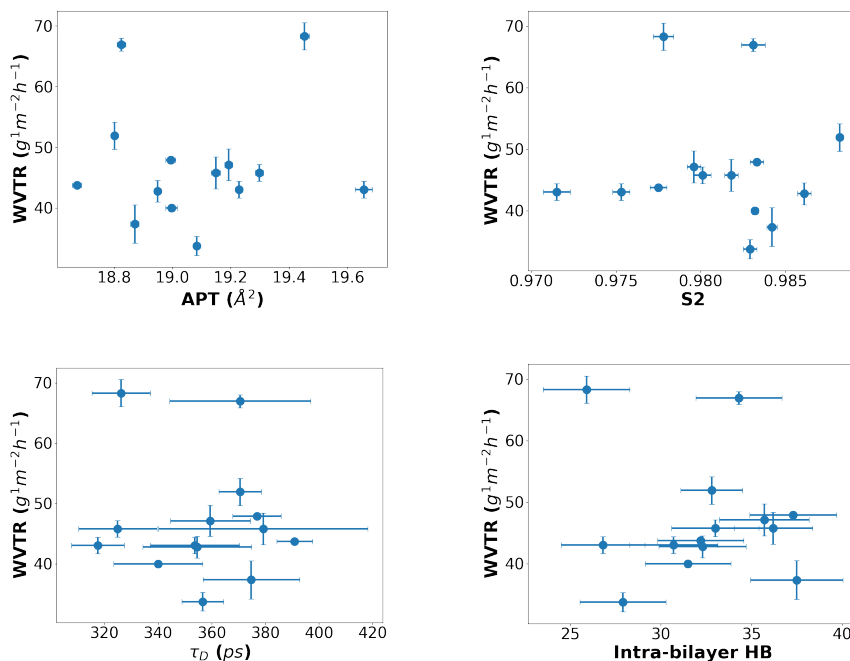Figure B.2: Experimental structural data vs. simulated permeability data. IR and Tm follow same notation as above.

Figure B.3: Experimental structural data vs. experimental permeability data. Tm and IR follow same notation as above. WVTR denotes water-vapor transmission rate.

Figure B.4: Simulated structural data vs. experimental permeability data. APT, S2, τ_D, Intra-bilayer HB, and WVTR follows same notation as above. P denotes simulated permeability coefficient.
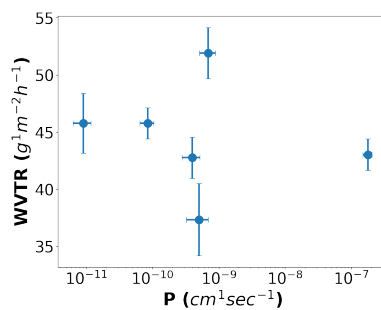
Figure B.5: Simulated permeability data vs. experimental permeability data. WVTR and P follow same notation as above. It should be noted that corresponding experimental WVTR measurements are computed from formulations containing a dilute fraction of phospholipid and OH/FFA component, thus muting the influence of composition on experimental barrier properties compared to simulations of more-concentrated systems.

Appendix C

Appendix to Chapter 5

INITIALIZATION OF GNFS WITH DNA COATING
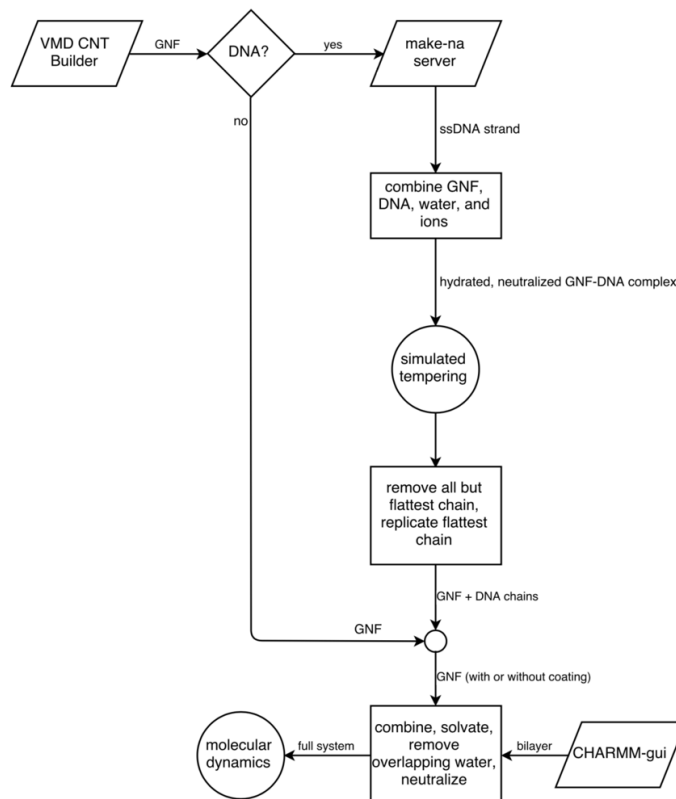
Figure C.1: Process flow for initializing and simulating the systems studied in graphene-DNA-bilayer studies. Parallelograms represent external programs used to generate structures, diamonds represent decision points, rectangles represent structure manipulation, and large circles represent simulations.
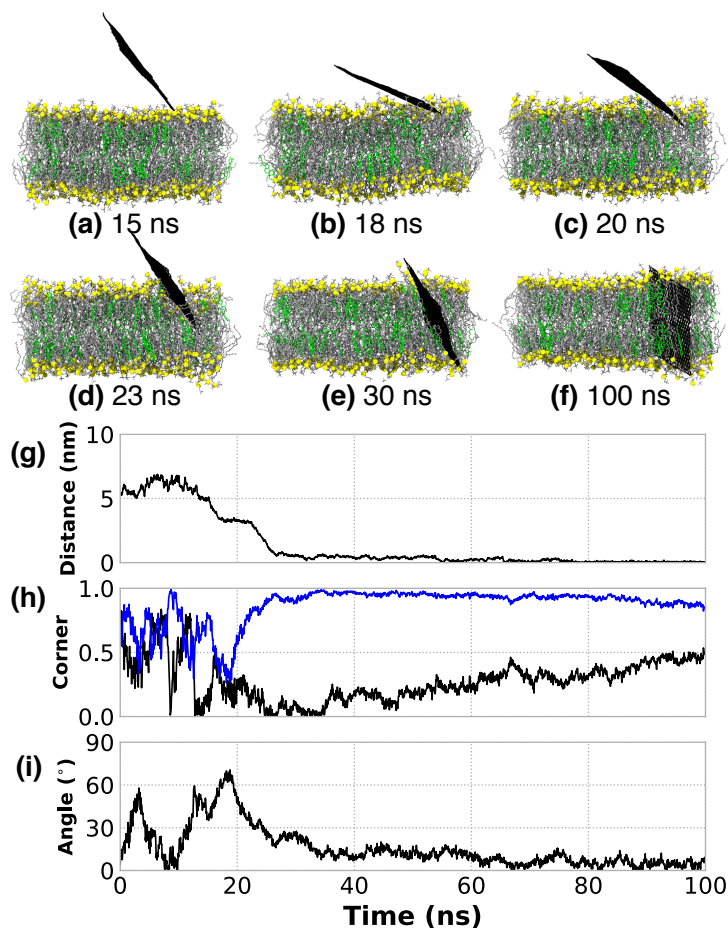
Figure C.2: Insertion of a bare GNF where the GNF initially approaches the bilayer at a non-ideal angle of insertion. (a-f) snapshots of the insertion process as a function of time. (g) The distance between the centers-of-mass of the GNF and bilayer, projected along the bilayer normal; the plateau in separation between ∼17-27 ns corresponds to the reorientation of the GNF before insertion into the bilayer. (h) The normalized dot product calculated between the vectors describing the GNF diagonals (blue and black) and the bilayer normal, demonstrating the corner first insertion at ∼27 ns. (i) The angle between the GNF and bilayer normal is plotted as a function of time, showing the reorientation of the GNF during insertion, where the value slowly achieves a value close to 0° at the end of the simulation.
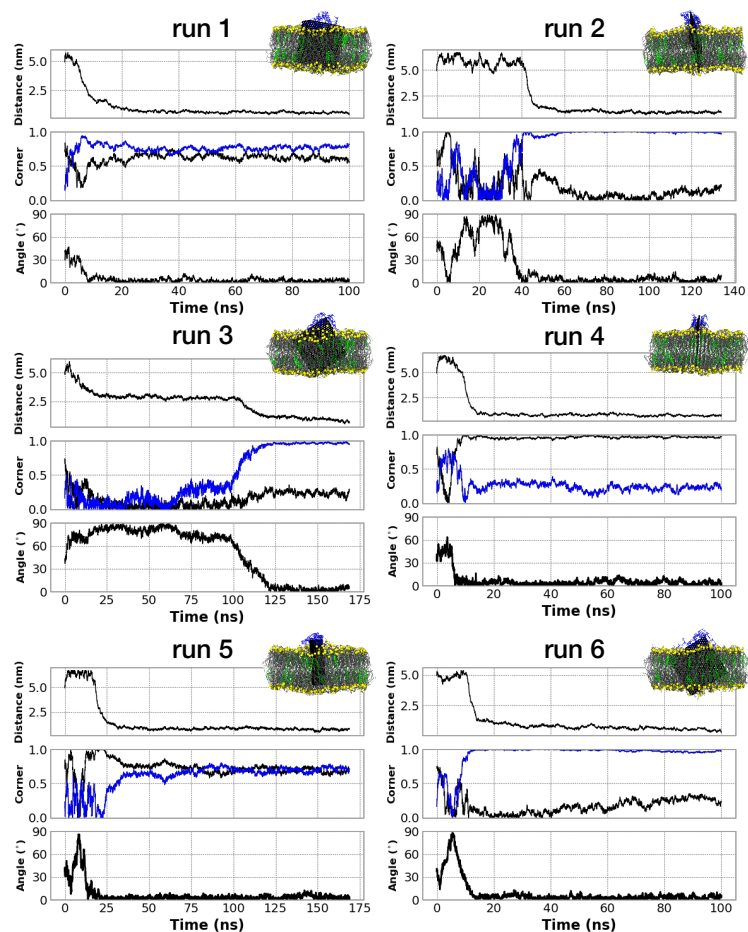
Figure C.3: Analysis of 6 replicates for the 2 ssDNA coated GNF simulations. For each replicate, the following metrics are calculated: the distance between the centers-of-mass of the GNF and bilayer projected along the bilayer normal ("Distance"); the normalized dot product calculated between the vectors describing the GNF diagonals (blue and black) and the bilayer normal, where a value of unity for one of the diagonals represents a corner first orientation ("Corner"); and angle between the GNF and bilayer normal where a value of 0° corresponds to the perpendicular orientation of the GNF sheet and a value of 90° to the GNF lying flat upon the bilayer interface ("Sheet"). A simulation snapshot corresponding to the final configuration of the simulation is inset for each replicate, where water is not shown for clarity, P atoms of DOPC are shown as yellow to highlight boundary, DOPC tails are shown as gray, and CHOL colored green, following the color scheme in Chapter 5.
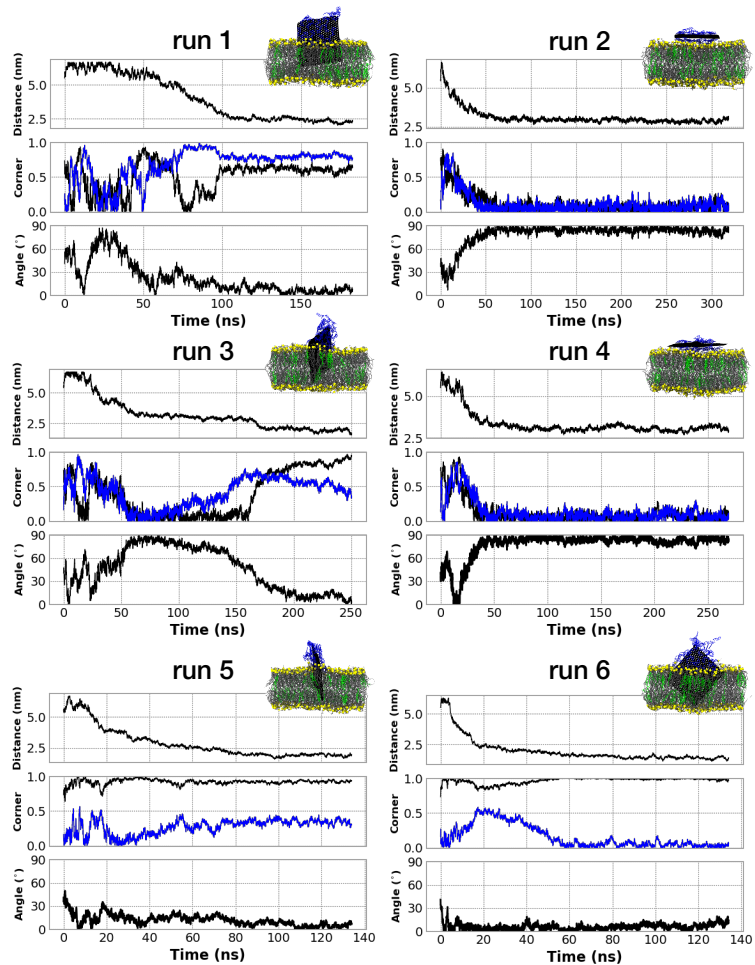
Figure C.4: Analysis of 6 replicates for the 4 ssDNA coated GNF simulations. The analysis and color scheme follows Figure C.3.
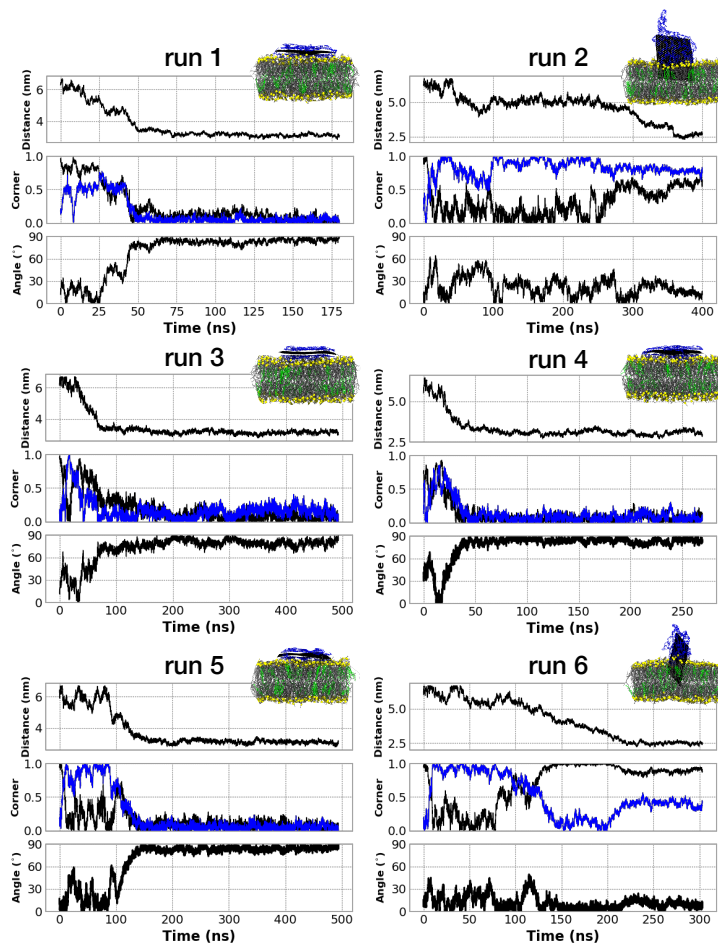
Figure C.5: Analysis of 6 replicates for the 6 ssDNA coated GNF simulations. The analysis and color scheme follows Figure C.3.
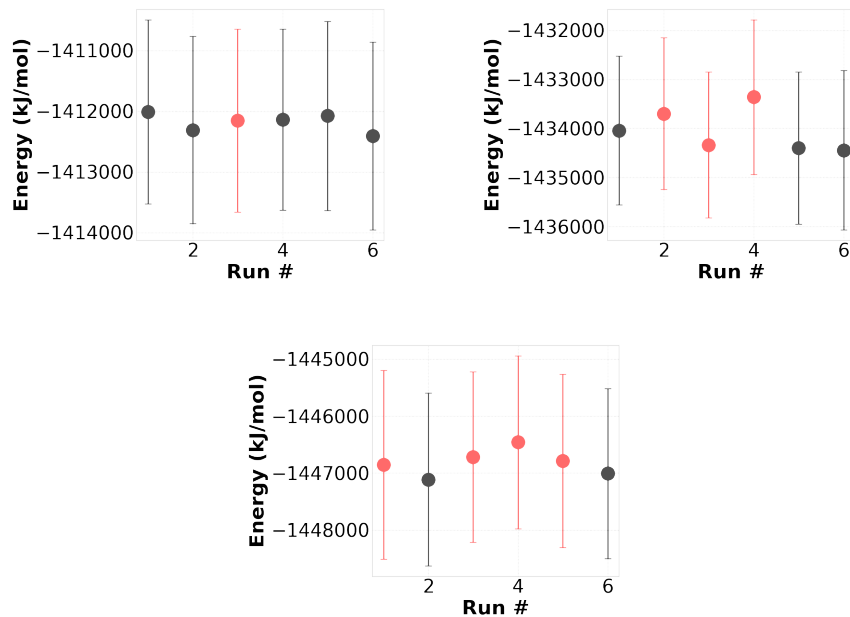
Figure C.6: Potential energies of final configurations of un-steered simulations, averaged over the last 100ps for simulations of 2 chains (top, left), 4 chains (top, right), and 6 chains (bottom). Black: inserted configurations, red: flat configurations. The energetic similarities between flat and inserted configurations suggests flat configurations may be metastable compared to inserted configurations. It should be noted that these are energies of the entire chemical system, thus any local configurational change to the graphene and ssDNA may be muted out by other energetic fluctuations throughout the system.
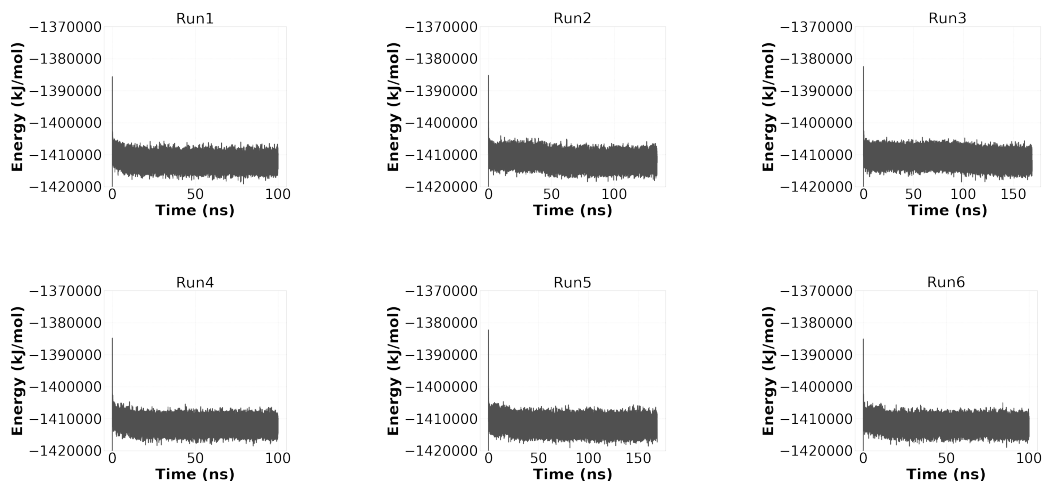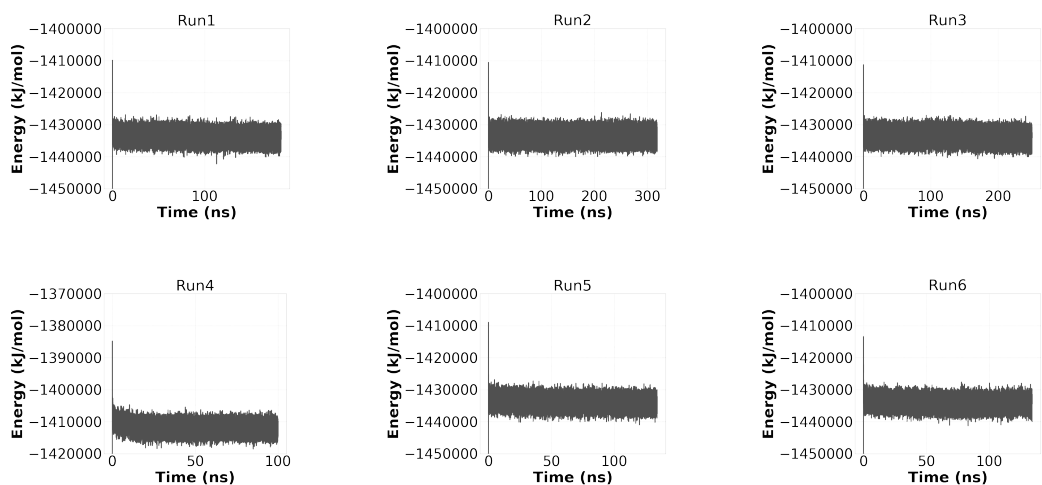
Figure C.7: Potential energies plotted over the course of the non-steered simulations for graphene systems with 2 ssDNA chains. "Run3" represents a simulation with a flat configuration, as opposed to an inserted configuration. It should be noted that these are energies of the entire chemical system, thus any local configurational change to the graphene and ssDNA may be muted out by other energetic fluctuations throughout the system.

Figure C.8: Potential energies plotted over the course of the non-steered simulations for graphene systems with 4 ssDNA chains. "Run2", "Run3", and "Run4" represent simulations with a flat configuration, as opposed to an inserted configuration. It should be noted that these are energies of the entire chemical system, thus any local configurational change to the graphene and ssDNA may be muted out by other energetic fluctuations throughout the system.
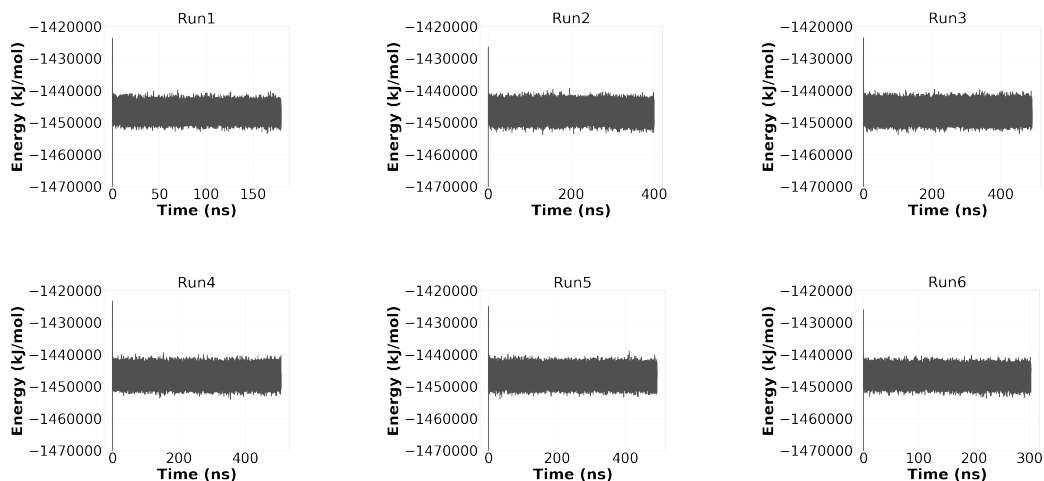
Figure C.9: Potential energies plotted over the course of the non-steered simulations for graphene systems with 6 ssDNA chains. "Run1", "Run3", "Run4", and "Run5" represent simulations with a flat configuration, as opposed to an inserted configuration. It should be noted that these are energies of the entire chemical system, thus any local configurational change to the graphene and ssDNA may be muted out by other energetic fluctuations throughout the system.
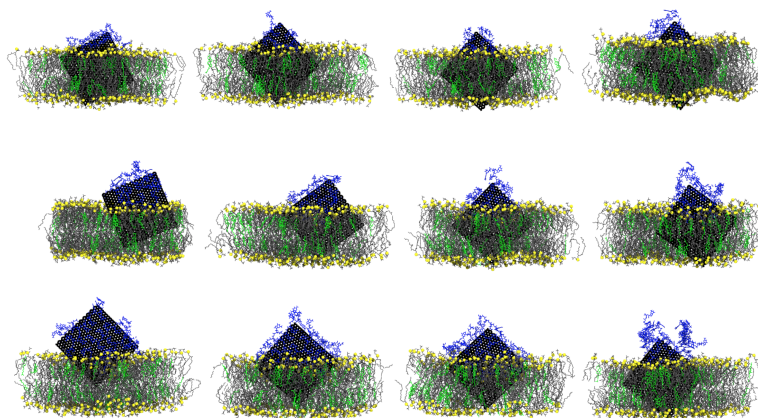

Figure C.10: Final configurations of steered simulations. From left to right: various spring constants of 50, 125, 250, and 500 kJ mol^{-1} nm^{-2}. From top to bottom: coatings of 2, 4, and 6 ssDNA.
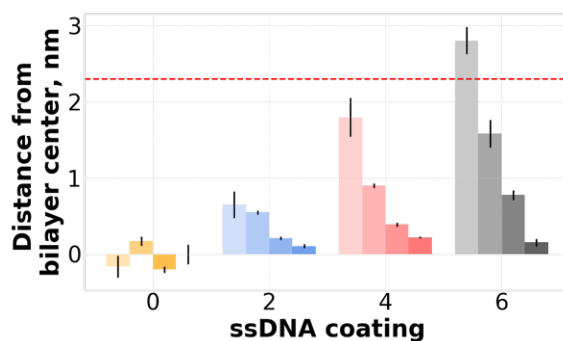
Figure C.11: Distance between centers-of-mass of the GNF and bilayer at the end of the steered simulations of 4 different ssDNA coatings. Four different spring constants, 50, 125, 250, and 500 kJ mol^{-1} nm^{-2} are presented respectively (darker shades are stiffer constants). Bilayer half-thickness is shown as a red dashed line for reference. Color code: 0 ssDNA, i.e., bare GNF (orange), 2 ssDNA (blue), 4 ssDNA (red), 6 ssDNA (black).